Title

Thin film compression toward the single-cycle regime for the advancement of high field science

Author

Farinella, Deano Michael-Angelo

Publication Date

2018

UNIVERSITY OF CALIFORNIA,
IRVINE

Thin film compression toward the single-cycle regime for the advancement of high field science

DISSERTATION

submitted in partial satisfaction of the requirements
for the degree of

DOCTOR OF PHILOSOPHY

in Physics

by

Deano Michael-Angelo Farinella

Dissertation Committee:
Professor Franklin Dollar, Chair
Professor Toshiki Tajima
Professor Roger McWilliams

2018

DEDICATION

To my family

TABLE OF CONTENTS

LIST OF FIGURES

Page

LIST OF TABLES

ACKNOWLEDGMENTS

This journey would not have been possible without a lot of help from a great number of people. These next couple pages are for them.

First I would like to thank my primary adviser Professor Toshiki Tajima for introducing me to the world of laser-plasma physics. I find his physical intuition, theoretical insight and drive to bring the benefits of coherent laser-plasma interactions to bear on society very inspirational and I feel extremely proud to have worked with him. I would also like to graciously thank Professor Franklin Dollar for allowing a student working on PIC simulations the opportunity to carry out ultrafast optics experiments in his lab at UCI. Without his expertise, careful advising and selfless time sacrifices there would have been no chance for me to succeed in carrying out ultrafast laser experiments across the world in less than a year. Additionally I would like to thank Professor Roger McWilliams for our many stimulating physics discussions and for sharing his multi-faceted wisdom from matters of research to matters of life and career. Although the research is not included in this document I would additionally like to thank Professor Laura Tucker, who gave me the opportunity to participate in an education research project in her group. The opportunity to work with Prof. Tucker alongside my physics research opened many doors for me in terms of advancing my own pedagogical training and providing me with teaching opportunities to garner my passion for teaching. In addition to my primary mentors, I would like to recognize Profs. Lin, Heidbrink, and Chanan for their extremely high caliber teaching which lent itself to my development as a researcher.

Much of the experimental research carried out in this dissertation would not have been possible without access to external facilities (ie. the Center for Ultrafast Optical Science (CUOS) and the LASERIX facility at the université Paris-Sud) made possible through strong collaboration with Professor Gerard Mourou, Professor Karl Krushelnick, Jonathan Wheeler, Anatoly Maksimchuk, and John Nees. I am extremely grateful for the opportunity to participate on projects at these facilities.

In addition to my mentors local and abroad, I would like the thank the graduate students that have supported me and helped me navigate the various challenges in graduate school: Calvin, Sam, Yoonwoo, Po-Chun, Scott, Luke, Matt, Nick, Tam, Hunter, Sean, Chris, Ketron, and Adi. You all have taught me valuable lessons in life and graduate school and served as a home away from home for me.

Next I want to thank my foundational mentors from the University of Minnesota. To Kurt Wick, Prof. Robert Gehrz, Prof. Jeremiah Mans, and Prof. Priscilla Cushman, thank you for offering me the opportunity to work on research with you, and for encouraging me to pursue a career in physics through graduate study. Your support was critical and gave me the necessary experience to be competitive in graduate school.

There were many K-12 teachers who had a significant impact on me as well. I want to thank Mr. Lindfors for making high school physics fun and empowering his students to tackle the toughest concepts, you believed in me before I believed in myself. Mr. Brandt, you also made school fun and inspired me to do well in everything I do. Thank you to Mr. Koch and Ms. Schneck who worked with me through middle-school and whose encouragement was essential. Finally thank you to Ms. Hendrix and Ms. Smith, who served as a couple of my foundational mentors upon which all other academic success was built.

Last but not least, I must thank my family. I have been very fortunate to have many members of the Farinella and Haag families who have been very supportive and inquisitive about my studies and have inspired me to be the best version of myself. To my parents, your support and encouragement throughout my academic journey has been the wind at my back. My sense of work-ethic, pride/humility, and conscience stem from your example. You were my first and most important role models and I hope to emulate your likeness in everything I do. To my sister, thank you for your unconditional support and encouragement, it has meant a lot to me throughout my academic career and life. Finally to my partner Kelsey, as a fellow PhD student, we have been through a lot in the past five years. You have supported me unconditionally through thick and thin. Whether it be helping prepare meals, perform various “cat duties,” household chores, or helping me plan things out when I was unable, in many cases you were a big part of why I was able to accomplish my research goals. I look forward to the opportunity to provide you with the same support you have given me in your endeavors, and look forward to our life together.

This research work has been funded in part by the following sources: the Norman Rostoker Fund, the Alfred P. Sloan Foundation, the National Science Foundation Science and Technology Center for Real-Time Functional Imaging (NSF-STROBE), and the Extreme Light Infrastructure - Nuclear Physics (ELI-NP)

Permission has been granted to include previously published work in this manuscript from the American Physical Society and The American Institute of Physics. This permission is granted to the author on the Journal copyright FAQ pages for re-use in theses and dissertations for each journal respectively.

CURRICULUM VITAE

Deano Michael-Angelo Farinella

EDUCATION

Doctor of Philosophy in Physics	**2018**
University of California, Irvine	*Irvine, California*
Master of Science in Physics	**2015**
University of California, Irvine	*Irvine, California*
Bachelor of Science in Astrophysics	**2013**
University of Minnesota, Twin Cities	*Minneapolis, Minnesota*
Bachelor of Science in Physics	**2013**
University of Minnesota, Twin Cities	*Minneapolis, Minnesota*

RESEARCH EXPERIENCE

Graduate Student Researcher	**2015–2018**
University of California, Irvine	*Irvine, California*
Undergraduate Student Researcher	**2009–2012**
University of Minnesota, Twin Cities	*Minneapolis, Minnesota*

TEACHING EXPERIENCE

Graduate Teaching Assistant	**2013–2015**
University of California, Irvine	*Irvine, California*
Undergraduate Teaching Assistant	**2012-2013**
University of Minnesota, Twin Cities	*Minneapolis, Minnesota*

PEER-REVIEWED PUBLICATIONS

Wakefield in solid state plasma with the ionic lattice force **Feb 2018**

S. Hakimi, T. Nguyen, **D.M. Farinella**, C.K. Lau, H.-Y. Wang, P. Taborek, F. Dollar, T. Tajima

Phys. Plasmas **25**, 023112 (2018)

Particle-in-cell simulation of x-ray wakefield acceleration and betatron radiation in nanotubes **Oct 2016**

X.M. Zhang, T. Tajima, **D.M. Farinella**, Y.M. Shin, G. Mourou, J. Wheeler, P. Taborek, P. Chen, F. Dollar, and B. Shen

Phys. Rev. Accel. Beams **19**, 101004 (2016)

High energy photon emission from wakefields **Jul 2016**

D.M. Farinella, C.K. Lau, X.M. Zhang, J.K. Koga, S. Taimourzadeh, Y. Hwang, K. Abazajian, N. Canac, T Ebisuzaki, P. Taborek, and T. Tajima

Phys. Plasmas **23**, 073197 (2016)

MANUSCRIPTS IN PREPARATION

Pulse compression and focusability of high intensity laser pulses after self-phase modulation in thin films **2018**

D.M. Farinella, J. Wheeler, A. Hussein, J. Nees, M. Stanfield, N. Beier, G. Cojocaru, R. Ungureanu, M. Pittman, J. Demailly, E. Baynard, D. Ros, R. Fabbri, R. Secareanu, M. Masruri, A. Naziru, R. Dabu, A. Maksimchuk, K. Krushelnick, G. Mourou, T. Tajima, F. Dollar

CONFERENCE PRESENTATIONS

Far-field effects of high intensity self-phase modulation in fused silica wafers **Sept 2018**

D.M. Farinella, J. Wheeler, A. Hussein, J. Nees, M. Stanfield, N. Beier, G. Cojocaru, R. Ungureanu, M. Pittman, J. Demailly, E. Baynard, D. Ros, R. Fabbri, R. Secareanu, M. Masruri, A. Naziru, R. Dabu, A. Maksimchuk, K. Krushelnick, G. Mourou, T. Tajima, F. Dollar

International Committee on Ultrahigh Intensity Lasers, Lindau, Germany, 2018 (Upcoming)

Thin film compression of a high rep rate laser: towards single-cycle pulse generation **Oct 2017**

D.M. Farinella, X.M. Zhang, C.K. Lau, S. Taimourzadeh, Y. Hwang, J. Koga, T. Ebisuzaki, T. Tajima

American Physical Society - Division of Plasma Physics, Milwaukee, WI, 2017

Laser wakefield signatures: from gas plasma to nanomaterials **Oct 2016**

D.M. Farinella, X.M. Zhang, Y. Shin, T. Tajima

American Physical Society - Division of Plasma Physics, San Jose, CA, 2016

High energy photon emission from wakefields and its signatures in astrophysical blazars **Nov 2015**

D.M. Farinella, X.M. Zhang, C.K. Lau, S. Taimourzadeh, Y. Hwang, J. Koga, T. Ebisuzaki, T. Tajima

American Physical Society - Division of Plasma Physics, Savannah, GA, 2015

ABSTRACT OF THE DISSERTATION

Thin film compression toward the single-cycle regime for the advancement of high field science

By

Deano Michael-Angelo Farinella

Doctor of Philosophy in Physics

University of California, Irvine, 2018

Professor Franklin Dollar, Chair

Recent developments in ultrashort ($\sim$ 30-50 fs) laser technology such as chirped pulse amplification (CPA) have made relativistic laser-plasma interactions accessible to research institutions and universities across the globe and paved the way for research institutions to increase laser pulse power beyond 1 petawatt. The high achievable intensities and ultrashort pulse durations now available have reinvigorated the fields of nonlinear optics and photonics as well as high intensity laser-plasma physics. Theoretical models which could previously only be explored computationally such as laser wakefield acceleration are now routinely realized experimentally and are being perfected at labs across the globe.

Though much progress has been made, there is a nearly accessible regime that could open the door to a new class of laser-plasma interactions providing novel schemes for heavy particle acceleration and secondary coherent source generation, the *single-cycle regime*. High efficiency pulse compression schemes such as thin film compression (TFC) have made possible the increase in optical power through a decrease in pulse duration. This technique not only serves as a powerful shortcut to higher laser peak power, but also reduces the laser pulse duration-consequently increasing the degree of coherence of the interactions of compressed laser pulses with plasmas.

The first half of this thesis is dedicated to demonstrating this pulse compression at intensities comparable to petawatt facilities ($\sim$ 1 TW/cm^2). Pulse compression experiments were carried out in the Dollar Lab at UCI, the LASERIX facility at the Université Paris-Sud and the HERCULES laser at the University of Michigan. Pulse compression of a factor of $\sim$ 2 has been demonstrated on multiple laser systems using fused silica as the nonlinear medium, with slightly better compression using plastics. Furthermore, laser mode quality is seen to be largely maintained in the process of nonlinear spectral broadening (which is required for pulse compression) in the highest power systems. Finally, a set of preliminary studies at near-infrared wavelengths (1140 - 1500 nm) investigate the high intensity spectral broadening in various dispersion regimes motivated by the potential for self-compression.

In the second half of this thesis particle-in-cell simulations are carried out that utilize x-ray laser pulses which could be generated by a combination of TFC and laser-plasma interactions in the single-cycle regime to drive laser wakefields in nanotubes. The laser wakefields generated in these nanotubes are shown to drive unprecedented acceleration gradients of up to TeV/cm and also an increased laser pulse propagation and therefore laser wakefield lifetime. At the other density extreme, another particle-in-cell study was performed investigating the possibility of laser wakefields as a contributing acceleration mechanism for ultra-high energy cosmic rays from blazar jets. In each case, the particle acceleration and photon emission properties of the wakefield are analyzed and scaling laws are developed for various parameters of interest, and are compared and contrasted to typical laboratory cases.

Chapter 1

Introduction

The first laser was made in 1960 [8] shortly after its invention in 1958 [9] as an optical extension of the Microwave Amplification by Stimulated Emission of Radiation (MASER) technique. In the case of optical frequencies this is called "Light Amplification by Stimulated Emission of Radiation" (LASER). Acronyms like these are used today as nouns to refer to the object performing the amplification of light.

Today there are a myriad of laser systems that use vastly different materials to act as the lasing medium, but the mechanism of amplification is the same. Electrons in a medium (gas, solid, dye) which we will call the active medium, are first brought into an excited state by a process called pumping. As electrons in the medium leave the excited state, the decay produces photons which carry away some of the energy from the excited electrons. This is called spontaneous emission, and is emitted with no preferential direction.

Typically the medium is pumped to a short-lived state that very quickly decays to a long-lived state. This long-lived state has a transition energy of the photons to be amplified. By containing the active medium in an optical cavity, photons with energy of the long-lived electronic excitation of the active medium can also excite electrons in the active medium. A condition called a population inversion is achieved when more of the electrons in the active medium are in an excited state than not. In this case, photons entering the active medium are more likely to encounter excited electrons than not. When impinging upon these excited electrons, they can induce the electrons to transition to a lower energy state and therefore produce “cloned” photons which have the same polarization, phase, and direction as the impinging photons-this is the process called stimulated emission. These newly generated photons are also more likely to encounter an electron in an excited state than not, and therefore are likely to produce further simulated emission [10]. As you can see, the number of photons produced from stimulated emission can grow large very quickly thereby amplifying the light. The early demonstration of this light amplification resulting in coherent radiation began the process of producing ever more intense light sources that continues to this day.

1.1 Pulsed laser technology

Since the first demonstration of the laser [8], laser peak power has been dramatically increased by inventing techniques which result in successively decreasing laser pulse duration. In 1962, modulation of the laser-cavity quality factor allowed the same energy to be released in a nanosecond time scale, to produce pulses in the megawatt range [11], a thousand times shorter than the earlier laser durations. In 1964, locking the longitudinal modes of the laser (mode-locking) allowed the laser pulse duration to be reduced by another factor of a thousand, down to the picosecond regime, pushing the peak power to the GW regime [12, 13].

1.1.1 Chirped pulse amplification

At this point, the intensities associated with the ultrashort (ps) pulses were approaching the levels at which the index of refraction becomes non-negligibly modified by the pulse intensity ($\sim$ GW/cm^2) in a process known as the optical Kerr effect ($n = n_0 + n_2 I$), which will be explored in detail in Chap. 2 [14]. This nonlinear effect can lead to wave-front errors [15] and small-scale self-focusing leading to beam filamentation [16] and ultimately damage to optical components [17]. Further, laser amplifier materials with relatively low saturation fluence ($F_{sat} \sim 10^{-3}$J/cm^2) were used since for most efficient energy extraction the laser fluence and saturation fluence should be matched [17]. Since the intensity could not be increased, the only way to increase peak power seemed to be to increase the laser system aperture, making these systems larger and more expensive [17].

This was the case until the invention of Chirped Pulse Amplification (CPA) in 1985 [18]. As shown in Fig. 1.1 a short pulse is first produced by an oscillator. The short pulse is then stretched from femtoseconds to picoseconds or nanoseconds duration, which in turn drastically reduces its intensity and enables the use of high energy storage solid state amplification media with much higher saturation fluence ($F_{sat} \sim 1$ J/cm^2). Once the intensity has been reduced, the stored energy in the amplifying medium can be extracted without accruing damage induced by high intensity effects. Once the energy has been efficiently extracted from the amplifier, the pulse is then re-compressed to near its initial pulse duration, therefore drastically increasing the compressed peak power. The key challenges overcome by CPA are enabling the use of the highest input fluence for efficient energy extraction from high energy storage amplifiers, while maintaining low enough intensity such that undesirable nonlinear effects in the beam and damage are avoided.

As shown in Fig. 1.2, in recent years CPA has enabled laser peak powers to reach the petawatt level [19, 20]. However even with these advancements, next generation laser

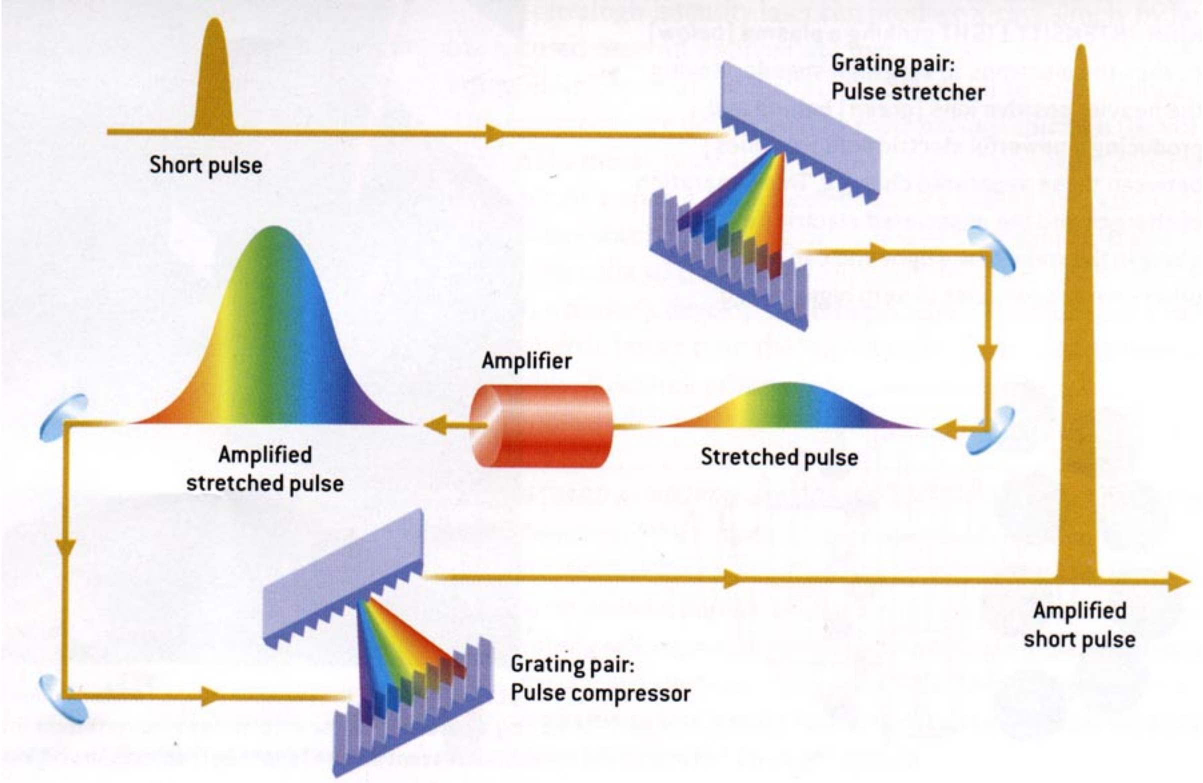

Figure 1.1: Shown above is the basic Chirped Pulse Amplification (CPA) scheme. An ultrashort high intensity laser pulse is stretched to a longer duration allowing it to be amplified without inducing nonlinearity or causing damage to the amplification medium. Once the energy is efficiently extracted from the amplification medium, it is re-compressed with a matched compressor to reach a dramatically increased peak power. Image credit: https://cuos.engin.umich.edu/researchgroups/hfs/facilities/ chirped-pulse-amplification/

driven accelerators and high field science [21, 22, 23, 24] require laser technology with even shorter pulse durations and higher peak power than is currently available.

To meet these challenges, facilities across the world are working to increase the peak power of their laser systems by developing higher energy lasers in order to reach 10 PW at the Extreme Light Infrastructure (ELI) [25] or even 100 PW at the Station of Extreme Light (SEL) [26] in Shanghai. On the other hand, the pulse length-intensity conjecture [27] suggests that the compression of laser pulses to an ultimate limit perhaps provides an alternative path to high intensities.

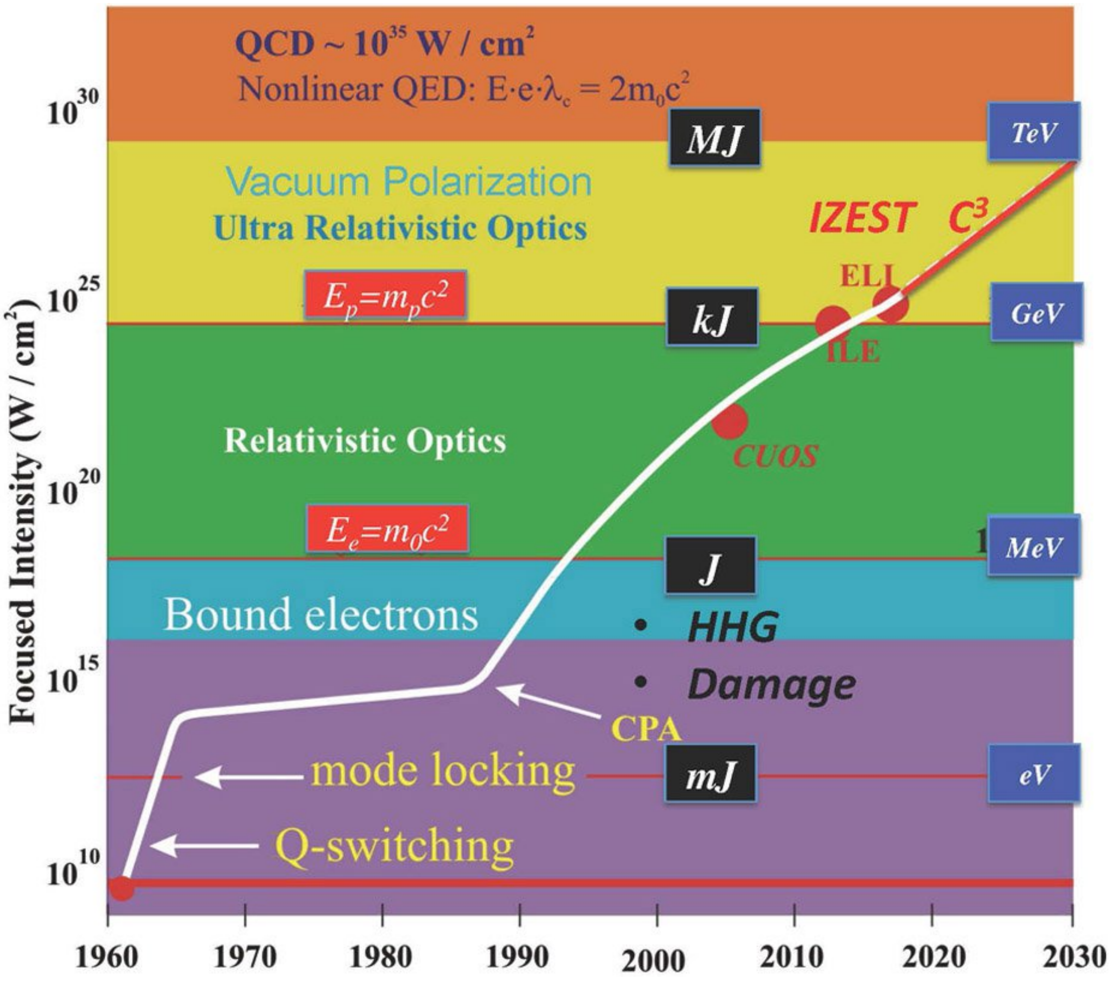

Figure 1.2: The evolution of focused peak intensity as a function of time. Image credit: [1]

1.2 Compression of ultrashort laser pulses

Many short-pulse petawatt laser facilities have laser pulse durations in the 25-50 fs range [28, 29, 30]. As mentioned in the previous section, facilities across the world are beginning to build facilities that will push beyond 1 PW to 10 PW or even 100 PW. To do this, these larger and more expensive facilities are planning to increase the energy of their laser pulses. However, as has been the theme of much of the history of of developing ever more intense laser pulses, decreasing the pulse duration of existing systems, may be key to a dramatic shortcut to higher peak power.

Ironically, if harnessed effectively the very same nonlinearities responsible for damaging amplifiers and limiting laser pulse intensity before CPA, can be used to generate a larger spectral bandwidth amenable to pulse compression. Further, with proper phase compensation the process can lead to power amplification via pulse compression. The relevant nonlinearity for optical pulse compression is called self-phase modulation (SPM) and was first observed in the late 1960s [31, 32, 33, 34]. SPM is a nonlinear effect that arises due to a change in the index of refraction through what is known as the Kerr effect ($n(t) = n_0 + n_2 I(t)$) and will be discussed in detail in Chap. 2. Specifically, the index of refraction is modified locally within the pulse and is proportional to the local intensity temporal profile. In this way, the center of the pulse experiences a larger index of refraction than the tails during propagation. This self-modulation of phase leads to a retardation of the center of the laser pulse with respect to the tails of the pulse leading to a red-shift at the leading edge of the pulse and a blue-shift at the trailing edge [35]. This phase modulation (which does not change the duration of the pulse itself) necessarily increases the bandwidth of the laser pulse. This increase in spectral bandwidth, combined with a phase delay that is nearly quadratic (linearly chirped) within the full width at half-maximum of the laser pulse allows the pulse to be compressed to a shorter duration by compensating the quadratic phase accrued through SPM.

1.2.1 Fiber and bulk compression

Although the temporal effects of SPM turn out to be very beneficial for pulse compression, the Kerr effect can also lead to spatial effects. Consider a Gaussian beam, as in the time domain the Kerr nonlinearity can cause a beam to accrue a larger phase delay at the peak of the intensity profile than the periphery known as a Kerr lens. This can lead to an on-axis whole beam self-focusing [36, 35], which will also be explored in more detail in Chap. 2.

SPM spectral broadening was originally induced by transmission through single-mode fibers, where only a the fundamental mode is guided [37]. This meant that any additional confinement of the mode to the fiber due to self-focusing was negligible [38] The mode was preserved during propagation, and the spectrally broadened pulse could then be compressed to the Fourier limit by compensating the phase incurred [39]. This technique became the primary way at the time to generate few-cycle laser pulses [40]. Early results using this technique showed that 5.4 nJ pulses could be compressed from 5.4 ps to 450 fs [39]. Pushing this method to its limit, laser pulses of up to 20 nJ were compressed from 40 fs to < 8 fs (fewer than 4 cycles) [41]. The fundamental energy limitation imposed by using single-mode fibers for this process involved requirements on its core radius. In order to guide only the fundamental LP_{01} mode in these step-index fibers, the so-called V number has to be < 2.4, where $V = a\omega(n_{core}^2 - n_{clad}^2)^{1/2}/c$ [42]. Here a is the core radius, ω is the frequency of light, c is the speed of light, and n_{core} and n_{clad} are the indices of refraction of the core and cladding respectively. Therefore these fused silica-core single-mode fibers typically had a fiber radius on the order of $\sim O(1 - 10\mu\mathrm{m})$.

Beyond this limit, the high intensities caused material damage and higher order nonlinearities to become prevalent in these single-mode fibers [40]. To push forward to higher energy pulse compression, a technique using fused silica hollow-core capillaries filled with noble gases was investigated. This technique used a larger core radius $\sim O(50 - 100\mu\mathrm{m})$ and a medium with a higher damage threshold than the single-mode fibers for SPM. Wave propagation in these guided structures occurred by grazing incidence reflections at the inner surface of the capillary which strongly discriminated against higher order modes. Therefore given a core radius, by choosing a sufficiently long capillary, only the fundamental mode would propagate [43]. This technique was shown to be able to compress laser pulses on the order of 100 µJ [44]. Soon thereafter it was shown that this technique could produce laser pulses of down to 5 fs (just under 2 optical cycles) [45]. Ultimately, this compression method was was also limited to energies of $\sim O(1\text{ mJ})$ imposed by ionization and energy losses due to mode coupling with the capillary [46, 43].

In an attempt to achieve scalable pulse compression to energies beyond the limits of hollow-core capillaries bulk material was investigated as a means to compress ultra-short pulses [47]. This technique relaxed restrictions on mode size, allowing essentially any energy pulse to be used, as long as the intensity was kept below the ionization threshold for the SPM material. The short length of the material used in this technique proved to minimize the negative effects due to self-focusing, but lost the benefits provided by good mode quality in the single-mode fiber based techniques. The spectral broadening through SPM itself also suffers when using a non-uniform spatial intensity profile. Therefore only the central region of the beam profile, where the intensity-and therefore spectral broadening was nearly constant was compressed. Nevertheless this technique showed a 20% efficient compression of the central portion of the Gaussian mode that could be extended in principle to arbitrary energy.

1.2.2 Thin film compression

To scale pulse compression to petawatt laser systems a technique called “thin film compression” (TFC) has been suggested by Mourou, *et al.* [48]. Like bulk compression, this unguided technique is scalable to arbitrary energy with no requirements on aperture size, but instead proposes using plastic thin films with a high nonlinear index n_2, as the nonlinear medium. By using a flat-top intense laser pulse $\sim$ O(1 TW/cm^2) to induce SPM in a thin film, the spectrum of the laser pulse could be uniformly broadened across the entire beam profile allowing for uniform compressibility. Additionally due to the lack of large-scale spatial gradients, the beam profile would not induce a Kerr lens in the same fashion as a Gaussian beam (flat-top beams with $P > P_{cr}$ tend to be susceptible to other types of collapse dynamics that will be explored in Chaps. 2 and 4, which can be mitigated by minimizing small scale intensity fluctuations in the beam and keeping optical components thin). Furthermore when fused silica wafers are used as the nonlinear medium and the film is oriented at Brewster's angle, the energy throughput can surpass 99% as will be shown in Chap. 4. As before, the linear chirp due to SPM can then be compensated with proper phase compensation (ie. chirped mirrors), constructing a shorter pulse. Using this technique to compress laser pulses at the petawatt level could serve as a shortcut to the high power frontier on the world stage. Additionally, TFC could be used to compress flat-top optical laser pulses towards the relativistic single-cycle limit. Several applications of such relativistic single-cycle pulses will be explored briefly in the following section.

1.3 Applications of compressed ultrashort laser pulses

Relativistic ultrashort laser pulses compressed to the single-cycle regime can induce unique laser-matter interactions due their duration, and electric field structure. The next two sections will very briefly review some promising applications of compressed laser pulses to particle acceleration and secondary source generation.

1.3.1 Single-cycle ion acceleration

Through TFC of petawatt laser pulses, access is granted to a new ion acceleration regime called the single-cycled laser acceleration (SCLA) regime [22, 2]. Pulse compression offers at least two benefits for ion acceleration in this regime.(1) By decreasing the laser pulse length at a fixed energy, the intensity of the laser pulse can be increased [2]. (2) By decreasing the number of oscillations in the laser pulse, the efficiency, coherence, and stability of the ponderomotive acceleration is enhanced. In the case of a single-cycle pulse, upon interaction with a thin foil a more coherent electron acceleration takes place due to the single oscillation of the electric field leading to a collective forward push by $\mathbf{v} \times \boldsymbol{B}$ as there are no longer many cycles to average over. A sharp electron layer is formed which results in a longitudinal electrostatic field that then uniformly accelerates ions in the forward direction leading to acceleration of mono-energetic ultrashort proton bunches to GeV energies.

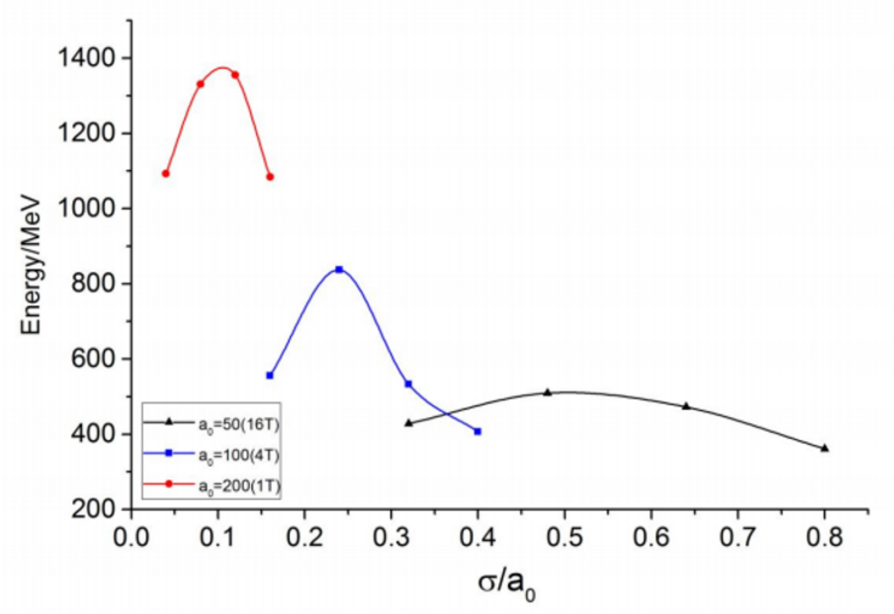

Figure 1.3: Proton cut-off energy - (a) The resulting proton energies by scaling σ/a_0, where the red, blue, and black lines represent $a_0 = 50$, 100 and 200 and corresponding pulse durations $\tau = 16T$, $4T$, and $1T$ respectively. Image credit: [2]

2D particle-in-cell simulations from Ref. [49] investigated the effect of scaling the laser pulse duration at a fixed energy to determine the resultant ion acceleration through interaction with a thin foil. Laser pulses with a Gaussian temporal profile with $\lambda = 1$μm, were focused to a 5λ focal spot on a 50 nm CH foil with a carbon to hydrogen ratio of 9:1 and a normalized electron density of $n_e = 480n_c$ where $n_c = m_e\epsilon_0\omega_L^2/e^2$. Laser pulses with $a_0 = 50$, 100, and 200 were explored with a corresponding pulse duration of $16T$, $4T$, and $1T$ representing compression at a fixed energy. Where $a_0 = eE/m_e\omega_L c$ is the normalized vector potential and T is the length of a single optical cycle. For each pulse length condition, the normalized electron areal density $\sigma = n_e l/n_c\lambda$ is scanned to retrieve the largest proton cut-off energy where l is the target thickness. Fig. 1.3 (a) shows that as the pulse duration is decreased at a fixed energy, the proton cutoff energy progressively increases. Furthermore it is seen that in the single-cycle limit, the optimal areal density becomes more precisely defined at $\sim \sigma = 0.1a_0$. This thin optimal target thickness allows for the more direct utilization of the photon energy instead of cascading through multiple collisional processes as in other methods such as target normal sheath acceleration (TNSA) [20, 50, 51]. To learn more about the subtle and interesting regime presented in this chapter, the reader is encouraged to explore Refs. [52, 53, 54], and a comprehensive review of the laser-driven ion acceleration literature can be found in Refs. [55, 56, 57]

1.3.2 X-ray generation

Another potential application of TFC compressed laser pulses was originally explored by Ref. [3] and demonstrated through particle-in-cell simulations. The generation of laser pulses on the attosecond timescale was achieved through an interaction of a few-cycle optical laser pulse with an overdense plasma. Due to the coherent nature of this technique, its efficiency was shown to be very high ($\sim 10\%$) when compared to other attosecond pulse generation schemes [58, 59, 60]. Due to its high efficiency and scalability, It has since been suggested as the second stage of a compression scheme to generate laser pulses beyond the optical single-cycle limit to reach the single-cycle x-ray regime [24]. In this case it is critical to have well-corrected tightly focused fundamental frequency beam to enhance the coherence of the reflected light.

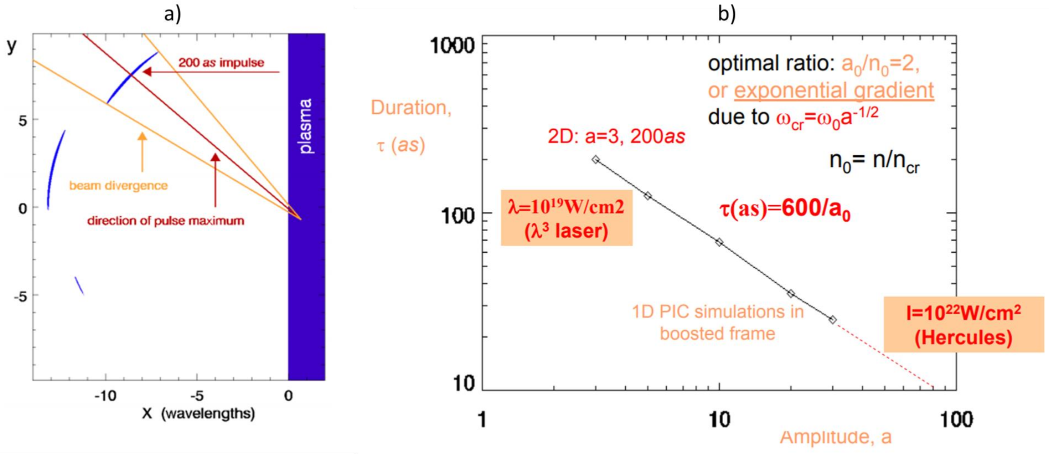

Figure 1.4: (a) The reflected pulses of a 5 fs optical laser pulse with $a_0 = 3$ after interacting with a slightly over-critical density ($n_e = 1.5n_c$) plasma. Maintaining this ratio of a_0/n_c, and scaling the laser vector potential yields shorter pulses with the scaling relationship $\tau = 600/a_0$ as seen in (b). Image credit:[3, 4]

2D particle-in-cell simulations carried out in Ref. [3] studied the interaction of a $\lambda = 0.8$µm laser with a Gaussian temporal shape with an over critical plasma ($n_e = 1.5n_c$). Laser pulses with a full-width at half maximum pulse duration of $\tau = 5$ fs (∼ 2 optical cycles) were focused to a 1λ spot size and an intensity of 2×10^{19} W/cm^2 ($a_0 = 3$). The plasma electrons were displaced into the plasma creating a strong electrostatic potential and therefore rebounded toward their parent ions Doppler up-shifting the reflected pulse. As seen in Fig 1.4 (a) an isolated 200 attosecond pulse with 10% of the initial energy resulted from the interaction. Further simulations were carried out that showed continued decreases in pulse duration as a_0 was increased as shown in Fig. 1.4 (b). Combining TFC with this relativistic compression at higher a_0 holds promise to generate the laser pulses necessary to drive laser wakefields at solid densities as will be further explored in Chap. 6.

1.4 Structure of thesis

The overall structure of this thesis is as follows. Chapter 2 reviews the relevant theoretical background for the ultrafast pulse compression experiments. It describes in detail the linear and nonlinear response of isotropic matter to ultrashort laser pulses and how they are used in pulse compression. Chapter 3 reviews the various capabilities and diagnostics developed by the author to carry out the experimental studies. Chapter 4 details the various pulse compression experiments carried out at various facilities. In addition to temporal compression, the effect of SPM on the laser far-field with flat-top and Gaussian mode types is investigated. Chapter 5 investigates SPM at longer wavelengths in the near infrared in two different experiments where the nonlinear coefficients are less well-known. Finally, since a potential application of thin film compression is the generation of short pulse coherent x-rays, as discussed in the previous section, particle-in-cell simulations were carried out investigating the utility of these types of x-ray pulses in driving wakefields at solid densities in Chap. 6. The wakefield strength, electron acceleration, and photon emission properties are contrasted between in cases with optical and x-ray laser drivers. On the other hand, laser wakefields were also computationally investigated as a potential source of high energy cosmic rays from blazars. Simulations were carried out using a base case to tie the results to present day experimental findings and scale the parameters in the direction of the conditions present in the astrophysical environment. Chapter 8 is dedicated to a pulse measurement technique developed by the author that sprung from insights gained from experiments carried out in Chap. 4 and 5. Finally, Chap. 9 reviews the findings of this body of work and suggests a few promising future directions for approaching the relativistic single-cycle limit.

Chapter 2

Laser pulses in matter

2.1 Linear response

Our further discussions will hinge critically on the interaction of light with dielectrics, therefore we will start with understanding how these non-conductive materials respond to electric fields. We will start by modifying Maxwell's equations with the induced bound source terms in a dielectric. We will then derive a simplified model for the index of refraction in dielectrics to guide our physical intuition. Finally, we will discuss the practical implications of the model and connect the theory to our best physical approximations for dispersion. Maxwell's equations in SI units in the absence of free charge and current are

$$\nabla \cdot \mathbf{E} = 0 \tag{2.1a}$$

$$\nabla \times \mathbf{E} = -\frac{\partial \mathbf{B}}{\partial t} \tag{2.1b}$$

$$\nabla \cdot \mathbf{B} = 0 \tag{2.1c}$$

$$\nabla \times \mathbf{B} = \mu_0 \epsilon_0 \frac{\partial \mathbf{E}}{\partial t} \tag{2.1d}$$

However in a non-uniform dielectric, bound charge density can change locally (ΔQ_{pol}) in a volume when exposed to an external field. The induced polarization through the surface of the volume is due to the enclosed change in electric charge.

$$\Delta Q_{\text{pol}} = -\oint_S \mathbf{P} \cdot \hat{n}\, da \tag{2.2}$$

Where we also know by definition, where ρ_{pol} is the bound charge density,

$$\Delta Q_{\text{pol}} = \int \rho_{\text{pol}}\, dv \tag{2.3}$$

and finally from divergence theorem.

$$\int \nabla \cdot \mathbf{P}\, dv = \oint_S \mathbf{P} \cdot \hat{n}\, da \tag{2.4}$$

Therefore we can see that

$$\int \rho_{\text{pol}}\, dv = -\int \nabla \cdot \mathbf{P}\, dv \tag{2.5a}$$

$$\implies \rho_{\text{pol}} = -\nabla \cdot \mathbf{P} \tag{2.5b}$$

If the external electric field is time-varying, this leads to the motion of bound charges, giving rise to a time-varying bound current density $\boldsymbol{j}_{\mathrm{pol}} = Ne\mathbf{v}$. If we recall that $\mathbf{P} \equiv Ne\boldsymbol{x}$, we can see that $\boldsymbol{j}_{\mathrm{pol}} = d/dt(Ne\boldsymbol{x}) = d\mathbf{P}/dt$. Unlike the bound charge density, bound currents can exist in perfectly isotropic materials, granted that there is a time-varying field. The modified Maxwell's equations in a dielectric in the absence of free charge and current are the following.

$$\nabla \cdot \mathbf{E} = \frac{\rho_{\mathrm{pol}}}{\epsilon_0} = \frac{-\nabla \cdot \mathbf{P}}{\epsilon_0} \tag{2.6a}$$

$$\nabla \times \mathbf{E} = -\frac{\partial \mathbf{B}}{\partial t} \tag{2.6b}$$

$$\nabla \cdot \mathbf{B} = 0 \tag{2.6c}$$

$$\nabla \times \mathbf{B} = \mu_0 \boldsymbol{j}_{\mathrm{pol}} + \mu_0 \epsilon_0 \frac{\partial \mathbf{E}}{\partial t} = \mu_0 \frac{\partial}{\partial t}(\mathbf{P} + \epsilon_0 \mathbf{E}) \tag{2.6d}$$

It is worth emphasizing here that in an isotropic medium (ie. fused silica) the the time varying polarization enters Maxwell's equation through driven bound currents in the media as shown above. In the case of weak, slowly varying fields the polarization **P** varies approximately linearly with the electric field **E** [61]. In this context it is often convenient to define the electric displacement field (**D**) since it contains the electric fields due to the material (**P**) as well as external fields (**E**) as seen in Eq. 2.7. [61].

$$\mathbf{D} = \epsilon_0 \mathbf{E} + \mathbf{P} = \epsilon_0 \mathbf{E} + \epsilon_0 \chi(\omega)^{(\mathbf{1})} \mathbf{E} = \left(1 + \chi(\omega)^{(\mathbf{1})}\right) \epsilon_0 \mathbf{E} = n^2(\omega) \epsilon_0 \mathbf{E} \tag{2.7}$$

Here $n(\omega)$ is the index of refraction, and $\chi(\omega)^{(1)}$ is the linear susceptibility of the material. In general the linear susceptibility is a second rank tensor and determines the polarization in a medium in response to any general electric field. For the purposes of this chapter, we will assume the electric field is linearly polarized, and that the medium is isotropic in which case the susceptibility tensor may be treated as a constant. A surprising number of physical phenomena can be described by modeling the polarization with a linear response.

By using this notation for the susceptibility with the superscript (1), we are committing to this approximation for now. The constant of proportionality of displacement field to the total electric field (Eq. 2.8) is called the permittivity of the material. It is important to emphasize here that this *constant of proportionality* is an approximation, and is only true if the field **E** does not become too large.

$$\epsilon(\omega) = \Big(1 + \chi(\omega)^{(1)}\Big)\epsilon_0 = n^2(\omega)\epsilon_0 \tag{2.8}$$

Sometimes it is also useful to refer to the dimensionless quantity $\epsilon_r(\omega)$, typically referred to as the dielectric constant or relative permittivity.

$$\epsilon_r(\omega) = \frac{\epsilon(\omega)}{\epsilon_0} = 1 + \chi(\omega)^{(1)} = n^2(\omega) \tag{2.9}$$

As will become clear in Sec. 2.2, $\chi(\omega)^{(1)}$ represents an approximation of the material response to an electric field.

2.1.1 The electric susceptibility $\chi^{(1)}$

Now that we have reviewed Maxwell's equations in a dielectric, and claimed that under certain conditions a decent approximation for the polarization is $\mathbf{P} = \epsilon_0\chi(\omega)^{(1)}\mathbf{E}$, the question that remains is what on earth is $\chi(\omega)^{(1)}$? To get a better physical sense of this, we will explore the Lorentz model [62] for $\chi(\omega)^{(1)}$ of which serves to guide our physical intuition. In the presence of an external oscillating electric field, electrons bound by electrostatic forces to their parent ions, and subject to velocity dependent damping was modeled by Lorentz using the damped driven harmonic oscillator.

$$\mathbf{F} = q\mathbf{E} = m(\omega_0^2 + \gamma\frac{d}{dt} + \frac{d^2}{dt^2})\boldsymbol{x} \tag{2.10}$$

Here ω_0 is the natural frequency of the oscillator and γ represents the velocity dependent damping. The Fourier transform can be employed to solve the differential equation for the displacement of these oscillators.

$$\mathbf{E}(\omega) = -\frac{m_e}{e}(\omega_0^2 - i\gamma\omega - \omega^2)\boldsymbol{x}(\omega) \tag{2.11}$$

This leads to an expression for the displacement of the electrons.

$$\boldsymbol{x}(\omega) = -\frac{e}{m_e}\frac{\mathbf{E}(\omega)}{(\omega_0^2 - \omega^2) - i\gamma\omega} \tag{2.12}$$

Recalling that $\mathbf{P} = -Ne\boldsymbol{x}$, and that the first order polarization can be expressed as

$$\mathbf{P} = \epsilon_0\chi(\omega)^{(1)}\mathbf{E}, \tag{2.13}$$

it is readily identified by algebra that the first order dielectric susceptibility takes the form shown below in Eq. 2.14

$$\chi^{(1)}(\omega) = \frac{Ne^2}{\epsilon_0 m_e}\frac{1}{(\omega_0^2 - \omega^2) - i\gamma\omega} = \frac{\omega_p^2}{(\omega_0^2 - \omega^2) - i\gamma\omega} \tag{2.14}$$

or equivalently

$$n^2(\omega) - 1 = \frac{\omega_p^2}{(\omega_0^2 - \omega^2) - i\gamma\omega} \tag{2.15}$$

where we have made use of the substitution $\omega_p^2 = Ne^2/\epsilon_0 m_e$, where ω_p is the plasma frequency. This equation represents the response of a system of oscillators with a single resonance subject to damping. It is noted here that for a complete theory of the response inside a dielectric one needs to take into account the local field correction to the electric field which can be found in Ref. [63]. Real materials have many resonances and make this function difficult to determine analytically. If we agree to stay away from resonances which are in the ultraviolet for most glasses including fused silica, the damping term can be neglected and an approximation for the response can be made taking into account the effect of a sum of resonances. This approximation is often formulated in wavelength as opposed to frequency and is called the Sellmeier equation (Eq. 2.16)

$$n^2(\lambda) = 1 + \sum_i \frac{B_i \lambda^2}{\lambda^2 - C_i} \tag{2.16}$$

Here B_i and C_i are experimentally determined parameters that determine the strength and location of the ith resonance respectively. As will be explored in the next section, the shape of this function has strong implications on how ultrashort laser pulses are effected through propagation in a dielectric. A large catalog of the index of refraction of many materials is hosted on Ref. [64].

2.1.2 Dispersive effects

Ultrashort laser pulses are not monochromatic, and (restricting our attention to the time domain) can be thought of as consisting of plane waves over a band of frequencies referred to as a bandwidth. When the peaks of these plane waves are aligned in time they are said to be at the Fourier transform limit. In this case each of the plane waves add constructively in the region near the peak, and then begin to destructively interfere farther away. The wider the bandwidth of the laser pulse, the shorter the duration of the pulse can be-and the more important dispersive effects become. Next we will follow Ref. [65] and consider the effect of a laser pulse $E_{\text{in}}(t)$ with a spectrum $\tilde{E}_{\text{in}}(\omega)$ consisting of a bandwidth of frequencies propagating through a dispersive medium. After passing through the medium, the laser pulse acquires a frequency dependent phase shift.

$$E_{\text{out}}(t) = \frac{1}{2\pi}\int d\omega\, \tilde{E}_{\text{in}}(\omega) e^{i\omega t} e^{i\varphi(\omega)} \tag{2.17}$$

The physical reason for this frequency dependent phase shift in dielectric materials (ie. fused silica) is the following. As an oscillating electric field passes through a dielectric, it polarizes the molecules setting them into oscillatory motion. The acceleration of the of these charges radiates new fields. The superposition of the new field interfering with the initial field produces a new overall combined field which is equivalent to a phase shift of the initial field [63]. Frequency components that are closer to the material resonances drive stronger oscillations and therefore produce stronger newly radiated fields resulting in a larger phase shift for a given frequency. The magnitude of this phase shift is encoded in the index of refraction. When passing through a medium of length L, the total phase shift of a laser pulse as a function of frequency can be written

$$\varphi(\omega) = \beta(\omega)L = n(\omega)\frac{\omega}{c}L. \tag{2.18}$$

Here $n(\omega)$ is the familiar index of refraction explored in the previous section, and $\beta(\omega)$ is the propagation constant. The total phase shift as can be expanded around the carrier frequency ω_0 of the pulse in a Taylor series to approximate its functional form. Since the first few terms are often dominant, this simplification can make the total phase shift more manageable, and give physical insight into how the material dispersion will alter the pulse by considering the effect of each term.

$$\varphi(\omega) = \varphi_0 + \left.\frac{\partial\varphi}{\partial\omega}\right|_{\omega_0}(\omega-\omega_0) + \left.\frac{\partial^2\varphi}{\partial\omega^2}\right|_{\omega_0}\frac{(\omega-\omega_0)^2}{2!} + ... \tag{2.19}$$

The zeroth order phase φ_0 corresponds to an absolute phase shift and describes the phase shift of the carrier frequency within the envelope of the pulse without altering the pulse shape. While the zeroth order phase is inconsequential when there are many oscillations of the electric field within the pulse envelope, it can have a significant effect on the dynamics of laser matter interactions in relativistic single-cycle limit [3], and is commonly referred to as the carrier envelope phase or CEP. The first order phase coefficient $\partial\varphi/\partial\omega|_{\omega_0}$ on the other hand corresponds to the group delay which is a phase shift that effects the entire pulse collectively, delaying the pulse envelope in time. The second order phase is the last term that will be discussed in this section where $\partial^2\varphi/\partial\omega^2|_{\omega_0}$ is called the group delay dispersion or GDD. This is the first term that contributes a frequency dependent phase delay and therefore results in pulse broadening in the time domain. The GDD expressed in terms of the index of refraction and the carrier wavelength can be see below [65].

$$\left.\frac{\partial^2\varphi}{\partial\omega^2}\right|_{\omega_0} \equiv -\frac{\lambda^3}{2\pi c^2}\left.\frac{d^2n}{d\lambda^2}\right|_{\lambda_0} L \tag{2.20}$$

It is worth noting here that if the L is omitted from the above expression, it instead describes $\partial^2\beta/\partial\omega^2|_{\omega_0}$ which is called the group *velocity* dispersion or GVD and describes the phase shift per unit length often expressed in units of fs^2/mm (ie. ~ 36.16 fs^2/mm in fused silica for $\lambda_0 = 800$ nm). This term can be the dominant term, but depending on the functional form of the index of refraction near the carrier wavelength higher order terms can become important. Furthermore, higher order phase components become more important as the laser pulse bandwidth increases. The interested reader is directed to Refs. [42, 65, 66] for a much more detailed account of these effects than can be included here. This concludes our discussion of linear effects on pulse propagation, the next section investigates one effect in the unbelievably rich topic of nonlinear effects on pulse propagation.

2.2 Nonlinear response

As explored in the previous section, materials respond linearly to oscillating electric fields given that the fields are small. We may wonder what happens if the fields become large enough that our linear term is not enough to describe the response of the material... This is the realm of nonlinear optics. In this realm there are many different ways materials can respond to the oscillating electric fields. To get the full picture, describing simultaneous resonances (ie. two-photon, three photon etc.) one must resort to the quantum mechanical description [67]. This however is beyond the scope of this thesis work, but the interested reader is encouraged to explore Refs [68, 69]. In this chapter we will follow [70] and [67] to extend the Lorentz model to take into account higher order effects which effect the index of refraction, which will be critical for understanding the wave picture of the phenomenon experimentally investigated in this thesis.

2.2.1 The nonlinear electric susceptibility $\chi^{(3)}$

The model in the last section that the electron clouds will oscillate linearly with the driving field is only approximately true in the case where the fields are small, because no atomic or molecular potential in nature is truly described by a parabolic restoring force. One can model the nonlinear response by including new terms in the potential represented by additional terms in the polarization as shown below.

$$\mathbf{P}(\omega) = \epsilon_0 \Big[\chi^{(1)}(\omega) + \chi^{(2)}(\omega)\mathbf{E}(\omega) + \chi^{(3)}(\omega)|E|^2 + ...\Big]\mathbf{E}(\omega) \tag{2.21}$$

The second term $\chi^{(2)}$ in this equation represents contributions from a potential that has an asymmetry (ie. odd power), such as those found in the ordered lattice of some crystals.

If however, the material is composed of unordered or amorphous collections of molecules, the response of the material can be better modeled by a centro-symmetric model. Since in this thesis, we are interested in describing the nonlinear propagation in glass, we will focus our attention on $\chi^{(3)}$, which can be modeled by adding an anharmonic term to the Lorentz model, where the odd powered restoring force is the result of a an even powered anharmonic potential and has a strength parameter b [70, 67, 71].

$$\mathbf{F} = q\mathbf{E} = m(b\boldsymbol{x}^3 + \omega_0^2\boldsymbol{x} + \gamma\frac{d\boldsymbol{x}}{dt} + \frac{d^2\boldsymbol{x}}{dt^2}) \tag{2.22}$$

This equation is called the Duffing equation [72, 71, 62] and the third order response can be solved by the method presented in Refs. [71, 67] to yield.

$$\boldsymbol{x}^{(3)}(\omega_q) = \sum_{(mnp)} \frac{be^3[\mathbf{E}(\omega_m)\cdot\mathbf{E}(\omega_n)]\mathbf{E}(\omega_p)}{m^3 D(\omega_q)D(\omega_n)D(\omega_m)D(\omega_p)} \tag{2.23}$$

Where the denominator function $D(\omega_n) = \omega_0^2 - \omega_n^2 - i\gamma\omega_n$ and $\omega_q = \omega_n + \omega_m + \omega_p$ have been introduced. The subscripts m, n, and p represent three distinct electric field frequencies, since this is the most general case for third order interactions. Here again $\mathbf{P}^{(3)}(\omega_q) = -Ne\boldsymbol{x}^{(3)}(\omega_q)$ and the definition of the third order polarization is [67]

$$P_i^{(3)}(\omega_q) = \epsilon_0 \sum_{jkl}\sum_{(mnp)} \chi^{(3)}_{ijkl}(\omega_q,\omega_m,\omega_n,\omega_p)E_j(\omega_m)E_k(\omega_n)E_l(\omega_p) \tag{2.24}$$

where i,j,k,l represent the spatial coordinates x, y or z. Again the third order susceptibility can be identified as in the case of centro-symmetric media as

$$\chi^{(3)}_{ijkl}(\omega_q,\omega_m,\omega_n,\omega_p) = \frac{Nbe^4[\delta_{ij}\delta_{kl} + \delta_{ik}\delta_{jl} + \delta_{il}\delta_{jk}]}{3\epsilon_0 m^3 D(\omega_q)D(\omega_n)D(\omega_m)D(\omega_p)} \tag{2.25}$$

Equation 2.25 represents the 81 element fourth rank tensor that is the third order susceptibility with arbitrary driving frequencies [71]. If the third order nonlinear polarization is induced by a linearly polarized monochromatic plane wave of frequency ω, the induced nonlinear polarization reduces to two unique terms $P_i^{(3)}(\omega)$ and $P_i^{(3)}(3\omega)$ with the corresponding susceptibilities $\chi_{ijkl}^{(3)}(\omega, -\omega, \omega, \omega)$ and $\chi_{ijkl}^{(3)}(3\omega, \omega, \omega, \omega)$ respectively. Here the former corresponds to an increase in the refractive index, whereas the latter corresponds to third-harmonic generation [67]. Considering the term corresponding to an increase in the refractive index, the polarization can now be expressed as [73, 74]

$$P_i^{(3)}(\omega) = 3\epsilon_0 \sum_{jkl} \chi_{ijkl}^{(3)}(\omega, -\omega, \omega, \omega) E_j(\omega) E_k(\omega) E_l(-\omega) \tag{2.26}$$

where the 3 represents the degeneracy factor. There are three nonzero elements to this sum, $\chi_{1122}^{(3)}$, $\chi_{1221}^{(3)}$ and $\chi_{1212}^{(3)}$ which together sum to $\chi_{1111}^{(3)}$ [67, 71]. Finally, the third order nonlinear polarization resulting in nonlinear changes to the refractive index due to a linearly polarized monochromatic plane wave is

$$P(\omega) = 3\epsilon_0 \chi_{1111}^{(3)}(\omega, -\omega, \omega, \omega) |E(\omega)|^2 E(\omega) \tag{2.27}$$

where

$$\chi_{1111}^{(3)}(\omega, -\omega, \omega, \omega) = \frac{Nbe^4}{\epsilon_0 m^3 D(\omega)^3 D(-\omega)} \tag{2.28}$$

This final expression for $\chi_{1111}^{(3)}(\omega, -\omega, \omega, \omega)$ serves to guide our physical intuition by showing what determines its value through the anharmonic model presented by Ref. [70]. Under strongly non-resonant conditions Ref. [67] uses this formula to obtain an order of magnitude estimation for $\chi_{1111}^{(3)}$. If we claim that the restoring force due to the linear

Mechanism	n_2 [cm^2/W]	$\chi^{(3)}_{1111}$ [m^2/V^2]	Resp. time [sec]
Electric polarization	10^{-16}	10^{-22}	10^{-15}
Molecular orientation	10^{-14}	10^{-20}	10^{-12}
Electrostriction	10^{-14}	10^{-20}	10^{-9}
Saturated atomic absorption	10^{-16}	10^{-8}	10^{-8}
Thermal effects	10^{-6}	10^{-12}	10^{-3}

Table 2.1: Typical time scales for changes in the refractive index due to many different effects

and nonlinear terms in Eq. 2.22 will become comparable as the displacement approaches the lattice spacing d, (ie. $mbd^3 = m\omega_0^2 d$) then we can obtain an estimate of $b \approx \omega_0^2/d^2$. Additionally, far from resonance we can approximate $D(\omega_0) = \omega_0^2$, and the number density is $N = 1/d^3$. Using these approximations with $d = 0.3$ nm and $\omega_0 = 7 \times 10^{15}$ rad/sec one obtains the following approximation for $\chi^{(3)}_{1111}$.

$$\chi^{(3)}_{1111} \approx \frac{e^4}{d^5 \epsilon_0 m^3 \omega_0^6} = 3.5 \times 10^{-22} [\frac{\mathrm{m}^2}{\mathrm{V}^2}] \tag{2.29}$$

This approximation turns out to be of the same order of magnitude as many experimentally determined values, for example in fused silica $\chi^{(3)}_{1111} \approx 1.86 \times 10^{-22} [\frac{\mathrm{m}^2}{\mathrm{V}^2}]$. It turns out there are several other $\chi^{(3)}_{1111}$ effects that can affect the index of refraction other than the electronic polarization explored in this chapter. Each of these effects occur on different characteristic timescales, as conveniently summarized in Table 2.1 from Ref. [67].

For the purposes of this thesis work, we will focus our attention on changes in the index of refraction by electronic polarization. This effect occurs on ultrashort ($10^{-15} - 10^{-16}$ fs) timescales relevant to ultrashort pulse compression often referred to in the literature as "instantaneously." Critically, this means that the nonlinear index of refraction changes on timescales shorter than our typical pulse durations ($3 - 5 \times 10^{-14}$ fs).

The main insight from this chapter is that a decent approximation of $\chi^{(3)}_{1111}$ can be made by adding a simple anharmonic term to the potential of the Lorentz bound electron model. It is also noted here that in the laboratory these approximations are almost never used quantitatively, instead the $\chi^{(3)}$ or n_2 are measured under the relevant conditions (timescale, materials, polarizations etc.).

This of course is not the whole story for $\chi^{(3)}$ by any means, and there are entire fields of study dedicated its unique effects on various timescales and in different materials. To delve into much more detail than could be presented in this thesis, the interested reader is encouraged to explore Refs. [71, 69, 68, 75] which should serve as a powerful jumping off point to more specific inquiries. For the remainder of this thesis the $\chi^{(3)}_{1111}$ corresponding to contributions from electronic polarization relevant on ultrafast timescales will be referred to as simply $\chi^{(3)}$.

2.3 Intensity dependent refractive index

Now that we have a sense of where $\chi^{(3)}$ comes from, we will explore one of its effects. It will be shown that nonlinear changes in the index of refraction can prove to be very useful in application to ultrashort pulse compression. On the other hand, nonlinear spatial effects (transverse to the beam propagation direction) can lead to effects such as filamentation and wave collapse. As explored in the previous section, centro-symmetric media exhibit inversion symmetry and do not have odd anharmonic terms in their nonlinear potential. As such, up to the first order of nonlinearity, the polarization can be expressed as Eq. 2.30 [74, 67]

$$\mathbf{P}(\omega) = \epsilon_0 \Big[\chi^{(1)}(\omega) + 3\chi^{(3)}(\omega)|E|^2\Big]\mathbf{E}(\omega) = \epsilon_0 \chi_{eff}(\omega, |E|^2)\mathbf{E}(\omega) \tag{2.30}$$

where

$$n^2(\omega, |E|^2) = 1 + \chi_{eff}(\omega, |E|^2) \tag{2.31}$$

and

$$n_0^2(\omega) = 1 + \chi^{(1)}(\omega) \tag{2.32}$$

substituting Eq. 2.32 into Eq. 2.31 and solving for $n(\omega)$ yields

$$n(\omega, |E|^2) = n_0(\omega)\left(1 + \frac{3\chi^{(3)}(\omega)|E|^2}{n_0^2(\omega)}\right)^{1/2} \tag{2.33}$$

However in the case that $\chi^{(3)}(\omega)|E|^2/n_0^2(\omega) << 1$ This expression can be approximated by

$$n(\omega, |E|^2) \approx n_0(\omega)\left(1 + \frac{3\chi^{(3)}(\omega)|E|^2}{2n_0^2(\omega)}\right) \tag{2.34}$$

Recalling that $I = 2n_0(\omega)\epsilon_0 c|E|^2$, Eq. 2.34 can be re-written in the following form,

$$n(\omega, I) \approx n_0(\omega) + \frac{3\chi^{(3)}(\omega)}{4n_0^2(\omega)\epsilon_0 c} I \tag{2.35}$$

giving rise to the common form of the optical Kerr effect

$$n(\omega, I) \approx n_0(\omega) + n_2(\omega)I \tag{2.36}$$

where [67]

$$n_2(\omega)\Big[\frac{\mathrm{m}^2}{\mathrm{W}}\Big] \equiv \frac{3}{4n_0^2(\omega)\epsilon_0 c}\chi^{(3)}(\omega)\Big[\frac{\mathrm{m}^2}{\mathrm{V}^2}\Big]. \tag{2.37}$$

As shown above, n_2 is a function of ω and is generally only experimentally determined at a few locations in frequency space for various materials due to the complexity in the modeling of the nonlinear response of the dielectric. That being said, it should be noted that empirical relationships have been determined that predict $\chi^{(3)}(\omega)$ reasonably well and could serve as a guide to choosing materials with larger nonlinear response [74].

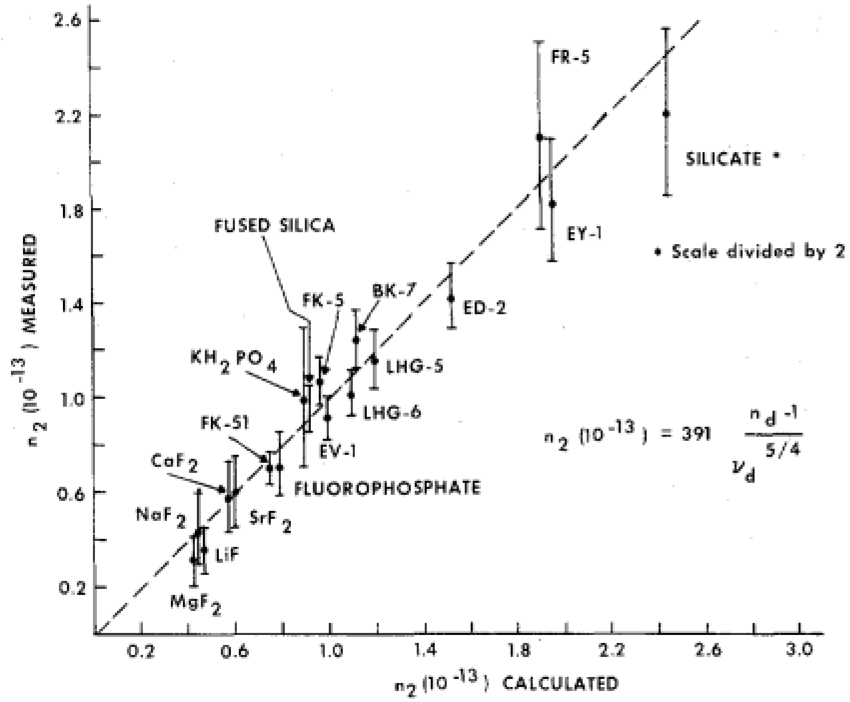

Figure 2.1: graphical representation of the empirical relationship for predicting the nonlinear index of refraction n_2 in many materials. Note that n_2 is given in ESU.

In [74] a detailed derivation of a predictive formula for n_2 was developed in dielectrics taking into account the local field correction. However, ultimately a simpler empirical formula was found to better fit the data as shown in Fig. 2.1. The next section will explore the effects of an increasing index of refraction in the time domain on ultrashort laser pulses.

2.3.1 Self-phase modulation

As explored in the previous section, when high intensity laser pulses interact with matter, they can lead to changes in the refractive index of the material. This change in the refractive index due to electronic polarization of the electrons occurs on the femtosecond timescale as seen in Table 2.1. The full treatment of intense ultrashort pulse propagation in matter requires simulations involving the nonlinear Schrödinger equation. Here we restrict our attention however, to a simple case where loss terms and dispersion can be neglected. Consider an intense ultrashort (30-50 fs) laser pulse with a gaussian temporal profile traveling through a very thin (sub-millimeter) fused silica wafer at Brewster's angle. The linearly polarized electric field of such a pulse can be defined by

$$E(z,t) = E_0 e^{-2\ln(2)t^2/\tau^2} e^{i\phi} \tag{2.38}$$

Here $\phi = \omega_0 t - kz$, where $k = 2\pi n(I)/\lambda_0$ and τ is the full width at half max of the intensity profile. Now by substituting the modified index of refraction into the phase term we obtain the following expression for the phase including the nonlinear term. I have explicitly included the time dependence as a reminder that the phase shift is local within the pulse envelope.

$$\phi(t) = \omega_0 t - \frac{2\pi}{\lambda_0}(n_0 + n_2 I(t))z \tag{2.39}$$

The magnitude of the phase change arising from the nonlinear index of refraction can be seen below in Eq. 2.41. Different parts of a gaussian pulse experience a different index of refraction locally in time as the pulse passes through matter (ie. the center of the pulse where the intensity is highest, will experience a higher index of refraction than the wings of the pulse during propagation). In other words, the phase is modulated by the intensity envelope of the laser pulse itself, giving credence to the name self-phase modulation (SPM).

$$\Delta\phi(t) = \frac{2\pi}{\lambda_0} n_2 I(t) z \tag{2.40}$$

In this case since the temporal intensity profile is gaussian, this leads to a gaussian phase shift. Further, since $\omega_{\text{inst}}(t) \equiv d\phi/dt$,

$$\omega_{\text{inst}}(t) = \omega_0 - \frac{2\pi}{\lambda} n_2 \frac{dI(t)}{dt} z. \tag{2.41}$$

The remarkable thing about this process is in the center of the pulse, the intensity envelope and therefore the nonlinear phase shift acquired is roughly quadratic. This means that a linear change in the instantaneous frequency has been added to the pulse (ie. a linear chirp). An example of an extreme case of SPM spectral broadening ($B \sim 21$) is shown below in Fig. 2.2 so that the change in the instantaneous frequency is resolvable to the eye. The electric field of the laser pulse after SPM can be seen with a clear frequency chirp with lower frequencies at earlier times and higher frequencies at later times.

Changing the instantaneous frequency of a transform limited pulse without changing its duration means more frequencies were added to the pulse as seen in Fig. 2.2. A broader bandwidth implies that we have a narrower transform limited pulse duration by the time-bandwidth product. Furthermore, since the frequencies constituting this bandwidth have a linear chirp over most of the temporal duration, they can be re-arranged using dispersive optics (ie. chirped mirrors), which can undo the linear frequency chirp. This is the basic physics governing optical pulse compression in the time domain.

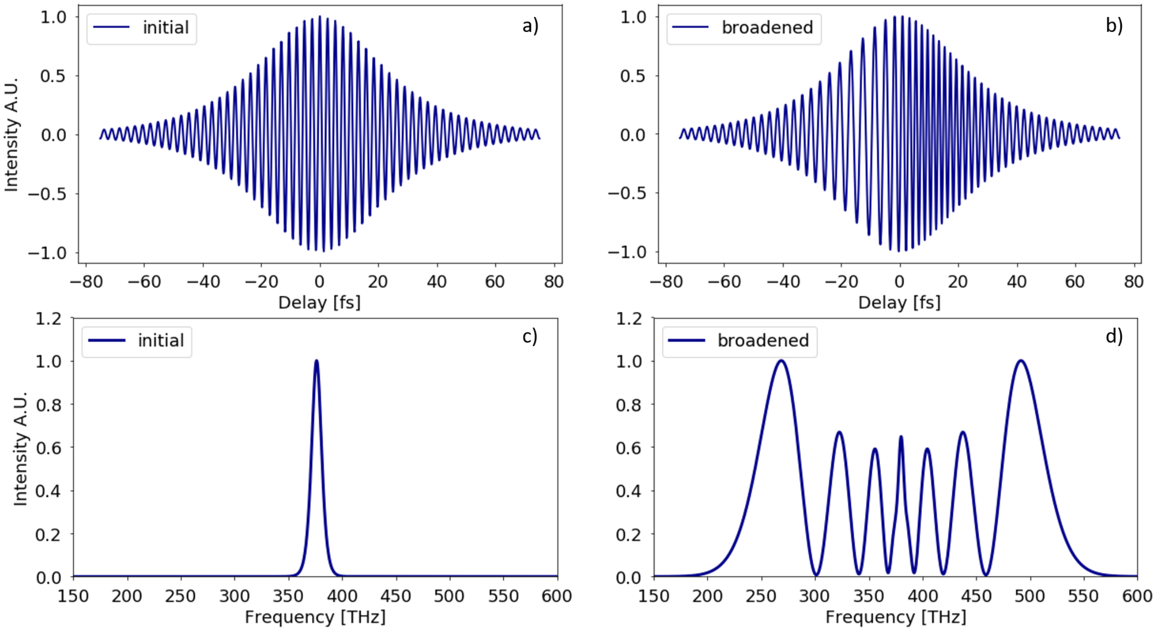

Figure 2.2: The electric field of an ultrashort laser pulse before (a) and after (b) a nonlinear phase shift from SPM. The Fourier transform of the initial (c) and spectrally broadened (b) laser pulse can be seen below their respective laser pulses.

2.3.2 Self-focusing

Although the temporal effects of the nonlinear refractive index explored in the previous section are extremely beneficial for pulse compression, the nonlinearity also has spatial manifestations as mentioned in Chap. 1. As was the case in time, local differences in the intensity profile as a function of space can give rise to a lensing effect due to local changes in the index of refraction. Since the on-axis portion of the beam experiences a larger index of refraction than its periphery, the phase velocity is lower on-axis. Further, since optical rays propagate normal to the wavefront, they converge on axis therefore producing a lensing effect. This process was first predicted in the early 1960s and observed experimentally shortly after [36, 15]. It was shown that this lensing effect can lead to so-called catastrophic beam collapse when the laser power exceeds a certain threshold called the critical power P_{cr} [36, 76, 77, 78].

$$P_{cr} = \pi(0.61)^2 \frac{\lambda_0^2}{8n_0n_2} \tag{2.42}$$

For example in a *long enough medium* there is a critical power P_{cr} such that if $P < P_{cr}$ the laser pulse will always ultimately spread out due to diffraction, whereas if $P > P_{cr}$ the beam will always collapse catastrophically to a small point [79, 65]. The critical power then defines the point at which the nonlinear self-focusing just compensates the beam spreading due to diffraction [79, 67]. Above the critical power, gaussian beams collapse to an on-axis filament after propagating a distance of

$$z_f = \frac{\pi \mathrm{w}_0^2}{\lambda_0}\Big(\frac{P}{P_{cr}} - 1\Big)^{-1/2}. \tag{2.43}$$

It is interesting to note that regardless of the input beam, the beam has been shown to collapse into a self-similar Townes profile [80]. On the other hand, if the material inducing the nonlinearity is very thin (ie. the profile of the beam is not significantly modified), the optic can instead be modeled as a geometric lens [79], as further discussed in Chap. 4. It is also noted here that Kerr lensing still occurs below the critical power as is the case with passive mode-locking schemes like Kerr lens mode-locking (KLM) [79, 65].

In addition to whole-beam self-focusing, high power laser pulses are also susceptible to small-scale filament formation when propagating through a nonlinear medium. This type of small-scale spatial nonlinearity (initiated by noise in the intensity profile) is typically the dominant effect in flat-top beam profiles where the large scale intensity gradients tend to be smaller making the collapse dynamics are slightly different [81]. A small region of higher intensity (ie. noise) in the beam profile raises the index of refraction locally, which focuses light toward it and raises the intensity even higher [79]. This process has been modeled as an instability by Ref. [82] where the growth rate of these modulations was found to be $g_m = 2\pi n_2 I/\lambda_0$ [79, 83]. Integrating over the entire length of the nonlinear medium yields the "B-integral."

$$B = \frac{2\pi}{\lambda_0} \int_0^L n_2 I(z) dz \tag{2.44}$$

The value of the B-integral specifies the total nonlinear phase shift over the length of the nonlinear medium where the amplitude of the small-scale modulations grow according to $G = e^B$ [79, 16]. Spatially filtering before and after the nonlinear interaction can ensure that the input noise is minimized, and that the growth of the filaments can be mitigated be removing the high frequency components with an appropriately sized pinhole after the interaction [79]. In the context of ultrafast pulse compression, these techniques as mentioned in Ref. [24] will likely be very important to obtain the highest quality pulse compression and extend the compression to multiple stages as explored in Chap. 9.

Chapter 3

Methods/laser diagnostics

This section briefly outlines the various diagnostic tools developed for the experimental studies. It also includes several applications of these diagnostics to calibrating and characterizing various pieces of equipment.

3.1 Second harmonic generation FROG

In pursuing pulse compression of ultrashort high intensity laser pulses, accurate measurements of pulse length are of critical importance. This statement may seem obvious but it makes the process no less trivial. Typically to record an event, you need to take measurements at a faster rate. This becomes very difficult on the femtosecond timescale. For a sense of scale, one femtosecond ($\sim 10^{-15}$ s) is to a minute ($\sim 10^{1}$ s), as one minute is to the age of the universe ($\sim 10^{17}$ s). Typically to measure these events a method called an intensity autocorrelation is used. A beam-splitting optic is utilized to create a clone of the laser pulse. The laser pulse and its clone are then overlapped inside a nonlinear crystal such as Beta-Barium Borate (BBO) and generate a new signal when the beams are overlapped in space and time. One can then delay the clone pulse by increasing the path-length using a translation stage in very small increments $O(1\mu m)$ thereby scanning across (gating) the laser pulse. When the pulses no longer overlap, the second harmonic signal due to their overlap will disappear. The distance the stage moves in this process gives you an idea of the length of the laser pulse. This measurement is called an intensity auto-correlation and can serve as a pulse measurement, assuming a pulse structure.

A similar but slightly more complicated technique is called Frequency Resolved Optical Gating (FROG). In the case of the scanning second harmonic generation FROG, the process is nearly identical except that instead of only recording the intensity of the second harmonic signal you also record its spectrum. In other words - you frequency resolve the optical gating. Figure 3.1 shows a schematic and photo of an example of such a diagnostic. Many more details can be found in Ref. [66].

In Fig. 3.1, an input beam is aligned through irises and split into a *reference line* and a *delay line*. The delay line has a variable path length by use of a retro-reflecting mirror pair on a motorized delay stage. The reflective optics used to guide the beam are either gold (Au) or silver (Ag). The set of laser pulses are then focused and overlapped inside the nonlinear crystal to generate the second harmonic signal. BBO is manufactured to phase match a certain input wavelength and needs to be oriented correctly to generate efficient SHG (For Type I BBO at 800nm needs to be cut at 29.2 deg). This means that mounting the BBO in a rotation mount is generally a good move. Sometimes the angle of the cut may need to be determined for the vendor, using software such as SNLO can be critical in these cases. The thickness of the crystal also determines how much spectrum it can phase match. Using a thicker crystal will increase the second harmonic signal, but it also limits the amount of bandwidth you can phase match - ultimately limiting the duration of pulses you can measure with FROG. The crystal thickness generally needs to be matched with the application, and one can determine the phase matching bandwidth

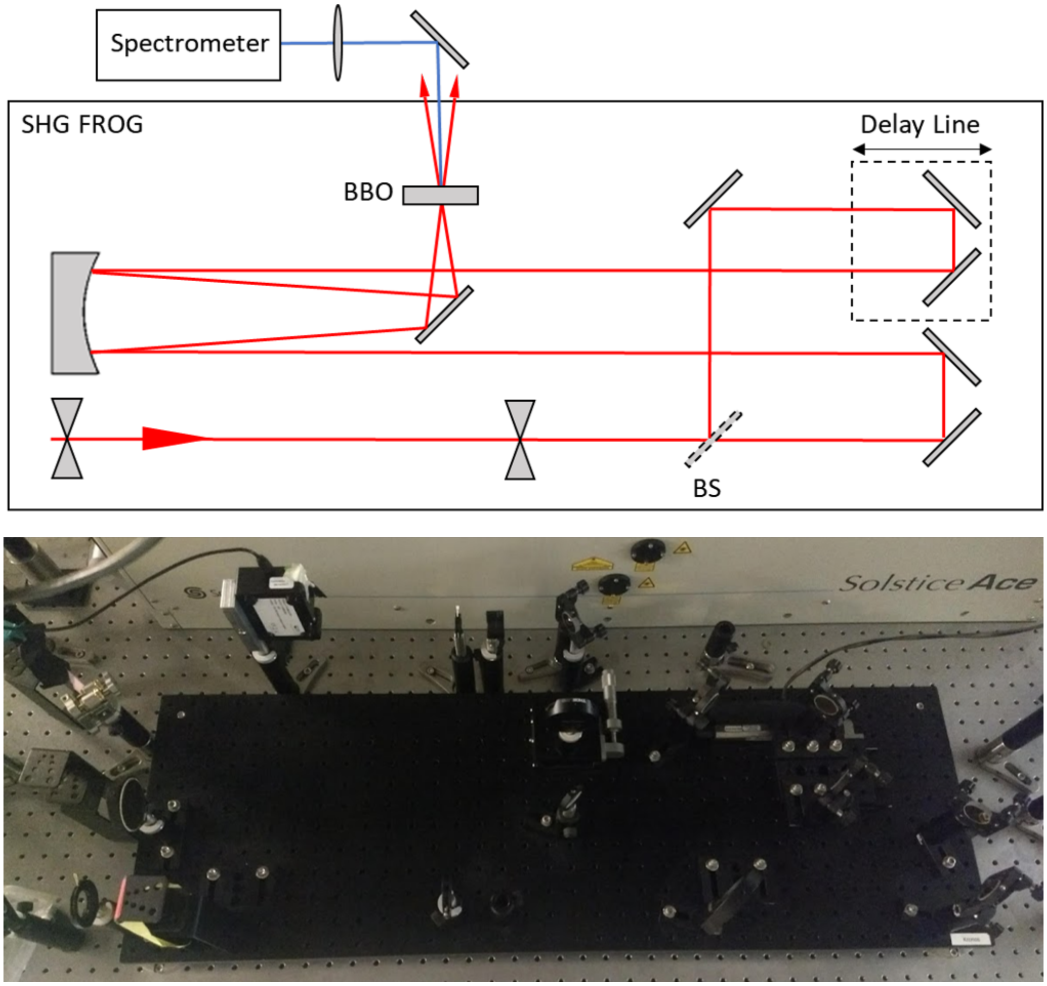

Figure 3.1: Shown above is a schematic representation (top) and a photo (bottom) of the SHG scanning FROG device

afforded by a certain crystal thickness with the following formula [66].

$$\Delta\lambda_{\text{FWHM}} = \frac{0.44\lambda_0}{|n'(\lambda_0) - \frac{1}{2}n'(\frac{\lambda_0}{2})|} \tag{3.1}$$

Here n' refers to the first derivative of the Sellmeier equation, and λ_0 refers to the carrier wavelength of the laser pulse. In this case the laser wavelength is $\sim$ 800 nm which means the second harmonic is blue at $\sim$ 400 nm. In this case the light exiting the BBO consists of two blue beams that represent the SHG signal coming from each intense laser pulse. Furthermore, when the focal spots of the laser pulses are overlapped in space and time in the nonlinear crystal a third blue beam will appear between the other two. CAUTION: Care must be taken to ensure that the intensity of the focused beams is low enough so that BBO does not burn - it typically costs ∼ $500-1000 and can take weeks of lead time to grow and acquire. This central signal is then directed by an aluminium (Al) mirror and focused onto the spectrometer slit using an A-coated lens to record its spectrum at each delay position to build a two-dimensional dataset which is called a spectrogram. An example of a spectrogram can be seen below in Fig. 3.2 (a) and (b). By making the assumption that the pulse is finite in both frequency and time this two-dimensional data set can uniquely determine the intensity and phase of the laser pulse through the process of "2D phase retrieval" [84]. Herein lies the strength of the FROG technique over a simple autocorrelation.

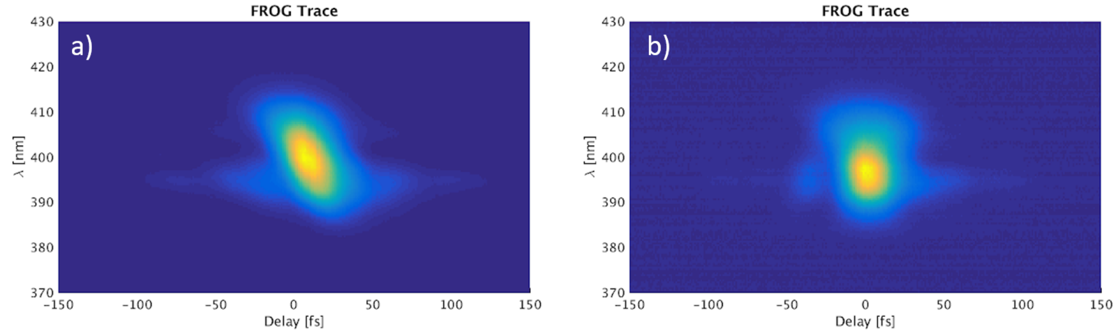

Figure 3.2: Shown above is a sample spectrogram of an 800 nm laser pulse using an ultrafast fused silica beam splitter (a) and a pellicle beam splitter (b). The fused silica beam splitter adds some dispersion to the reference line giving rise to the angled trace in (a), whereas the pellicle does not

It is critical to note that all the optics in the FROG are reflective up until the nonlinear crystal. This is because dispersion plays a large role in ultrashort laser pulse propagation in dielectrics as explored in the previous sections, and can significantly alter the pulse length before the pulse measurement. A striking example of this can be seen in Fig. 3.2. Figure 3.2 (a) is an example of a spectrogram taken while using a fused silica beam splitter. This spectrogram asymmetry is normally not possible in the SHG process [66] and is indicative of a difference in Group Delay Dispersion (GDD) between the delay and the reference pulse. This asymmetry can be corrected with post-processing, or alternatively one can use a very thin beam splitter (pellicle beam splitter) in place of the fused silica beam splitter, where the dispersion is negligible at the cost of some stability.

3.2 Compressor calibration

As mentioned in the previous section, SHG FROG determines the phase of the laser pulse. This is very convenient in calibrating devices such as a compressor grating. Such a device can be used to vary the amount of GDD in a laser pulse. As explored in Chap. 2 the GDD concerns the second order term in the expansion of phase about the carrier frequency.

$$\varphi(\omega) = \varphi_0 + \left.\frac{\partial \varphi}{\partial \omega}\right|_{\omega_0} (\omega - \omega_0) + \left.\frac{\partial^2 \varphi}{\partial \omega^2}\right|_{\omega_0} \frac{(\omega - \omega_0)^2}{2!} + ... \tag{3.2}$$

Recall GDD $\equiv \partial^2\phi/\partial\omega^2$. One can then numerically fit to the measured phase (in the region where the spectrum is non-zero) to determine the GDD of the laser pulse, where the coefficient of the ω^2 term is the relevant quantity.

$$\phi(\omega) = a + b\omega + c\omega^2 \tag{3.3}$$

It can be seen upon inspection of Eqs 3.2 and 3.3 that $c \equiv GDD/2$. It is also worth noting here that the sign of the measured quadratic phase is arbitrary in SHG FROG and requires other processes to retrieve the arrow of time. For example, one could introduce a fused silica window to the pulse and observe the change in the quadratic phase. If the magnitude of the quadratic phase becomes larger this means that the beam was originally positively chirped, whereas if the magnitude of the quadratic phase becomes smaller this means the pulse was initially negatively chirped. Alternatively higher order nonlinear processes such as self-phase modulation also have unique spectral responses depending on the sign of quadratic chirp-allowing one to determine the sign of quadratic chirp by inspection of the modulated spectrum, which will be discussed in Chap. 8 A typical chirped pulse can be seen in Fig. 3.3 where the spectrum (blue) and the spectral phase (green) and a fit to the second order phase (red-dotted) are plotted.

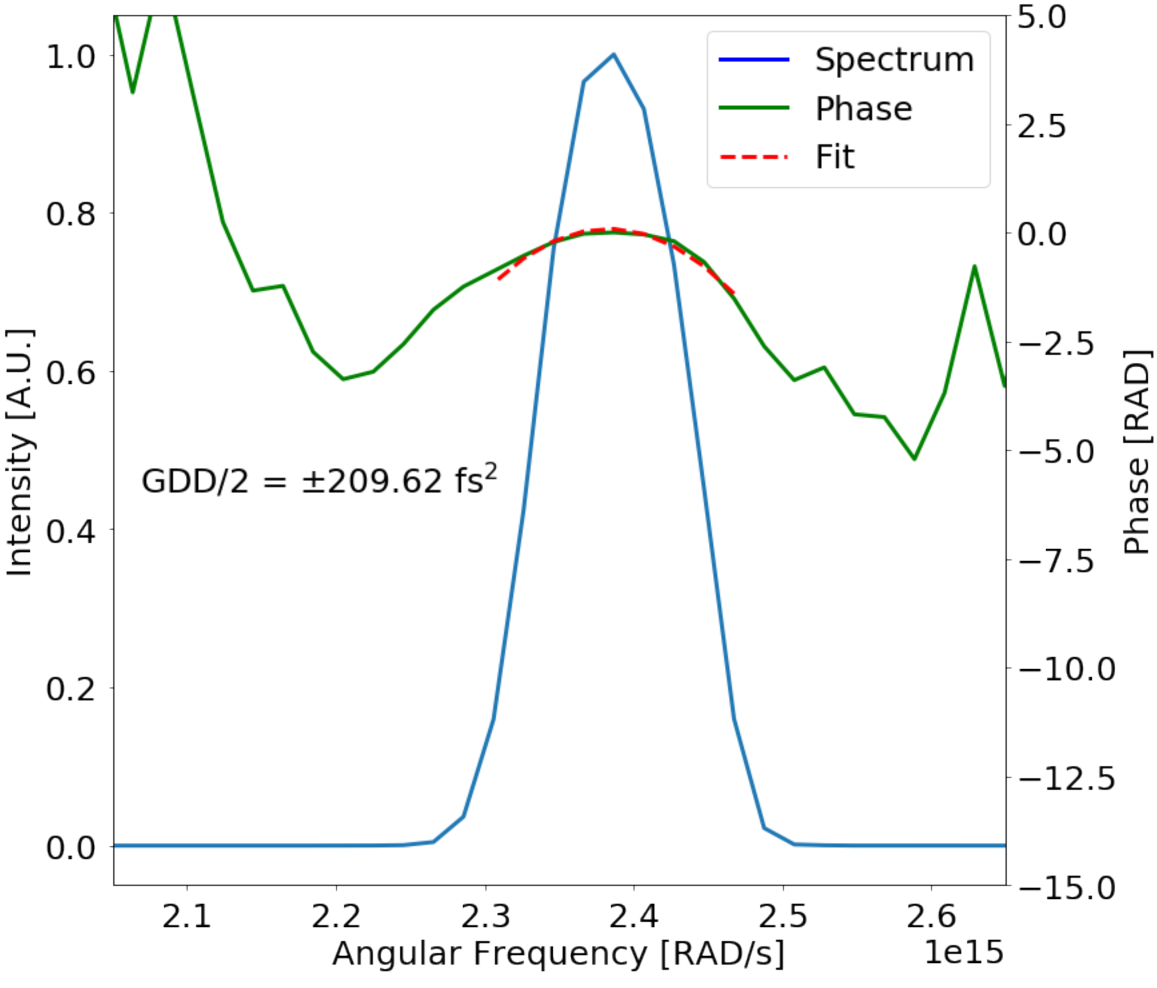

Figure 3.3: Shown above is a sample spectrum and phase of a laser pulse by SHG FROG with strong quadratic phase (a linearly chirped pulse) with $\sim$ 420 fs^2 of GDD

By varying the compressor grating separation and taking SHG FROG measurements at each compressor position, one can retrieve the GDD per actuator position and ultimately the location of the shortest pulse. The green curve in Fig. 3.4 (a) shows the fwhm of the retrieved pulse duration from SHG FROG as a function of actuator position - where the shortest pulse occurs $\sim$ 5295. The orange data series in Fig. 3.4 (b) shows the fitted quadratic spectral phase as a function of actuator position - where the phase is determined by the method shown in Fig. 3.3. By fitting a line to the retrieved quadratic phase versus actuator position we acquire a compressor calibration of ~ -7.91 fs^2/actuator position. Note that the fit to the quadratic phase crosses zero at the location of the shortest pulse. This is what we expect since the pulse should be shortest when there is no chirp. This particular scan was performed during a time when the compressor grating was slightly unoptimized, leading to third order phase in the pulse. This is evident not only in the slightly above spec ($\sim$ 35 fs) minimum pulse duration of $\sim$ 37 fs, but also in the asymmetry in the orange data series in Fig. 3.4 (b). When near zero, the quadratic fit is picking up on third order terms leading to a slight asymmetric wiggle in the linear trend. The compressor has since been optimized for minimizing this third order contribution, but I include it here in case others discover a similar thing.

In addition to calibrating the compressor itself, the phase compensation of the chirped mirrors used in the UCI compression experiments were also characterized. While this can in principle be done with a single FROG measurement, by taking a compressor scan one can minimize the error in a single measurement. At a later date when the compressor was optimized so as to minimize the third order phase, another scan was done with the chirped mirrors in the beam. The blue curve in Figure 3.4 (a) again shows the fwhm of the pulse duration as a function of compressor position, whereas the blue data series in Fig. 3.4 (b) again refers the the quadratic phase as a function of compressor position. The difference in quadratic chirp in the green dotted calibration curves at the actuator position 5250 is $\sim -251 - 332.5 = -583.5$ fs^2. This agrees reasonably well with the HD58 ultrafast innovations datasheet (http://www.ultrafast-innovations.com/product.php?name=HD58).

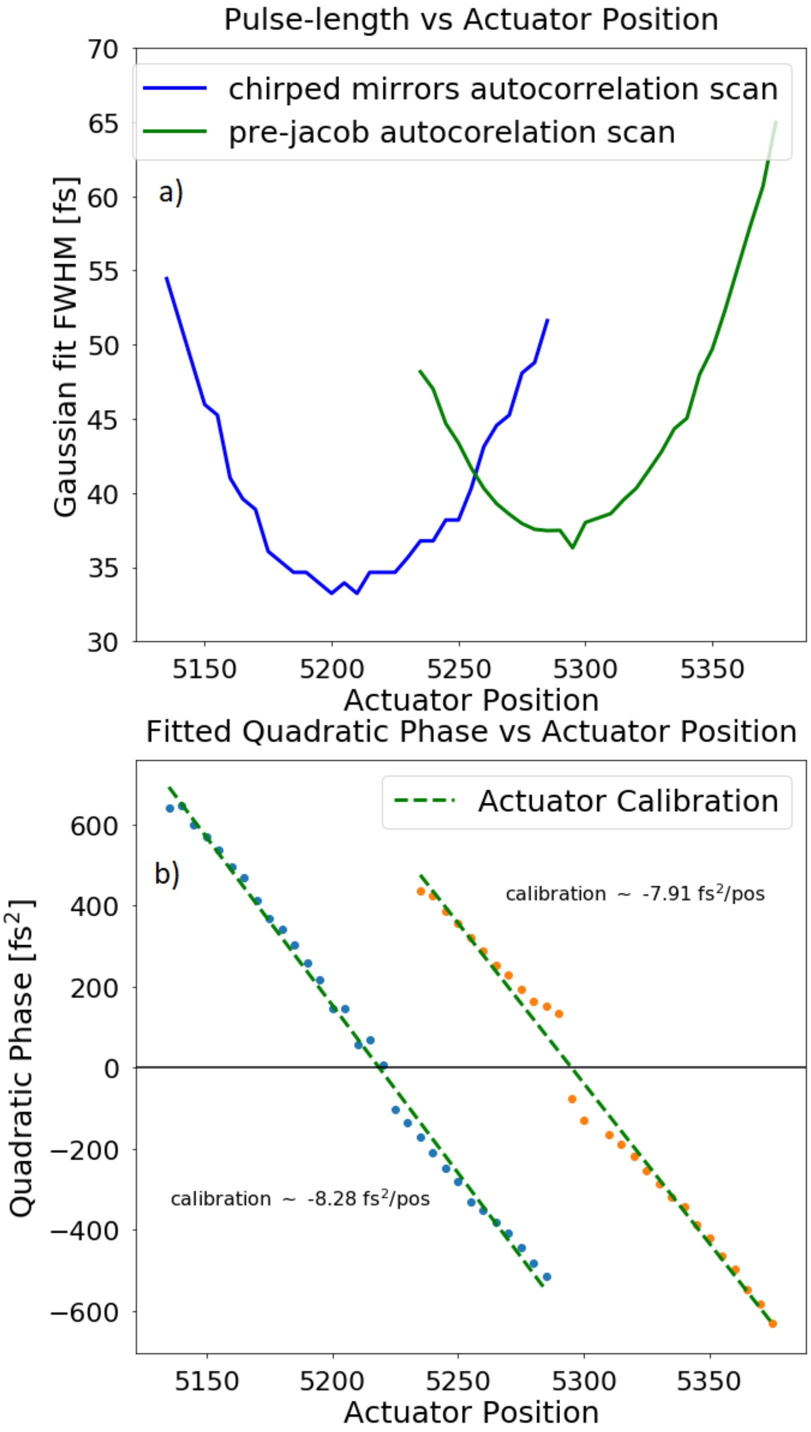

Figure 3.4: Calibration of pulse duration (a) and phase (b) versus actuator position with and without chirped mirrors in the beam. The blue line in (a) and blue data series in (b) represent the autocorrelated pulse duration, and quadratic phase as a function of compressor position with chirped mirrors in the beam. Whereas the green line in (a) and orange data series in (b) represent the autocorrelated pulse duration and quadratic phase of the laser system.

Chapter 4

Demonstration of thin film compression

4.1 Introduction

In the following sections the process of ultrashort laser pulse compression is investigated experimentally on three separate laser systems with different mode types (ie. gaussian and flat-top) and a range of energies ($\sim$ 7mJ - 2J). The scheme for pulse compression is TFC, as discussed in Chap. 1. Each laser system has a central wavelength of $\sim$ 800 nm and a pulse duration of $\sim$ 35-50 fs. Though these laser systems have a variety of different energies and mode types, the spectral broadening observed is similar, due to the similarity of the collimated intensity ($\sim$ 1 TW/cm^2). Proof-of-principle experiments are carried out in bulk fused silica at UCI. These experiments demonstrate a power amplification, and that spectral broadening and phase manipulation using chirped mirrors can be achieved to compress pulses to nearly half the original pulse duration (to 20 fs). Two other ultrafast pulse compression studies were carried out at the Center for Ultrafast

Optical Science (CUOS) on the HERCULES laser, and the LASERIX facility at the Université Paris-Sud. The HERCULES experiment was designed to investigate how the laser far field changes under the influence of self-phase modulation of a flat-top beam profile in a 0.5 mm fused silica wafer. The experiment at the LASERIX facility was a longer campaign and investigated the effect of inducing SPM in different materials on pulse compression as well as the effect of scaling the laser pulse energy, with primary experimental attention on the temporal characterization.

4.2 Pulse compression in fused silica windows (UCI)

The initial compression experiment at UCI was set up according to Fig. 4.1. High intensity laser pulses ($\sim$ 0.3 TW/cm^2) with a 1/e^2 beam diameter ($\sim$ 11.7 mm) were spectrally broadened in two 4 mm fused silica windows installed on flipper mounts and oriented at Brewster's angle (nearly 10 mm of fused silica when accounting for refracted path length) and re-compressed using 2x HD58 Ultrafast Innovations (-250fs^2) chirped mirrors. It is noted here that recent work has been done to adapt the TFC technique to Gaussian laser systems by the use of concave optics [85, 86, 87]. This takes advantage of the fact that spectral broadening through SPM is dependent on both intensity and target thickness, but the focus of this initial study was to demonstrate high throughput and compressibility of laser pulses with simple fused silica windows oriented at Brewster's angle. By measuring the power with a power meter with and without the the Brewster windows, the power throughput is measured to be $\sim$ 99%, implying the process of spectral broadening is remarkably efficient. The far field and temporal profile of the beam after this interaction was measured by a CMOS camera and a SHG FROG (as described Chap. 3) respectively.

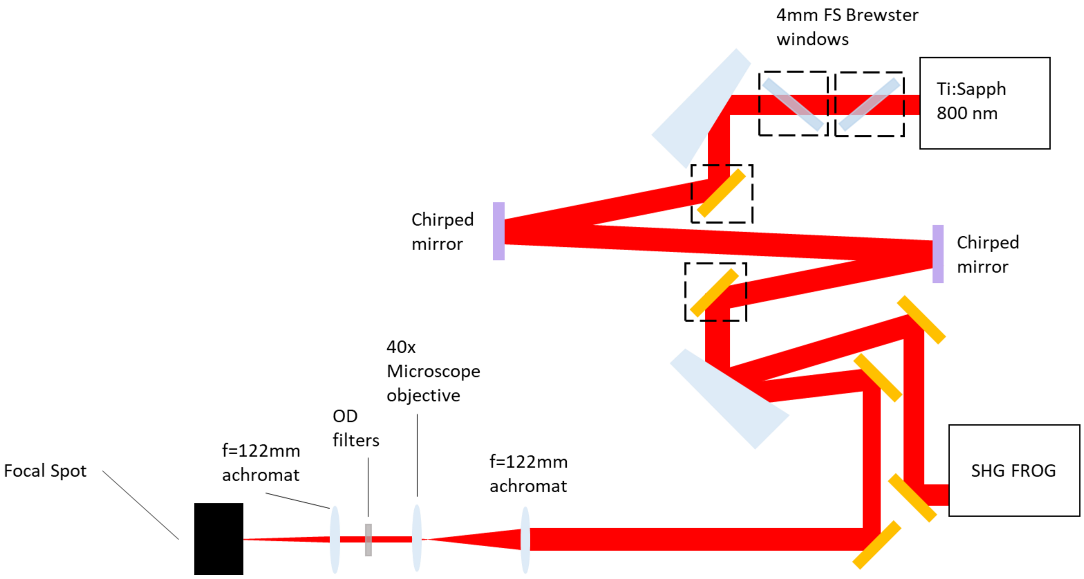

Figure 4.1: Shown above is the schematic for the pulse compression in bulk fused silica experiment. Laser pulses are spectrally broadened in fused silica, and the chirp due to SPM and GVD is compensated with chirped mirrors. The focal spot and the temporal duration are then characterized by a CMOS camera and an SHG FROG respectively. The optics surrounded by dashed lines are installed on flipper mounts or kinematic bases and were removed to take reference shots.

The beam is then split to each diagnostic with a wedge. The front reflection is directed to the SHG FROG, and the back-reflection is directed to the far-field imaging setup. Due to the gaussian intensity profile, the beam is irised before going into the FROG, therefore the duration measurements pertain to the central part of the mode. Figure 4.2 shows the measured spectrogram (FROG trace) of the initial (a) and compressed (b) laser pulses and their associated autocorrelated pulse durations (c) and (d) respectively. The spectrogram shows spectral broadening as well as a temporal narrowing, indicating that SPM in the fused silica has generated new frequencies, and those frequencies have been brought into phase with the chirped mirrors to construct a shorter pulse.

Figure 4.3 shows the laser spectrum before and after spectral broadening (a) measured directly by a spectrometer, and the reconstructed pulse duration (b) before and after compression by chirped mirrors.

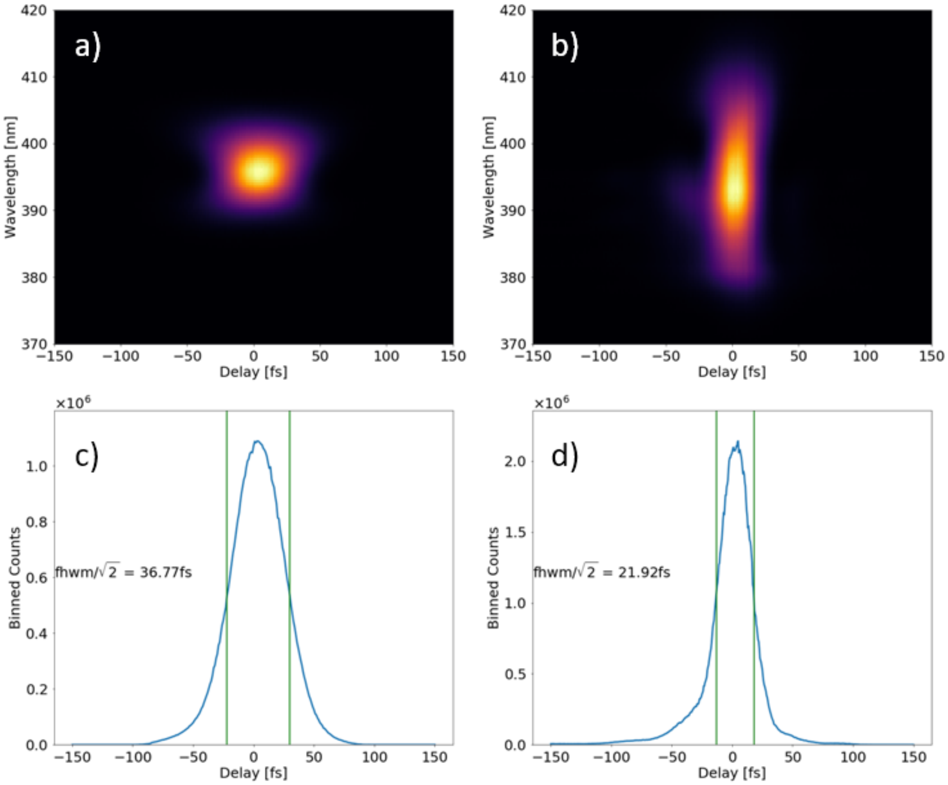

Figure 4.2: The measured spectrograms before (a) and after (b) pulse compression, and the associated autocorrelated pulse durations (c) and (d).

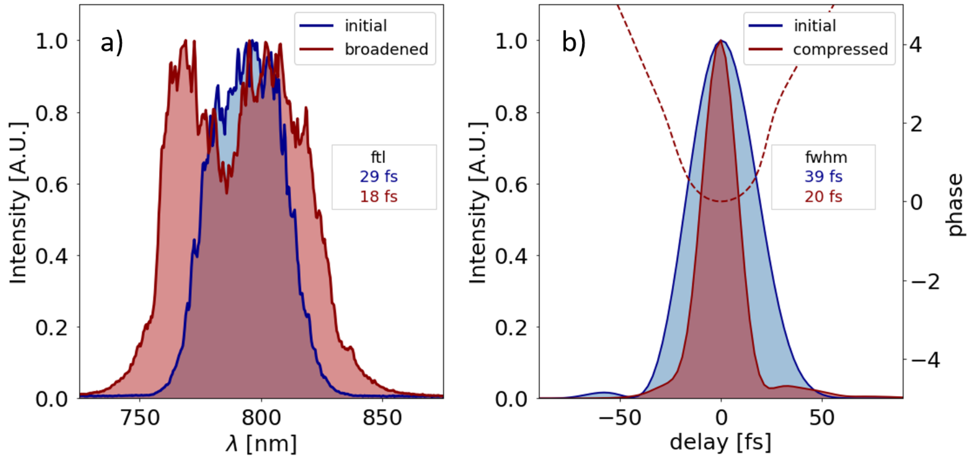

Figure 4.3: Shown above is the spectrum (a) and the pulse duration (b) of the initial (blue) and compressed (red) pulse. The residual phase after compression (b) red-dashed shows a remaining quadratic component that could be further compressed toward the analytical ftl.

The pulse duration is compressed to 20.2 ± 0.27 fs (red) (originally 39 fs (blue)) as shown in Fig. 4.3 and the phase measurement of the compressed pulse indicates that the residual phase is predominantly quadratic (Fig. 4.3 red - dotted). This means that with more suitable chirped mirrors the pulse can be compressed further to the FTL, which was calculated from the reconstructed spectrum to be $\sim$ 18 ± 0.1 fs. Uncertainty in the pulse duration and FTL represent the standard deviation of four measurements. As will be discussed in Chap. 9 a second stage could be utilized after spatial filtering to further decrease pulse duration towards the single cycle regime [24].

Since the UCI laser has a gaussian mode, it is expected that there will be some self-focusing in the beam. As shown in Fig. 4.1, a focal spot is created with an achromatic doublet and imaged onto the surface of the CMOS camera with 40x PLAN achromat microscope objective and a duplicate achromatic doublet. Fig. 4.4 (a) shows the initial focal spot, and Fig. 4.4 (b) shows the same focal plane after the fused silica windows are introduced to the beam. The peak pixel count is seen to drop to $\sim$ 60% of its initial value, and the focal spot seems to degrade. However, after translating the 40x PLAN achromat on axis, a new focal plane was found to recover to $\sim$ 83% of the initial peak intensity. Therefore it seems that in the case of slight gaussian self-focusing, the use of wavefront correcting optics may be able to re-collimate much of the beam's energy before sending it into an OAP.

This section clearly demonstrates a power amplification of the central part of the beam where the intensity is highest and roughly constant. The pulse duration is nearly halved (from 39 fs to 20 fs), and the energy throughput of the fused silica windows was $\sim$ 99%. It is noted here that the wings of the spatial mode are likely not as compressed in time since the intensity is lower there and therefore less frequencies are generated through SPM. It is also shown that in the focal spot of the achromatic doublets, $\sim$ 83% of the initial maximum pixel counts were recovered when translating to the new focal plane accounting

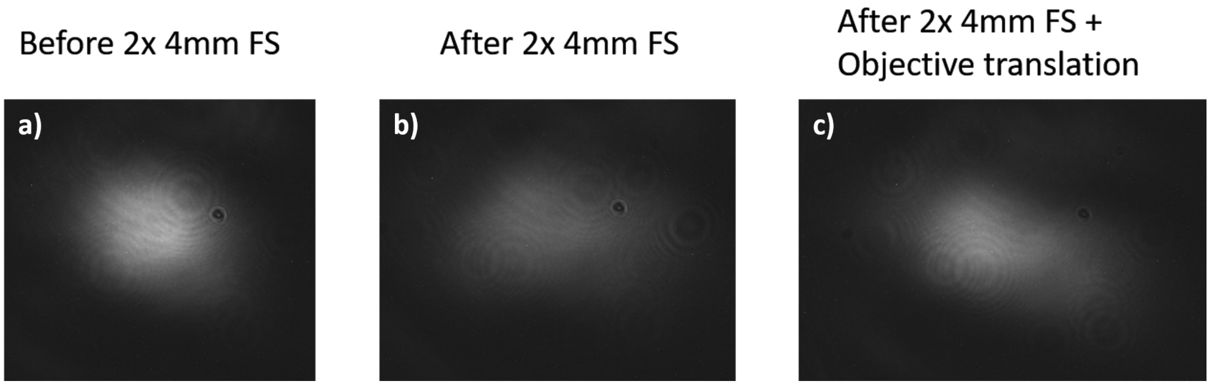

Figure 4.4: The focal spot of the laser pulses (a) created by an achromatic fused silica lens imaged by PLAN achromat microscope objective. The same plane is imaged after introducing 2x 4 mm compensating plates at Brewster's angle as the nonlinear medium (b). The new focus of the gaussian beam is found by translating the microscope objective on-axis (c)

for the whole beam self-focusing effects. This suggests that a deformable mirror may be useful in correcting for these wavefront errors and utilizing this pulse compression technique for Gaussian beams.

4.3 Far-field effects of SPM in thin wafers

To reach the highest intensities for experiments high intensity laser pulses are focused to focal spots with diameters on the order of the wavelength. It is therefore imperative that the wavefront quality be maintained in the pulse compression technique used. The unguided propagation of high intensity laser pulses in nonlinear materials can lead to wavefront imperfections [36, 82] that may impair the ability to focus them. Recall that in lower intensity pulse compression techniques it is common to use wave-guiding structures to maintain wavefront quality.

As shown in the previous section, large scale intensity gradients in the beam (ie. as are present in a Gaussian spatial mode) can lead to whole-beam self-focusing as evidenced by

Table 4.1: Approximate laser pulse parameters at each facility.

Laser Parameters				
Facilities	**pulse length [fs]**	**$1/e^2$ diam. [mm]**	**mode**	**I_0 [TW/cm^2]**
UCI	35	2.3	gaussian	1.3
HERCULES	30 [29]	100 [29]	flat-top	0.75-1

the on-axis translated focal spot. This section presents a comparative study of the change in the original focal plane of high intensity beams with both a Gaussian and flat-top mode.

Specifically, the far field effects of spectrally broadened high intensity pulses ($\sim 1\text{TW/cm}^2$) after propagation in thin fused silica wafers for application in pulse compression are investigated. The initial TFC proposal suggested the use of plastic films but here we test fused silica wafers as the nonlinear medium for the SPM due to their high damage threshold and high optical quality despite their lower Kerr response.

A focal spot created by an OAP is then imaged by a high numerical aperture microscope objective onto a CMOS or CCD camera to monitor changes. The imaged f/22 and f/20 focal spots at UCI and HERCULES are made by gold OAPs. In each experiment, the spectrum of the intense laser pulses is measured directly by a spectrometer with and without spectral broadening through SPM in one or two 0.5 mm fused silica wafers.

The amount of spectral broadening is controlled by varying the compressor grating separation with the fused silica wafers in the beam to find the broadest bimodal spectrum arising from the steepest rising and falling edges (shortest pulse) characteristic of SPM [38]. Experimental constraints at UCI and HERCULES required that the fused silica target could be removed *in situ*, so the grating separation was decreased (adding positive chirp to the pulse) to minimize spectral broadening in order to determine the unbroadened laser spectrum. Negatively chirped pulses are not included here due the observed effect of spectral narrowing through SPM in fused silica [88].

4.3.1 Gaussian mode (UCI)

The experimental layout of the UCI experiment can be seen in Fig. 4.5. Leak-through from an ultrafast 85%/15% beam-splitter with a transmitted pulse energy of 0.945 mJ and pulse duration of 35 fs was down-collimated by a factor of 5x from a $1/e^2$ diameter of 11.7 to $\sim$ 2.3 mm and an approximate peak intensity of $\sim$ 1.3 TW/cm^2. The small amount of dispersion introduced in transmission through the ultrafast beam splitter was compensated with the compressor gratings such that the shortest pulse could be achieved. The 5x telescope consisted of a -1000mm radius of curvature silver (Ag) mirror and a positive +200mm radius of curvature dielectric mirror to handle the high intensities.

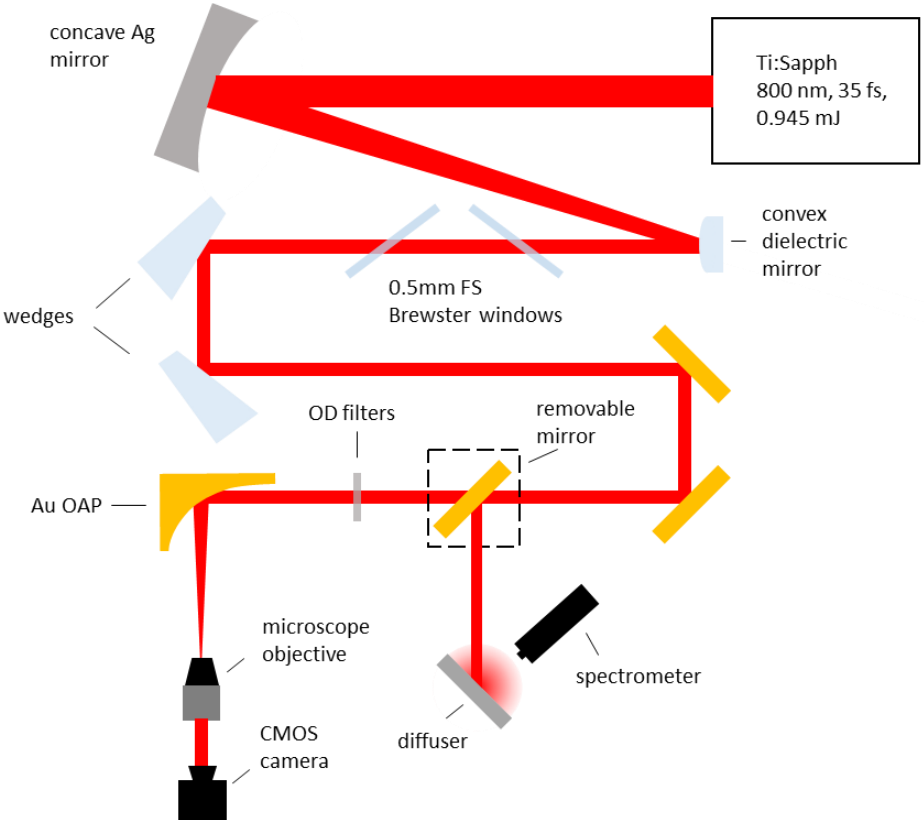

Figure 4.5: The experimental setup characterizing the changes in the focal plane and spectrum of gaussian laser pulses in 2x 0.5 mm fused silica wafers at Brewster's angle. Pulses are down-collimated in a 5x Galilean telescope to reach high intensities for SPM and then re-directed to pulse diagnostics after cutting power.

After down-collimation in the reflective Galilean telescope, the beam passes through two 0.5 mm fused silica windows at Brewster's angle at atmosphere. Immediately after the nonlinear interaction, the P-polarized beam is reflected from fused silica wedges at ~ 45 degrees to cut power to the diagnostics and prevent further nonlinearity in air. The beam is then redirected with gold mirrors to a spectrometer and focal spot camera to monitor the changes in focal spot.

Prior to taking focal spot measurements, the spectrum of the laser pulses was measured after propagation through the fused silica wafers at Brewster's angle. Since the spectral broadening through SPM depends on both the input beam chirp and duration, a compressor sweep was first performed to identify the location of shortest FTL (most broadening). Figure 4.6 shows the FTL of the broadened laser pulses versus actuator position. Recall that as measured in Chap. 3 the shortest pulse occurs near the actuator position 5295. Since we expect that the shortest pulse will also induce the strongest spectral broadening since it has the highest intensity, it makes sense the the shortest FTL (most broadening) would occur very close to the actuator position corresponding to the shortest pulse. Also, as determined in Chap. 3 actuator positions below 5295 correspond to positive chirp, and higher actuator positions correspond to negative chirp.

The FTL of the laser pulse without any nonlinear interaction is ~ 29 fs, which was measured by removing the nonlinear samples from the beam path and recording its spectrum. This value matches the value measured at low actuator positions (very positive chirp) very well. Another interesting thing to note is that at slightly negatively chirped input pulses that are still intense enough to induce a nonlinear interaction with the glass, the FTL actually decreases. This is the expected behavior of spectral narrowing as investigated by [88]. Although very interesting, in the next section we omit the negatively chirped pulses, and compare focal spots at compressor position 5075

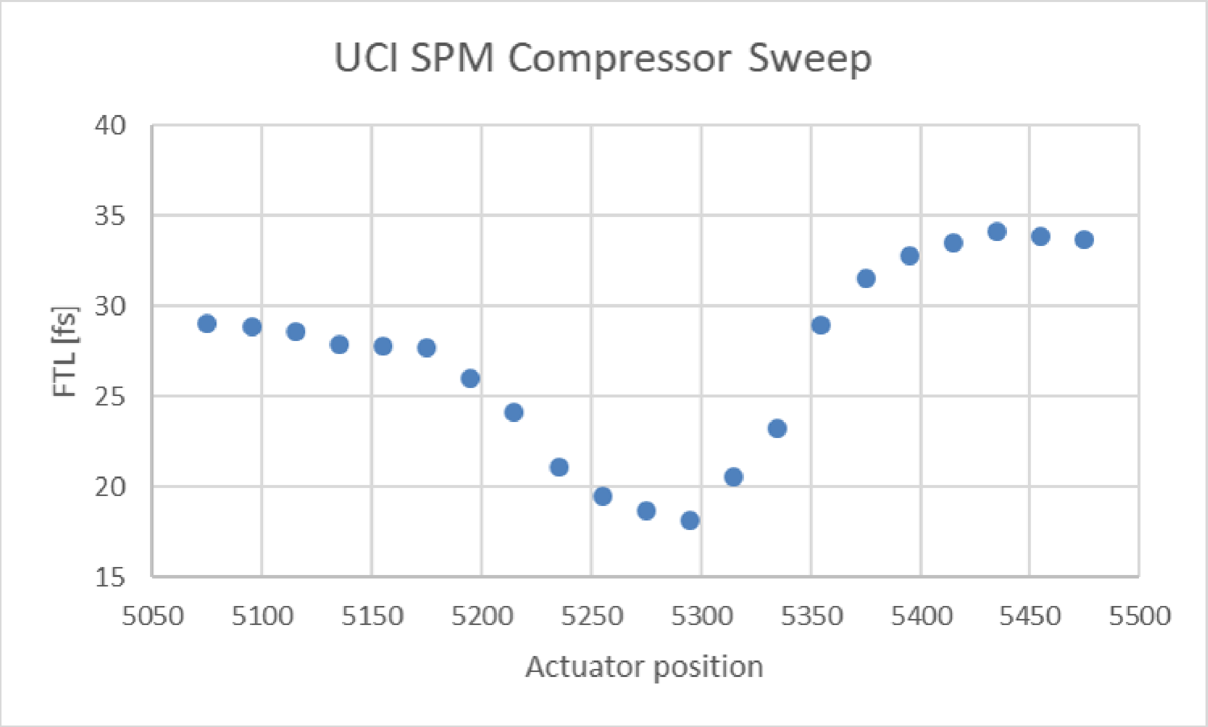

Figure 4.6: The fourier transform limit of the broadened spectrum through SPM in two 0.5 mm fused silica wafers oriented at Brewster's angle. By altering the actuator position of the compressor, the location of the unbroadened pulse (very positively chirped) and the maximally broadened (shortest FTL) are identified

and compressor position 5295 corresponding to cases with no nonlinear broadening and maximum nonlinear broadening (corresponding to the shortest FTL).

At UCI the shape of the intensity distribution is seen to change significantly with respect to the original focal plane, as expected due to whole-beam self-focusing. Each focal spot measurement at UCI represents the average of 472 shots. The average fwhm along x of five such measurements with and without spectral broadening increases from 218±5 to 268±13 pixels, and the energy contained within a circle of diameter equal to the fwhm along x, centered at the peak signal decreases from 35% ± 1% to 24% ± 1% where uncertainty represents the standard deviation of these measurements. This general spreading out and decrease in contained energy can be seen in the line-out comparison in Fig. 4.7 (a). It is also noted here that an analytical 2d gaussian profile was put through this same

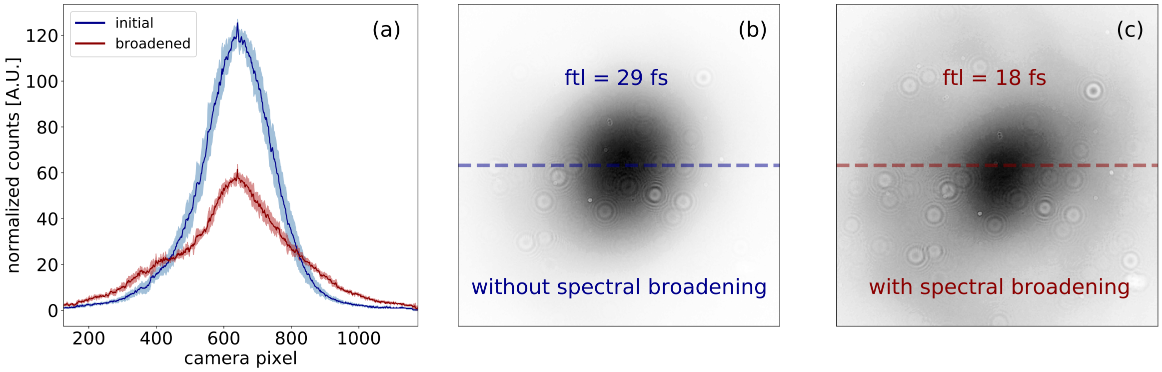

Figure 4.7: The line-out of the intensity profile of the focal plane (a) at compressor position 5075-unbroadened (blue) and 5295-broadened (red) respectively. Figure (b) and (c) show an example focal spot and the associated line-out location together with the amount of spectral broadening as indicated by the FTL of the spectrum. Shading in (a) represents the standard deviation of multiple measurements

analysis and was determined to have $\sim 50\%$ of the counts contained within the fwhm. This expected behavior serves as a benchmark to ensure that the code is performing as intended.

The full 2d distribution of intensity in the original focal plane of gaussian laser pulses experiencing no nonlinear spectral broadening (b) and maximum spectral broadening (c) are also shown in Fig. 4.7. This is the result of strong self-focusing resulting in an on-axis translation of the focal spot as shown in the previous section. Here the small beam diameter of 2.3 mm and high power of 0.027 TW ($\sim 10^4 P_{cr}$) contribute to strong spatial gradients across the beam profile leading to strong Kerr self-focusing.

The UCI focal spots were measured with gain on the camera set to the default value of “1.” Each image was subject to the same image preparation for analysis. The outlier removal routine in ImageJ was used with a radius of 3 and threshold of 10, and the De-speckle routine was used afterwards.The Rolling background removal tool worked very poorly and slowly due the very large focal spot with respect to the camera size. Since the background was very uniform at the cameras edges, a background subtraction based on the intensity threshold was used instead through the contrast menu. After this procedure, each shot was then scaled to have the same number of total integrated counts.

4.3.2 Flat-top mode (HERCULES)

The experimental layout of the HERCULES experiment can be seen in Fig. 4.8. As opposed to having a gaussian beam as in the UCI laser, HERCULES has a flat-top mode. The energy of the laser pulses at HERCULES was significantly higher at $\sim 1.8 - 2.4$ J, but since the beam size also must scale up to prevent damaging optics, the intensity is comparable ~ 1 TW/cm^2. Nominally, the HERCULES beam has a beam diameter of 100 mm and a pulse duration of 30 fs. Using these parameters to predict the expected intensity, the intensity is calculated to be $\sim 0.75 - 1$ TW/cm^2 corresponding to a pulse power of $\sim 60 - 80$ TW. However, at the time of the experiment the shortest FTL was found to be 48 fs, leading to a calculated intensity of $\sim$ 0.47-0.63 TW/cm^2 corresponding to pulses having $\sim 40 - 50$ TW of power assuming a 100 mm beam diameter.

A single fused silica wafer with a larger diameter (150 mm) but the same thickness (0.5 mm) (University wafer Part#: U01-W1-140620-1. JGS2) is utilized at near-normal incidence for spectral broadening as seen in Fig. 4.8. Since the input beam to the optical setup was known to have some high frequency modulations, the B-integral before the OAP was minimized to prevent the likelihood of damaging the OAP. This concern would be less of a problem if the input beam had very little noise, or was spatially filtered before the interaction. Since these preparatory measures were not able to be implemented in time, the effect of a single wafer was measured in this experiment.

After nonlinear interaction in the fused silica wafer the beam is redirected by high reflectivity dielectric mirrors under vacuum to a f/20 OAP. After going through focus, the

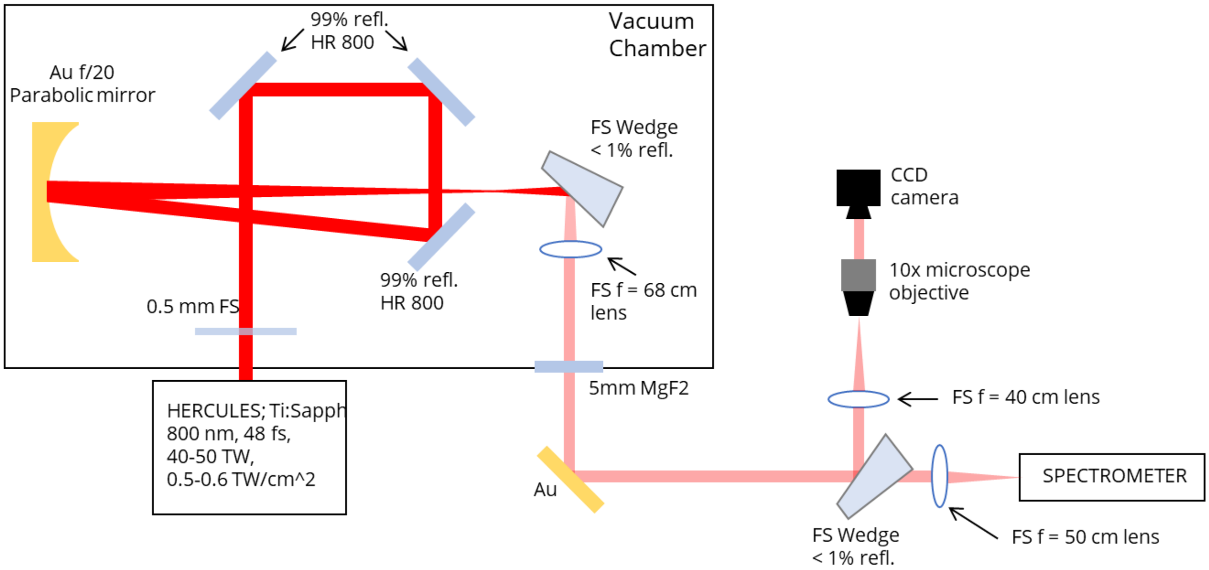

Figure 4.8: The experimental setup at HERCULES characterizing the changes in the focal plane and spectrum of flat-top laser pulses in 1x 0.5 mm fused silica wafer. Pulses wedged and re-collimated so as to exit the chamber without clipping and then re-directed to pulse diagnostics after cutting power.

beam is re-collimated to a smaller diameter (so as to make it out of the vacuum chamber window without clipping) by a fused silica lens after being reflected at near Brewster's angle to cut the power to below 1% of the initial power. The beam then exits the chamber through 5mm of MgF2 and is wedged further before the image of the focal spot is imaged by the microscope objective onto a CCD camera. The spectrum of the beam transmitted through the wedge is also recorded by the spectrometer. Due to the nature of this setup, the spectrum and focal spot for each shot was recorded simultaneously.

As with the UCI experiment, a compressor sweep was performed to find the location of the largest spectral broadening by varying the grating separation. A similar shape was found in the HERCULES compressor sweep as the UCI compressor sweep as shown in Fig. 4.9. Analogously to the UCI data, at low grating separation values, the laser pulses are found to have positive chirp. This is evident from the monotonically decreasing FTL to a minima at the location of lowest FTL (broadest spectrum). Whereas as the grating separation increases beyond this minima, the FTL is seen to increase due to spectral narrowing of negatively chirped pulses.

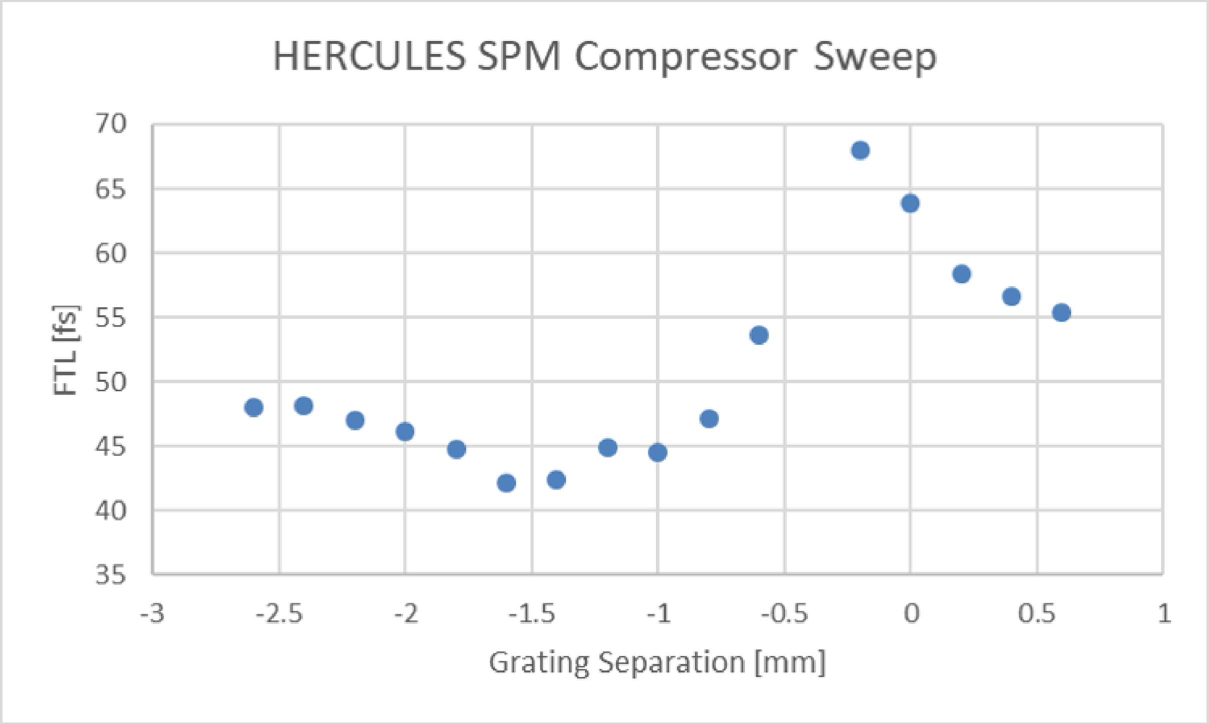

Figure 4.9: The fourier transform limit of the modulated spectrum from SPM in 1x0.5 mm fused silica wafer at near normal incidence. Again here the location of most significant spectral broadening (shortest FTL) and the regions of positive and negative chirp are identified.

As in this case with the UCI data, the negatively chirped pulses are ignored in this analysis, and the data collected at grating separation of -1.4 mm and -2.6 mm was analyzed in depth. Similar to the previous section Fig. 4.10 (a) shows the line-out of the intensity profile of the unbroadened (blue) and broadened (red) shots at these grating separation locations. As will be discussed in more detail in the next section, high power laser facilities like HERCULES tend to be susceptible to filamentation due to small scale intensity fluctuations in their beam profiles as opposed to whole-beam self-focusing as in the case of small Gaussian profile beams. This is because the spatial intensity gradients determine the magnitude of the self-focusing effects.

As seen in Fig. 4.10 the shape of the intensity distribution changes much less significantly than in the case of the UCI experiment. The line-out of the intensity profile after spectral broadening Fig. 4.10 (a-red) is nearly identical to the line-out of the profile without nonlinear broadening Fig. 4.10 (a-blue). Here the line-out values correspond to the average line-out at compressor positions -1.4 mm (red) and -2.6 mm (blue) of 4 and 3 shots respectively where the shading represents the standard deviation among these shots. 4.10 (b) and (c) show example shots at these compressor locations along with the corresponding FTL calculated from the spectral broadening seen to decrease from ~ 48 fs to ~ 42 fs.

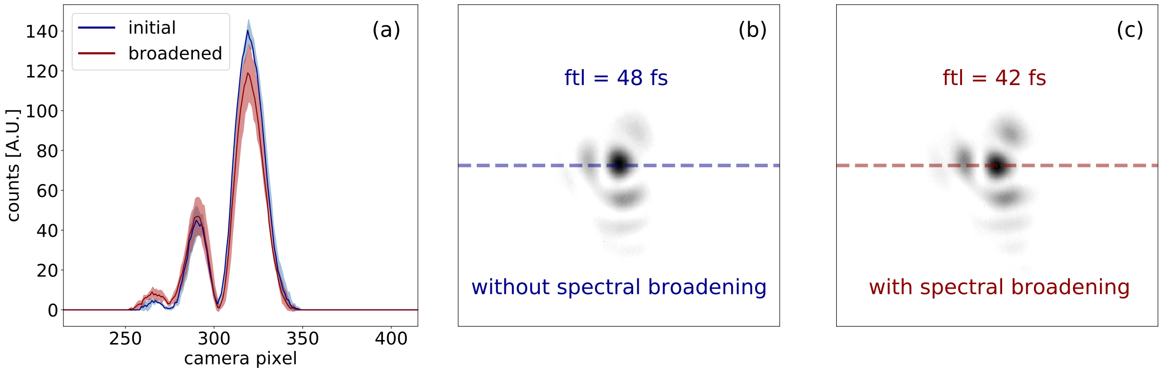

Figure 4.10: The line-out of the intensity profile of the focal plane (a) at compressor separation -2.6 mm-unbroadened (blue) and -1.4 mm-broadened (red) respectively. Figure (b) and (c) show an example focal spot and the associated line-out location together with the amount of spectral broadening as indicated by the FTL of the spectrum. Shading in (a) represents the standard deviation of multiple shots

In addition to the line-out comparison, a crude comparison of the energy contained in each successive diffraction ring was measured from the data taken at these compressor positions as well. As seen on Fig. 4.11 (a), regions were defined that roughly correspond to each diffraction ring. If the pixel falls within a circle centered at the max pixel value with a radius of 20 pixels it is considered to fall within the central spot (blue-dotted). If a pixel falls between a radius of 20 pixels and 45 pixels (between the blue and red-dotted lines), it is considered to fall in the first ring. The second ring contains pixels that fall between a radius of 45 and 70 pixels (between red and green-dotted lines). Finally, the rest of the pixels are considered to exist "everywhere else."

The counts that exist in each of these regions are summed, and the sum for each region is averaged over the number of shots at each compressor position. The blue bars in Fig. 4.11 (b) show the average percent of total energy per shot in each region without nonlinear broadening, where the error bars represent the standard deviation among shots (-2.6 mm grating separation). Similarly the red bars in Fig. 4.11 (b) show the average percent of total energy per shot in each region with maximized nonlinear broadening, where the error bars represent the standard deviation among shots (-1.4 mm grating separation)

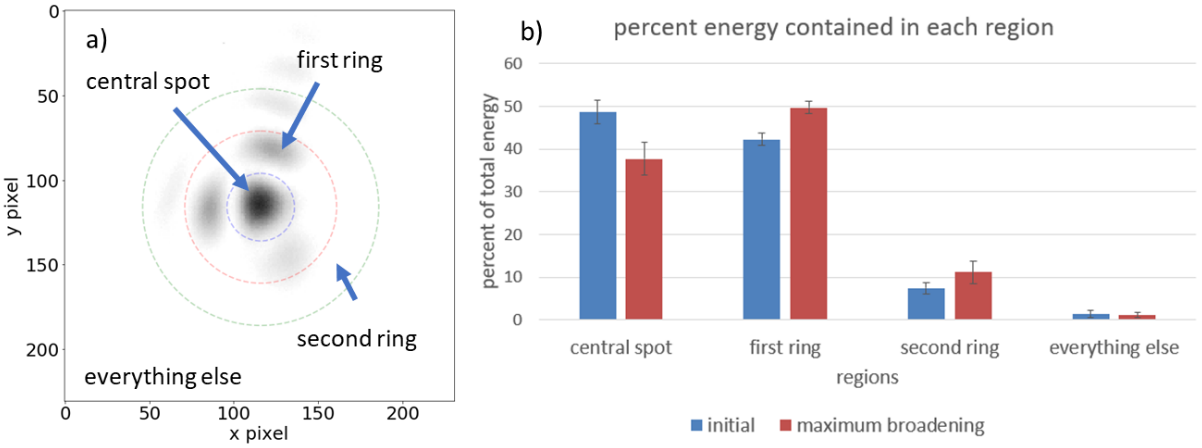

Figure 4.11: The regions roughly constituting the central spot and each subsequent diffraction ring (a) and the relative distribution of energy (b) in the unbroadened (blue) and broadened (red) shots. Error bars in (b) represent the standard deviation in the percent of energy found in each region for each set of shots.

As shown in Fig. 4.11 the energy contained in the central spot is seen to change from 49% ± 3% to 38% ± 4%. The change in counts without a significant change in shape may be due to filamentation, which is an expected challenge in high energy systems that will be explored in more detail in the following section.

It is noted here that although some counts are lost in the central spot, the pulse can still be focused to high quality. This critical result suggests that with the help of chirped mirrors to compress the pulse to the ftl, this technique could be employed to compress high energy laser pulses toward the single cycle regime while maintaining focal quality. It is further noted here that with the help of spatial filters before the nonlinear interaction, even fewer counts would likely be lost than measured in this experiment after SPM. Further investigation is needed to explore the maximum thickness of of material (amount of nonlinear phase shift) permissible before the onset of catastrophic collapse and filamentation.

Each of the HERCULES focal spots were subject to the same image preparation for analysis. The out-lier removal routine in ImageJ was used with a radius of 2 and threshold of 15. The rolling background removal tool was used with a rolling ball radius of 200. A background subtraction based on the intensity threshold was used to remove signal that was below 5 counts through the contrast menu. After this procedure, each shot was then scaled to have the same number of total integrated counts.

4.3.3 Discussion

High power laser pulses such as those of HERCULES typically have flat-top modes due to amplification in multi-pass amplifiers. In a multi-pass amplifier, gain saturation is bypassed by taking different geometrical paths through the gain medium. This allows the extraction of as much energy from the gain medium as possible [89]. On the other hand in single stage regenerative amplifiers like that of UCI laser pulses are amplified in an optical cavity and as a result have a near gaussian spatial mode.

When the peak power of the pulse exceeds the critical power $P_{cr} = \pi(0.61)^2\lambda_0^2/(8n_0n_2)$ [90] ($\sim$ 2.6 MW for fused silica at 800 nm), the laser mode and diameter play an important role in how the focusability is affected through the nonlinear Kerr effect. The critical power is the threshold at which whole-beam self-focusing of a Gaussian beam due to the Kerr effect just compensates the beam spreading due to diffraction [79]. If the material is thin enough so that the beam profile does not change significantly, the focal length of the nonlinear lens can be approximated by $f = \mathrm{w}_0^2/(4n_2I_0l)$ [79] where w_0 is the beam radius, I_0 is the peak intensity and l is the material thickness. On the other hand the collapse dynamics of intense laser pulses with super-gaussian modes are slightly different and tend to be initiated by noise in the beam profile [91]. These pulses tend to be susceptible to multi-filamentation through the modulational instability [82] where a beam with $P \gg P_{cr}$ is understood to break up into multiple filaments during propagation through a nonlinear medium of sufficient length, each with power of order $\sim P_{cr}$ [92].

In the context of spectral broadening for pulse compression, mode effects such as those seen in the UCI data are conventionally avoided by inducing SPM in gas-filled hollow-core capillaries which only allow for the propagation of the fundamental mode at sufficient length [44]. Unfortunately the energy of intense laser pulses spectrally broadened in this guided process are limited to the order of $\sim$ 1 mJ (with recent techniques using density ramps reaching as high as $\sim$ 5 mJ [46]) where self-focusing and ionization of the gas near the entrance of the fiber degrades the coupling to the fiber and therefore broadening due to SPM. Alternatively, by inducing SPM in a thin media, a gaussian beam can be progressively spectrally broadened and self-focused by a sequence of thin plates by a process called multiple plate continuum generation [93].

To go beyond the limits of conventional techniques by taking advantage of the flat-top mode at high energy facilties, intense laser pulses can induce spectral broadening in a very thin material. Spatially filtering the beam and using a thin nonlinear material for

SPM of flat-top laser pulses allows for the minimization of filamentation, and removal of noise before the modulational instability is allowed to grow [92, 94]. Combining the SPM of cleaned flat-top beams in thin films with GDD compensation from chirped mirrors constitutes the thin film compression technique (TFC), which has potential to extend pulse compression techniques to the petawatt level.

The previous section has demonstrated that SPM can be induced while maintaining the focal spot structure in high power flat-top beams, even without spatially filtering the beam before the nonlinear interaction. Even though some counts are lost in the central spot, this suggests that this technique could be utilized to compress laser pulses toward the single cycle regime while maintaining the focusability. The next section demonstrates TFC on a high energy (~ 300 mJ) flat-top system in plastic and fused silica.

4.4 Thin film compression (LASERIX)

In the previous section it was shown that the redistribution of intensity in the focal plane arising from high intensity (~ 1 TW/cm^2) SPM in thin fused silica wafers (0.5 mm) is mitigated when using flat top laser pulses. This is the motivation behind the technique called thin film compression. Thin film compression (TFC) [24] suggests the use of very thin material and high intensity flat-top laser pulses to generate compressible bandwidth through SPM while side-stepping the complications caused by strong spatial intensity gradients explored in the previous section. Ideally one would use a thin optical quality material with as high n_2 as possible (ie. plastic) combined with a flat top laser pulse to acquire quadratically chirped bandwidth to re-compress using chirped mirrors.

This section describes TFC experiments carried out at the LASERIX facility. Laser pulses with parameters described in Table 4.2 were spectrally broadened in thin films/wafers and re-compressed using the same model chirped mirrors as in the UCI pulse compression experiment (HD58 Ultrafast innovations). 0.5 mm of fused silica and 0.4 mm of Zeonor (cyclo-olefin polymer) were used as the SPM target. Pulse compression was carried out at a range of energies (35 - 300 mJ) corresponding to the intensity range in Table 4.2 achieving pulse compression to progressively shorter durations. Phase compensation was achieved through a combination of chirped mirrors and dispersion through fused silica and MgF2 windows before the temporal diagnostics to demonstrate re-compression.

4.4.1 Fused silica wafer

Similar to the previous section, 0.5 mm of fused silica is used as the SPM target in the first experiment. Though its n_2 is lower than some materials, its optical quality and high damage threshold make it an ideal first candidate to compare the performance of other materials in this energy scaling. The fused silica wafer was the same model as used in the previous section at UCI and HERCULES. The experimental setup and pulse diagnostics were arranged according to Fig. 4.12. Laser pulses entered the vacuum chamber directly from the compressor immediately encountering the 0.5mm of fused silica at full power at near normal incidence. The S-polarized beam was then reflected at $\sim$ 45 degrees by two glass windows with a frosted back (similar to the functioning of a wedge) to cut power by 10% each to minimize the nonlinearity in the vacuum chamber window. The laser pulses were then re-directed out of the vacuum chamber by a di-electric mirror through an MgF2 window and transported to the phase compensating optics and temporal and spectral

Table 4.2: Approximate laser pulse parameters.

Laser Parameters				
Facilities	**pulse length [fs]**	**1/e^2 diam. [mm]**	**mode**	I_0 **[TW/cm^2]**
LASERIX	50	18.75	flat-top	0.25-2.25

diagnostics. The laser pulses were measured on a shot to shot basis with Self-referenced spectral interferometry (SRSI) which provided a spectrum and phase measurement and pulse duration reconstruction. An auto-correlator was also used as a secondary pulse duration measurement. The leak-through of the primary 800nm spectrum was also measured after the auto-correlator as a secondary spectral measurement. These secondary measurements were taken at each experimental condition but were not correlated to shot-to-shot measurements of the Wizzler.

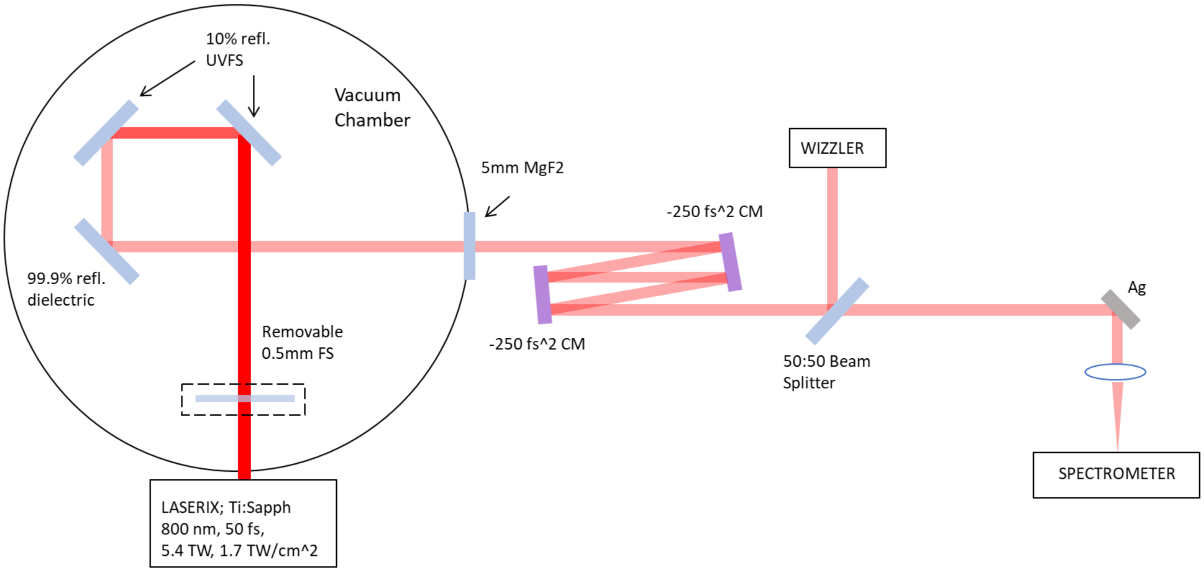

Figure 4.12: A schematic of the thin film compression experiment using 0.5mm fused silica wafers. Laser pulses are spectrally broadened in fused silica and transported out of the chamber after power is dumped through fresnel reflections on glass. Pulse is then re-compressed and measured by Self-referenced spectral interferometry (Wizzler), autocorrelator, and spectrometer.

At ~ 1 TW/cm^2 the compressor grating was adjusted such that the broadest spectrum could be achieved. Once the compressor was optimized, the phase was compensated and the broadened spectrum and compressed pulse duration were measured by the diagnostics. Laser pulses with intensities in the range 1 - 2.25 TW/cm^2 were spectrally broadened and compressed using thin film compression (due to the lower n_2 of fused silica lower intensities were not investigated). Figure 4.13 shows the measured pulse duration by SRSI (purple) where error bars represent the standard deviation of 5 shots and the Fourier transform limit as calculated from the spectrometer (grey) as a function of increasing intensity.

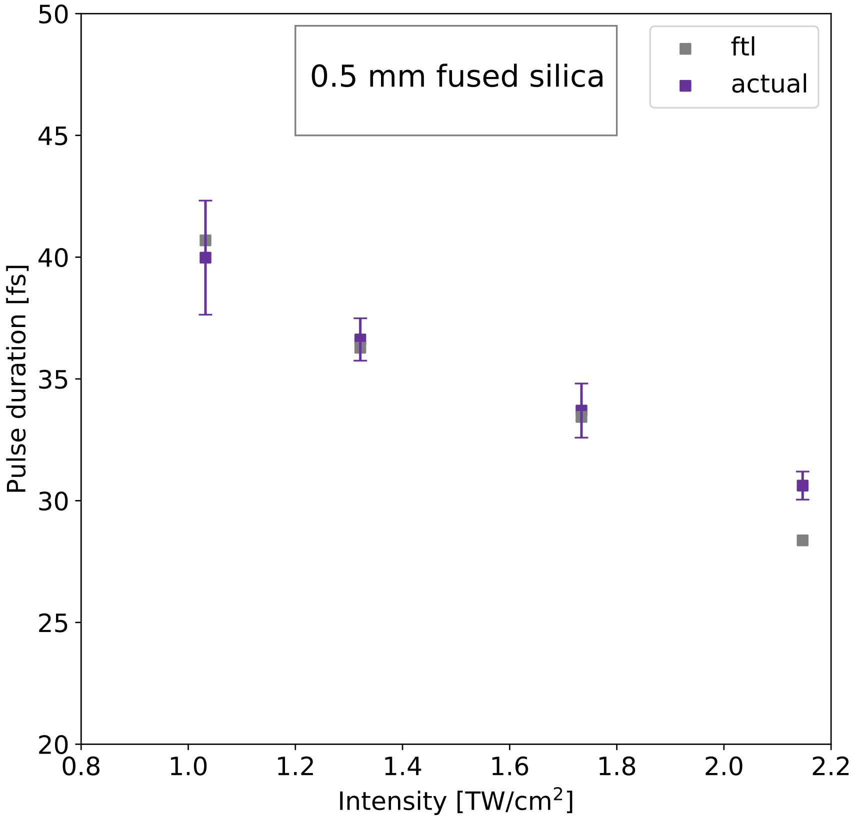

Figure 4.13: Compressed laser pulse duration as measured by SRSI (purple) and analytical Fourier transform limit calculated from measured spectrum (grey) as a function of increasing intensity. Error bars represent standard deviation of 5 measurements.

Shots with higher intensity produced more spectral broadening as expected, as shown by the decreasing spectral ftl in Fig. 4.13 - grey. In addition to the increasing spectral bandwidth, the pulses were also compressed close to the ftl by compensating the phase of the generated bandwidth as measured by SRSI. The most significant pulse compression in this range resulted in a pulse compression from $\sim$ 54.8 fs to $\sim$ 30.6 fs as shown in Fig. 4.14 (b). This compressed pulse duration is very close to the calculated ftl from the broadened spectrum shown in Fig. 4.14 (a), as measured by the spectrometer of ∼ 28.3 fs.

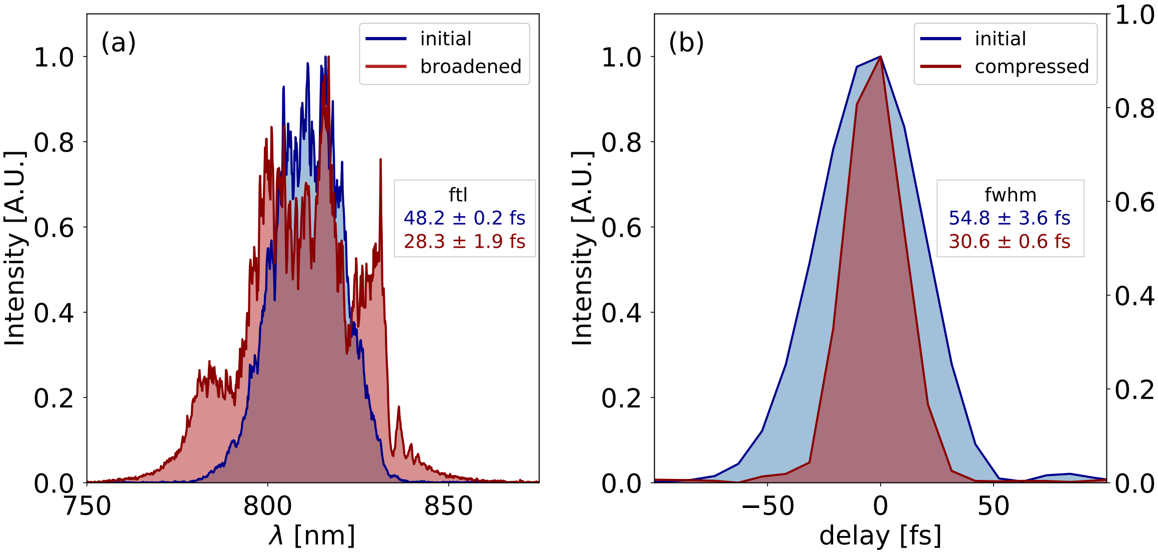

Figure 4.14: Spectral broadening (a) of 2.1 TW/cm^2 laser pulses in 0.5 mm of fused silica and pulse compression (b) with chirped mirrors. The spectrum and pulse duration of the initial pulse (blue) and the laser pulse after thin film compression (red) can be seen in each figure.

4.4.2 Thin films

As was mentioned in the previous section, in the initial TFC proposal thin films (ie. sub-millimeter plastics) were suggested as the nonlinear medium due to their higher n_2. Though these thinner materials may be more susceptible to damage, they could be easily replaced if they were to accumulate damage after several shots. In this spirit, a plastic called Zeonor (cyclic olefin polymer - COP) was used as the thin film in this experiment. A large roll of ∼ 0.1 mm thick Zeonor was installed on an electronically controlled roller mechanism constructed by a colleague shown in Fig. 4.15. The roller assembly consisted of two large spools that would rotate and cycle through the thin film material as it began to accumulate damage, exposing fresh target when necessary. The film is wound around

5 posts that are situated such that the angle made with an incoming laser pulse and each successive film is Brewster's angle to maximize transmission.

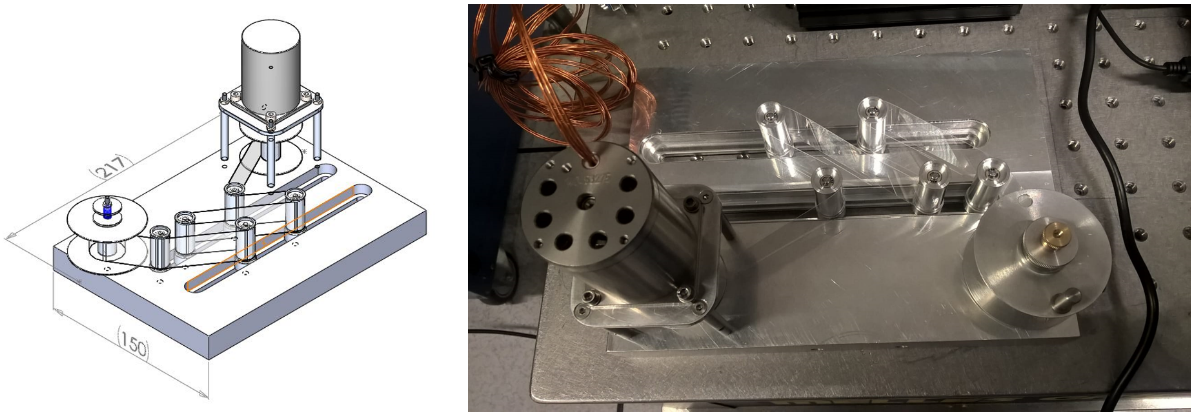

Figure 4.15: A schematic diagram (left) and the actual assembled roller mechanism with Zeonor roll installed (right). Laser pulses passing through the mechanism are exposed to 4x 0.1 mm Zeonor films.

Laser pulses passing through the assembly encounter the film four times accounting for a total transmitted path length of approximately 0.4 mm. The roller mechanism was oriented vertically as shown in Fig. 4.16 such that the S-polarized laser pulses encounter the films at Brewster's angle. The roller mechanism was installed in place of the 0.5 mm fused silica target shown in Fig. 4.12, but the setup was otherwise identical.

Due to the larger expected n_2 the intensity scaling started much lower than with the fused silica ranging from $\sim 0.25 - 2.2$ TW/cm^2. The same compressor position as was used for the 0.5 mm fused silica was used in this experiment (and was verified to be the optimized for broadest spectrum). Again here as the laser shot intensity is increased, the spectral broadening is increased as expected resulting in a shorter Fourier transform limit as shown in Fig 4.17 (grey). Here again the Fourier transform limit is calculated analytically from the spectrum measured by the spectrometer. Similarly, as in the previous section, Fig. 4.17 is the pulse duration measured by SRSI (purple) where the error bars represent the standard deviation of 5 shot measurements.

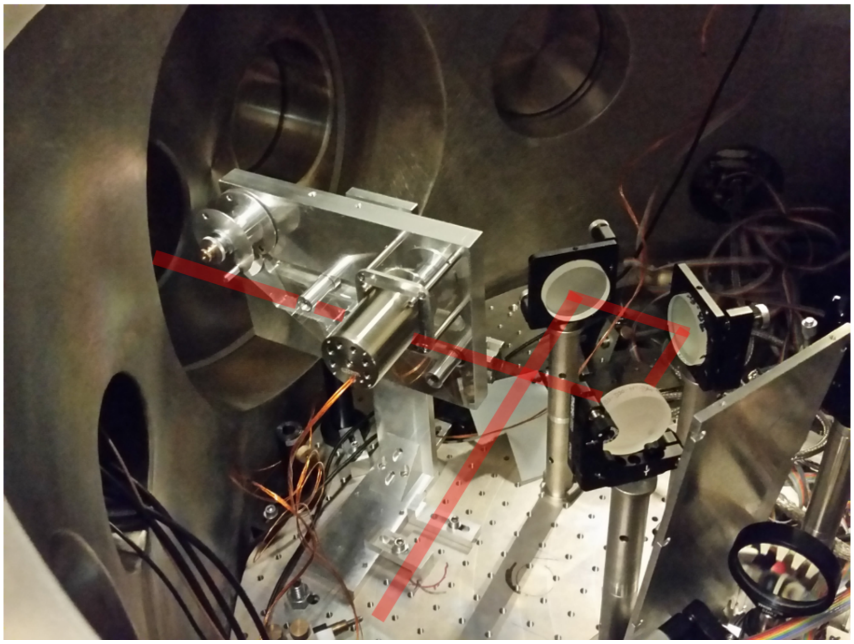

Figure 4.16: Vertically installed roller assembly with Zeonor film installed. The laser pulses (red) pass through 4x 0.1 mm films in the assembly and follow the same optical path as in the previous section.

As seen in Fig. 4.17, the Fourier transform limit is seen to decrease to ~ 22.1 fs at near 2.25 TW/cm^2. In comparison with the fused silica, there is slightly less material (0.4 vs 0.5 mm) and a lower ($\sim$ 6 fs) Fourier transform limit achieved. This more significant spectral broadening at roughly the same intensity and in less material verifies that the n_2 is larger in this material than in fused silica. Furthermore at the highest intensities, compression of this bandwidth to very near the Fourier transform limit was measured by SRSI. The most significant spectral broadening and thin film compression from this experiment is shown in Fig. 4.18 where laser pulses are compressed from 54.8 fs $\pm$ 3.6 fs to 23.1 $\pm$ 0.3 fs where here again the uncertainty represents the standard deviation in 5 shots.

It is also noted here that there was also a camera (not shown in the schematic) to measure how the far field of the laser pulse changed before and after spectral broadening. The focal spot in this experiment however, was created by a fused silica lens and therefore subject

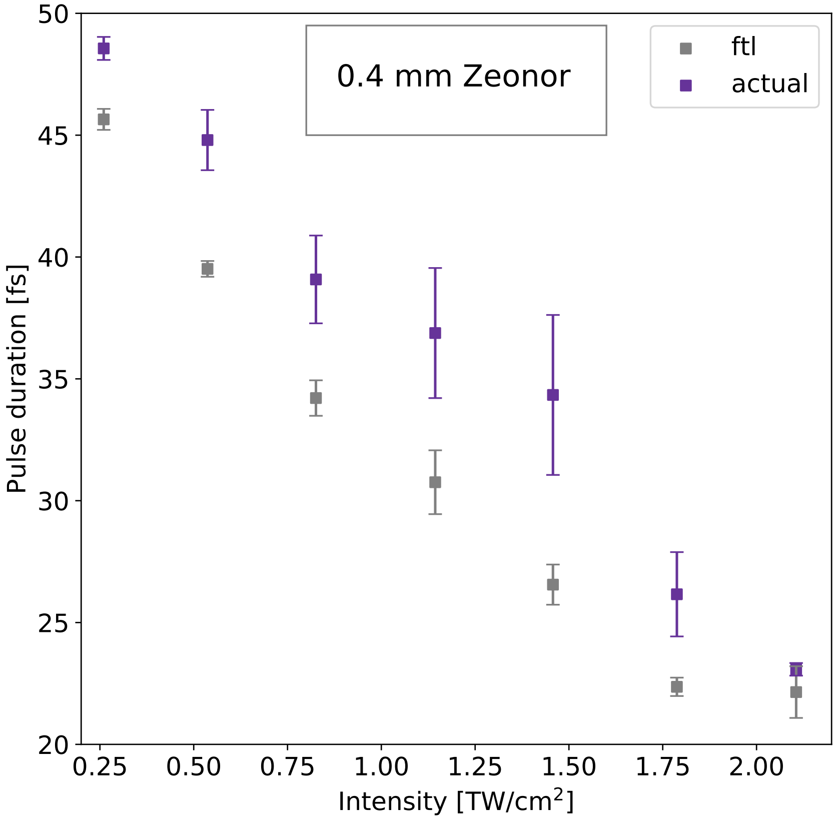

Figure 4.17: Compressed laser pulse duration as measured by SRSI (purple) and analytical Fourier transform limit calculated from measured spectrum (grey) as a function of increasing intensity. Error bars represent standard deviation of 5 measurements.

to chromatic effects especially when the spectral bandwidth was broadened. Generally speaking, the far field of the pulses before and after spectral broadening in fused silica maintained their far field as in the previous experiment, whereas the far field before and after spectral broadening in the sequence of Zeonor films was much worse. The difference in far field quality is likely due to the optical quality of the material since the focal spot quality was bad before and after the nonlinear effect for the Zeonor. An additional factor could be that since the Zeonor was installed on a roller assembly it was subject to tensions associated with the roller mechanism. It is further noted here that local hot-spots in the

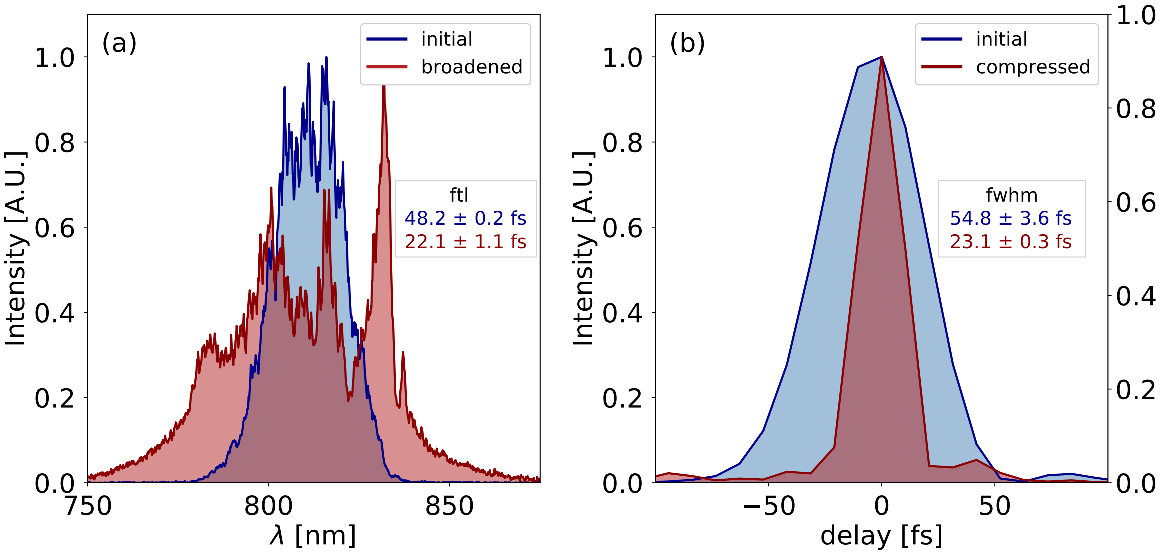

Figure 4.18: Spectral broadening (a) of 2.25 TW/cm^2 laser pulses in 0.4 mm of Zeonor and pulse compression (b) with chirped mirrors. The spectrum and pulse duration of the initial pulse (blue) and the laser pulse after thin film compression (red) can be seen in each figure.

beam profile during an initial spectral broadening investigation with 1x 0.1mm Zeonor film began to damage at $\sim 2 - 2.6$ TW/cm^2 with clear damage visible at 2.6 TW/cm^2 of 800 nm 50 fs laser pulses. This experiment has demonstrated thin film compression to less than half of the original pulse duration and shown that Zeonor is a viable candidate for use in thin film compression due to its strong nonlinear response. Should optical quality Zeonor become available, it will likely be very useful for thin film compression at 800 nm.

Chapter 5

λ-scaling of self-phase modulation

In this chapter we investigate the effect of using longer wavelength laser pulses to generate SPM, ultimately for use in pulse compression towards the single-cycle regime. There are several advantages of using longer wavelengths. First, given ultrashort laser pulses of ~ 35 fs (~ 45 fs at the time of this experiment) at longer wavelengths the laser pulses start off with fewer oscillations, giving a head-start to compression to the single cycle regime. Additionally, the laser vector potential is higher since $a_0 \propto \lambda_0$, where λ_0 is the carrier wavelength of the laser, making the laser pulses more suitable for many high field science applications (ie. ion acceleration) where higher a_0 is ideal. Furthermore, although it can be approximated as seen in Chap. 2, the $\chi^{(3)}$ is not well-known at these wavelengths in many materials.

5.1 Self-phase modulation near the zero dispersion point

The optical parametric amplifier (OPA) at UCI produces an “idler” and a“signal” beam which are generated from a combination of nonlinear conversion processes from the input beam. This process produces beams with photons of energies that sum to the same energy as photons of the input beam (ie. $hc/\lambda_{input} = hc/\lambda_{idler} + hc/\lambda_{signal}$). In this case the input wavelength is 800 nm and OPA peak efficiency occurs when $\lambda_{idler} \approx 2100$ nm and $\lambda_{signal} \approx 1300$ nm, but can be tuned to produce beams that have wavelengths in the range $\sim$ 1140 - 2680 nm.

The first long wavelength SPM experiment demonstrates self-phase modulation at 1260 nm. At approximately this wavelength, the index of refraction of fused silica versus wavelength undergoes an inflection point, which means that the second order phase accumulated by the beam passing through the glass is effectively zero where the second order phase is defined as [83]

$$\varphi_2 = \frac{\lambda^3}{4\pi c^2}\frac{d^2 n}{d\lambda^2}L \tag{5.1}$$

In other words, a laser pulse with this carrier frequency does not become linearly chirped in passage through fused silica. It should be emphasized that the pulse still accumulates phase in passage through fused silica at this wavelength - even though the second order phase coefficient is zero.

Though at the time of the experiment we did not have the ability to compress the broadened bandwidth, the goal was to induce spectral broadening at roughly the same ballpark of intensity as the previous pulse compression experiments, and then measure the resultant laser pulse in the SHG FROG and determine its Fourier transform limit. Though our spectrometer is only sensitive in the range $\sim 200-1100$ nm, the SHG FROG trace will consist of the second harmonic bandwidth which falls squarely in the middle of our detection range near ~ 630 nm.

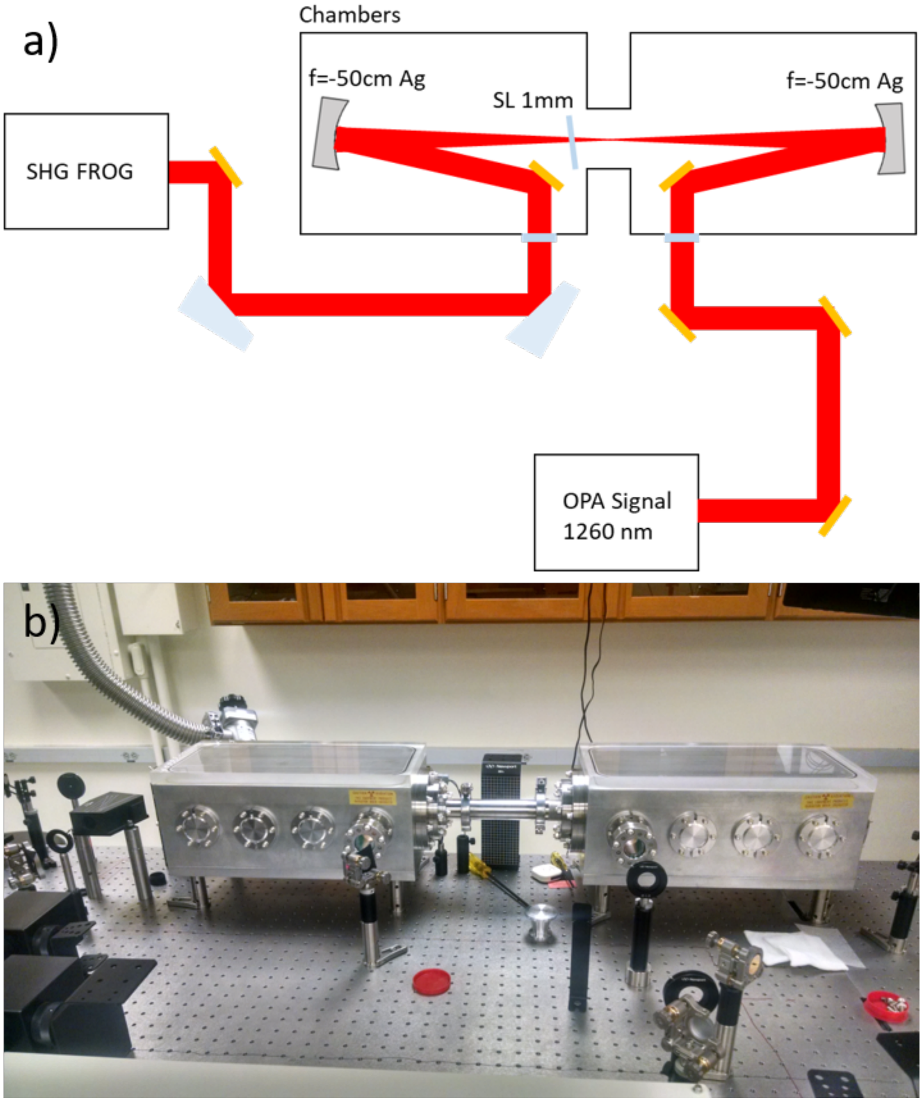

Figure 5.1: A schematic diagram of the long wavelength SPM experiment (a) and an image of the table setup (b). Laser pulses are sent through a Keplerian telescope in a set of vacuum chambers to increase the laser intensity at the location of the nonlinear sample. Spectral broadening and resultant pulse duration is then resolved in the SHG FROG.

The experimental setup is shown in Fig. 5.1. 0.983 mJ 1260 nm 45 fs ($\sim$ 22 GW) laser pulses are focused and re-collimated in a 1 to 1 Keplerian telescope. The Keplerian design under high vacuum ($\leq 10^{-4}$ Torr) allows higher intensities at the location of the nonlinear SPM target without compromising the beam quality by avoiding breakdown at the focus. The windows to the vacuum chamber are composed of C-coated fused silica, and the concave focusing optics constituting the telescope are protected silver. The SPM target (1mm soda lime glass) is then placed $\sim$ 268 mm from the surface of the second concave mirror ($\sim$ 232 mm from focus) after focus at near normal incidence. After exiting the telescope, two fused silica wedges were used at $\sim$ 45 degrees to cut power and transport the beam to the SHG FROG for measurement. Since at the time of this experiment the 1260 nm signal beam was S-polarized the beam sent to the frog was $\sim 22 \times (0.01) \approx 0.22$ GW. When using a focusing geometry to increase the intensity, care should be taken in choosing the target thickness and orientation for the SPM target. If the sample is oriented at Brewster's angle, one side of the mode will encounter the SPM target at a lower intensity than the other. Additionally, using a thin target will make approximations of the nonlinear effects easier to approximate since a thin target will occupy less longitudinal space in the focusing beam.

Since the sample was placed far outside the Rayleigh length, the approximate peak intensity was calculated from geometry and found to be $\sim$ 0.52 TW/cm^2 (assuming 7 mm 1/e^2 initial beam diameter). Figure 5.2 shows a dramatic increase in spectrum between the initial ((a) and (b)) and spectrally broadened ((c) and (d)) pulses. The measured FROG traces in Fig. 5.2 of the initial pulse (b) and the pulse after SPM in the 1mm soda lime glass (d) show a significant increase in spectral bandwidth toward lower wavelengths. The reconstructed spectrum and spectral phase can be seen in Fig. 5.2 of the initial (a) and spectrally broadened pulses (c). The spectral phase is seen to decrease in magnitude from $\sim |380|$ fs^2 to $\sim |230|$ fs^2. It is noted here that the spectral fit is

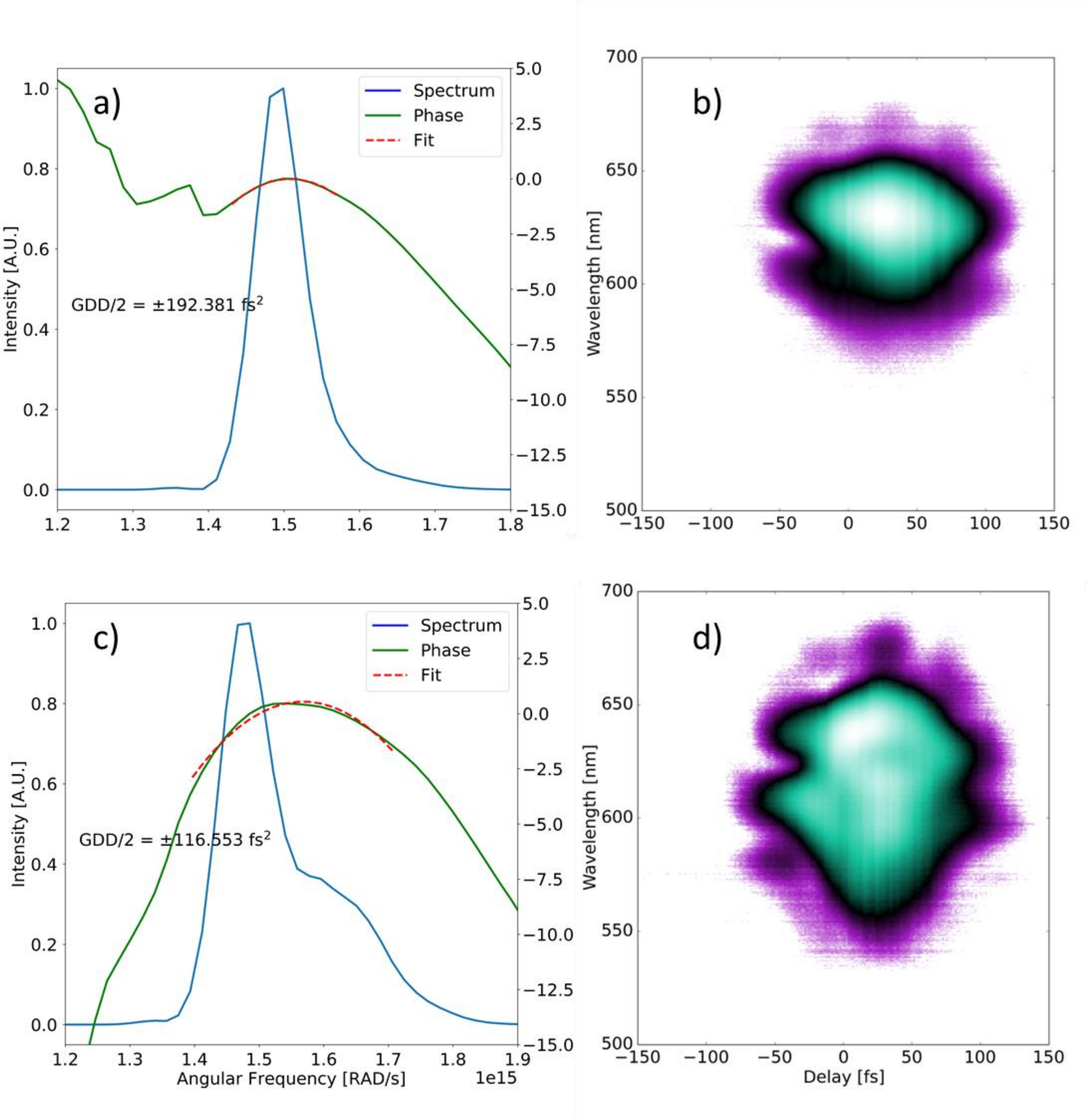

Figure 5.2: The retrieved spectrum (blue) and spectral phase (green) (a) and (c) and corresponding measured FROG traces (b) and (d) of the initial and spectrally broadened pulses. The fitted quadratic phase is noted on the plot and corresponds to the red-dotted line

currently not weighted by the value of the spectrum at a given frequency. The coefficient is determined by the fit to the spectral phase in the frequency range shown by the extent of the red-dotted line.

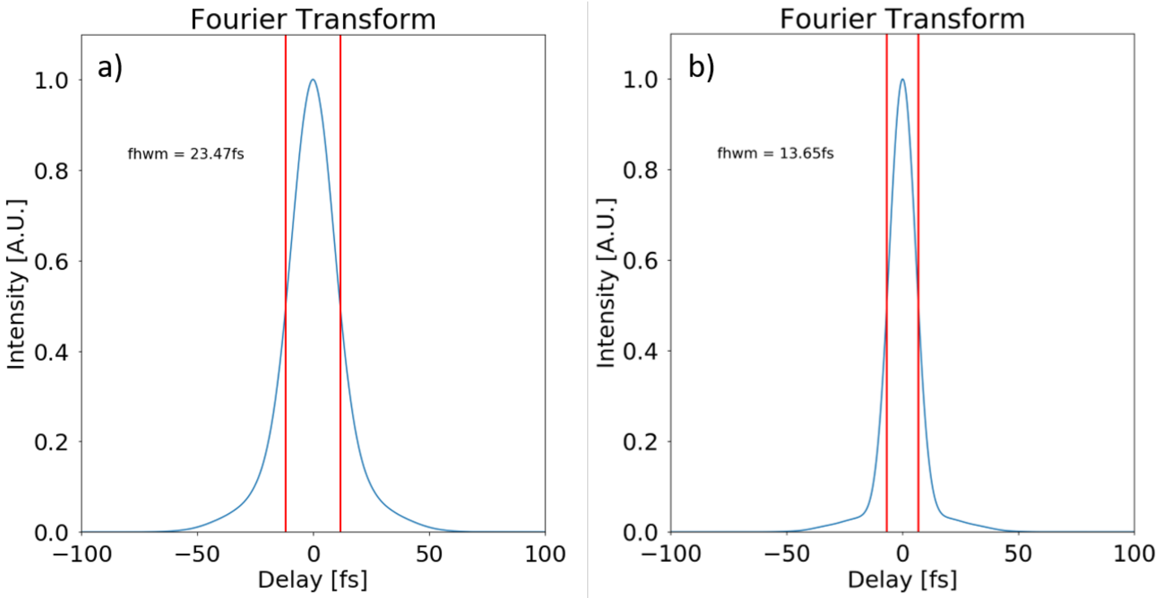

Figure 5.3: The fwhm of the analytical fourier transform of the initial (a) and spectrally broadened (b) pulse. This represents the theoretical limit to the pulse duration that can be constructed by reconstructed spectrum.

5.2 λ-scaling of self-phase modulation (preliminary study)

The second wavelength scaling experiment was meant to explore SPM over a range of longer wavelengths to explore both spectral broadening and the potential for "self-compression" at wavelengths above 1390 nm, where the dispersion becomes "anomalous" in soda lime glass. In this context anomalous means that instead of acquiring positive chirp as we expect in "normal" dispersion, laser pulses at these wavelengths in soda lime glass acquire negative chirp. Further, soda lime glass has a positive n_2 in this range which means the bandwidth acquired through SPM is positively chirped. The combination of adding positively chirped bandwidth while simultaneously compensating that positive chirp with negative chirp gained through dispersion can lead to self-compression [95].

Specifically, this study investigates wavelengths in the range 1140 - 1500 nm over the tuning range of the signal beam from the OPA. The nonlinear index of refraction n_2 is well-known for 800 nm light in some materials (ie. fused silica), but we have the ability to investigate n_2 over a range of wavelengths and materials that it is currently unknown. The more bandwidth generated, the shorter the Fourier transform limited pulse duration will be. Unfortunately immediately preceding this experiment, a significant amount of machining oil was discovered in the breadboards of the small chambers that was left over from their initial manufacture. This meant that the focusing geometry used in the previous section could not be used due to the fact that the turbo-molecular pumps (which were needed for achieving high enough vacuum to avoid creating a plasma at focus) had to be serviced and cleaned.

Therefore, a down-collimating design was used in a larger chamber under low vacuum ($\sim 2 \times 10^{-3}$ Torr) to minimize the nonlinear effects during propagation. In order to induce significant SPM at longer wavelengths where the OPA efficiency is lower, the down-collimating reflective Galilean telescope had to be constructed to produce as small of a beam as possible without burning the positive metal mirrors. A "burn-test" was therefore executed at atmosphere to determine if the gold mirrors would burn with the signal beam at a $1/e^2$ diameter of 1.16 mm (peak intensity ~ 3.53 TW/cm^2). (It is noted here that at the time of the experiment there was more uncertainty about the initial signal beam diameter, making estimates of the peak intensity more uncertain) After ~ 5 min (1.8×10^7 shots) the mirror was examined by eye, and did not have any visible marks. Therefore it was decided that using a down-collimating telescope that exposed the positive dielectric mirror to less than half of the peak intensity (~ 1.55 TW/cm^2) should be safe (it wasn't).

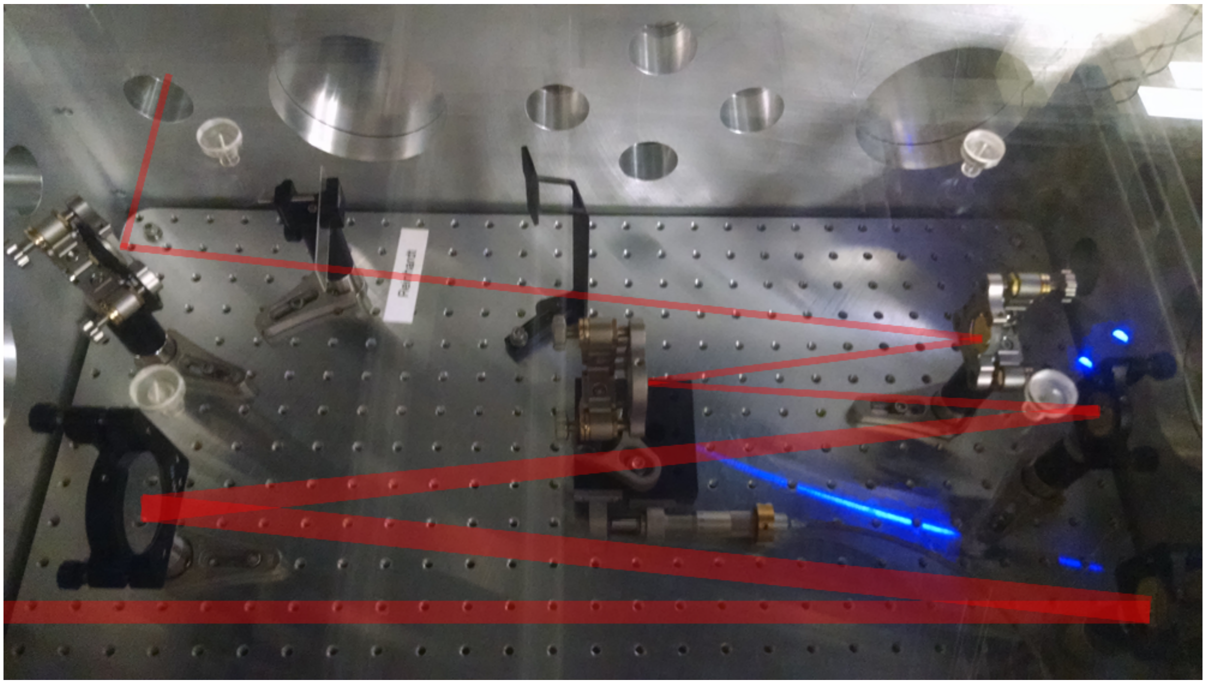

Figure 5.4: The experimental setup of the down-collimating telescope. The signal beam enters from the left and is down-collimated with a reflective Galilean telescope and redirected to the spm target (1mm soda lime glass) and then wedged and redirected out of the chamber to the FROG diagnostic

Figure 5.4 shows the experiment setup in the vacuum chamber. Laser pulses in the wavelength range 1140 - 1500 nm were sent through a c-coated fused silica window and down-collimated to a $1/e^2$ diameter of ~ 1.75 mm. Self-phase modulation was induced in a 1 mm soda lime glass slide at near normal incidence. The S-polarized beam was then wedged to minimize further nonlinear interaction in the c-coated chamber exit window and redirected to the FROG for measurement. FROG measurements were taken in 20 nm wavelength increments with and without the soda lime glass in the beam. As shown in Fig. 5.5 (a), the FTL of the FROG reconstructed spectra were seen to decrease the most near the peak power output of the OPA as expected. It is interesting to note however that at shorter wavelengths the difference in FTL seems to be higher than at longer wavelengths at the same measured power. This seems to suggest that lower wavelengths in this range produce a more significant change in the nonlinear broadening, and therefore have a larger nonlinearity than longer wavelengths. It is noted here however that at the time of this experiment the OPA signal was producing negatively chirped pulses, and since the zero dispersion point of fused silica is $\sim$ 1270 nm, shorter wavelengths will experience slight dispersion compensation (becoming more intense) and longer wavelengths will become more even more negatively chirped (becoming less intense). Though this dispersive effect is likely negligible ($\sim +10\text{fs}^2/\text{mm}$ at 1140 nm, and $\sim -20\text{fs}^2/\text{mm}$ at 1500 nm), it is noted here since it is not explicitly taken into account in the data analysis.

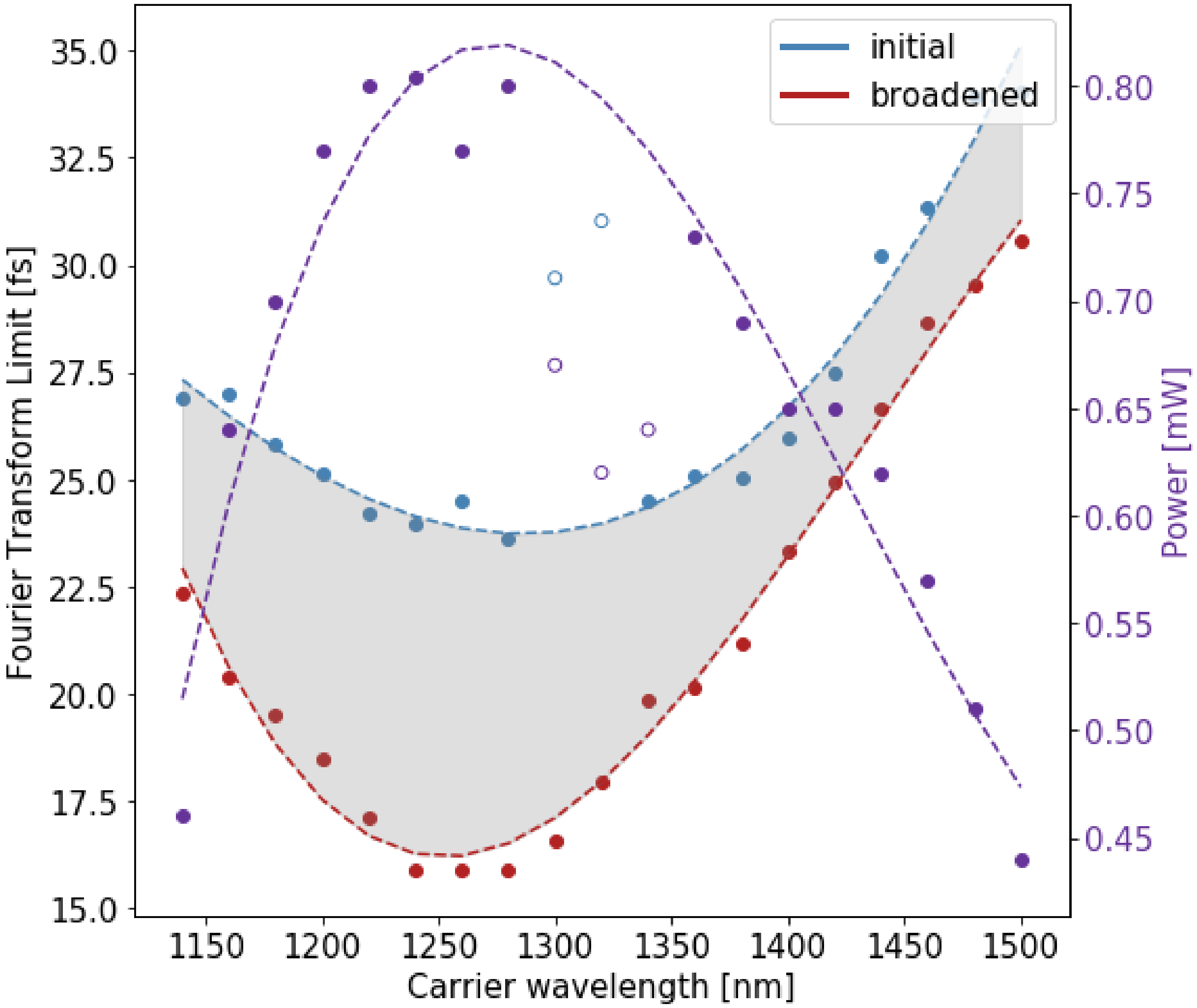

Figure 5.5: The Fourier transform limit of initial (blue) and spectrally broadened (red) laser pulses in 1 mm of soda lime glass in the range 1140 - 1500 nm. the grey shaded region represents the change in FTL.

The dashed lines in Fig. 5.5 are third order polynomial fits to the series of measurements and their functional form does not have any theoretical significance. The utility of these dashed lines should be understood to simply guide the eye. Several data points in the range 1320 - 1360 nm were omitted from the fit to the power and the initial FTL (empty data points) because they appear to be outliers, but are shown here for completeness. It is also noted here that the OPA was optimized not for highest power, but for the most gaussian looking SHG spectrum centered at $0.5\lambda_0$ as measured by the spectrometer. It should be noted that after several hours of operation (in the middle of the experimental run) the gold mirrors and silver positive mirror began to accumulate damage. Images of this damage on the gold mirror can be seen in Fig. 5.6.

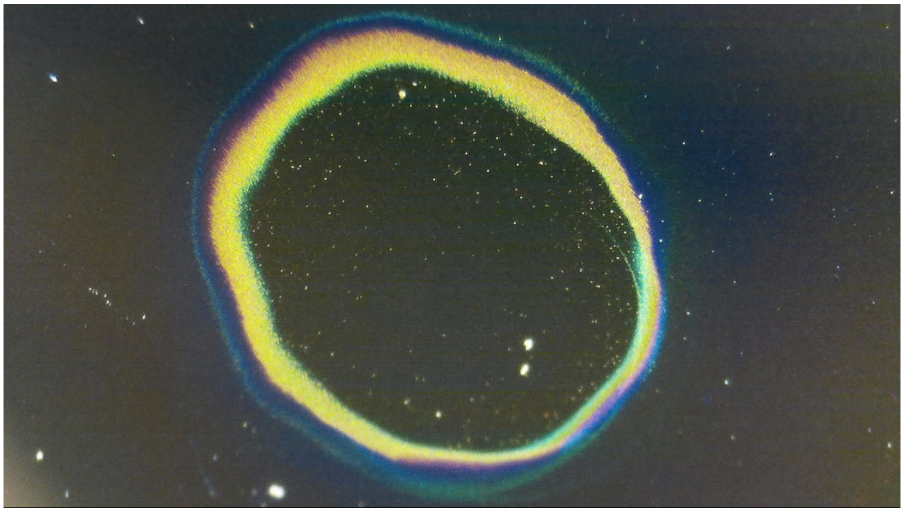

Figure 5.6: Shown above is a magnified image of the surface of the gold mirror. The surface damage to the protective coating accumulated through the course of the experiment.

A follow-up study examining the reflectivity of the mirrors in the seemingly burned regions found that the reflectivity was negligibly effected where the damage appeared to be at 800 nm [96]. This suggests that the damage seems to have been mostly to the coating, leaving the gold surface in tact. Though interesting, since the wavelength scaling of spectral broadening observed in this study is quite modest, performing a wavelength scaling using higher intensities with a focusing geometry under high vacuum akin to the previous section may give more insight into the wavelength scaling of the nonlinear properties of soda lime glass and other materials.

Chapter 6

Laser Wakefields at solid densities

The past few chapters have demonstrated experimental progress with respect to pulse compression of multi-cycle laser pulses toward the single-cycle regime. In Chap. 1 a method of generating x-rays through relativistic compression of optical pulses in the single-cycle regime was presented. This chapter investigates the utility of such relativistic ultrashort high intensity x-ray pulses for driving wakefields in nanomaterials. Using high intensity short-pulse x-rays for driving wakefields gives access to these much higher density materials enabling much higher acceleration gradients than conventional plasma based wakefields.

As explored in several parts of this thesis, electrons can be accelerated to high energies in a wakefield when a short laser pulse propagates through a plasma [21]. Experiments have shown that GeV energies are obtainable over centimeter scale distances in gaseous plasmas by riding the wakefield excited by optical lasers [97, 98, 99, 100, 101]. Laser wakefield theory [21, 102, 103] shows that for a given laser, the energy gain and acceleration length are both inversely proportional to plasma density. This means that the lower the gas density, the longer the acceleration distance required to reach greater energies, an undesirable condition for achieving the goal of ultra-high energies. Motivated by such considerations, utilization of metallic crystals was proposed in the 1980s [104, 105, 106, 107, 108, 109, 110], where TeV/cm acceleration gradient was anticipated. This includes the cases of wakefield acceleration in metallic crystal channels. Another advantage of solid-state guided acceleration is that such a system can naturally provide the mechanism radiation damping. Here the accelerated particle beam emittance, i.e. the transverse momentum, can be dramatically damped through channeling radiation to the ground state of the channels [111]. Under such a scenario, one may even envision head-on collisions of ultra-high energy particles inside these microscopic channels at their ground states, where the classical concept of luminosity is in the so-called quantum luminosity regime, which promises a much higher collision rate [112]. On the other hand, a disadvantage of metallic channels is its high collision frequency with the metallic electrons [113]. This may be alleviated by adopting nanoholes [108, 23, 114, 115].

One of the most important motivating factors of the present paper, in addition to the above, however, is the recent advent of the breakthrough in the laser compression technique that could open a door for an evolution any possibility of a coherent intense X-ray laser pulses in attosecond regimes. The recently proposed scheme of ultrashort, coherent X-ray pulse generation derived from the new optical laser compression [24] into a single-cycled optical pulse, in combination with the relativistic surface compression [3] of such an optical laser into an X-ray laser pulse, provides an attractive possibility to realize such an ultra-high acceleration gradient, for a compact solid-state accelerator scheme to accelerate particles to ultrahigh energies. Thin film compression [24] is a simple elegant method for compression of an ultrafast intense optical laser into a single-cycled optical laser pulse with high efficiency (such as $\sim 90\%$). In turn, such a single-cycled optical laser pulse may be relativistically compressed by the well-known relativistic surface compression [3] as shown in Chap. 1, into a single-cycled X-ray laser pulse, whose photon energies may be up to $\sim$ 10keV [3]. In principle the frequency of the driving X-rays can match the much higher critical density n_c, provided by the conductive solid material which depends inversely to the square of the laser wavelength:

$$n_c(\lambda_L) = \frac{\pi m_e c^2}{e^2 \lambda^2} \approx (1.1 \times 10^{21}[\mathrm{cm}^{-3}])/\lambda_{\mathrm{L}}^2[\mu\mathrm{m}] \tag{6.1}$$

Here c is the light speed in vacuum, m_e is the electron mass, e is the electron charge and λ_L is the laser wavelength. This high critical density by the X-ray laser allows us the additional advantage, i.e. the long dephasing length [21, 23]. One point to notice here is the following. Unlike optical photons, X-ray photons can see even shallowly bound electrons whose binding energy is less than the photon energy (such as 10keV). Thus, even if the material is, for the usual purpose of condensed materials, not a plasma but a bound-state condensed material, X-ray photons see these shallowly bound electrons as if they are (effectively) free electrons. We, therefore, treat such electrons as free electrons as in a plasma. In the following when we call plasma in the solid density for X-rays, we mean such electrons in the condensed material. Additional comments as to the use of the "collisionless model of the particle in cell (PIC) simulation are below and done here. For one, the time scale of the intense X-ray driven electron dynamics is on the order of attoseconds (or even zeptoseconds), so that collisional effects may be ignored in these short time scales. Secondly, in terms of a longer time scale dynamics, we introduce the nanotube materials so that accelerated electron dynamics in the nanotube remain collisionless over an extended time scale of propagation dynamics. For these two reasons of the first order importance is the collisionless dynamics of what we call the plasma driven by intense X-ray. However, unlike in gaseous plasma driven by an optical laser, it is anticipated that the quantum mechanical radiation processes could be far more important. That is why we incorporate quantum radiative effects in our study. Functional nano-materials such as carbon nanotubes have a large degree of dimensional flexibility and allow for a greater than 10 TV/m acceleration gradient. Accordingly, compact structures to obtain ultrahigh energy gain can in principle be realized through the state-of-the-art nanotube technology [23]. A plasma channel is useful for guiding the laser [116, 117], especially for a small laser spot. For an X-ray beam with a spot size at the nanometer level, stable propagation is important for the purpose of wakefield generation and acceleration. Available nanometer structures [118, 119, 120, 5] such as porous alumina as shown in Fig. 6.1 [119, 5] and carbon nanotubes provide an excellent prospect to guide the X-ray pulse while additionally guiding and collimating the high energy beam being accelerated, providing well-organized beam optics control. In such a material while the nanohole provides a good collisionless particle propagation, the surrounding nanomaterial supports the robust wakefield, where the X-ray laser aperture may cover a sufficient area. Furthermore, the honey comb repeated structure allows us to easily raster the X-ray laser pulses with repeated high repetition irradiations. Also importantly, the beam emittance is damped through channeling, or betatron, radiation as mentioned above [112].

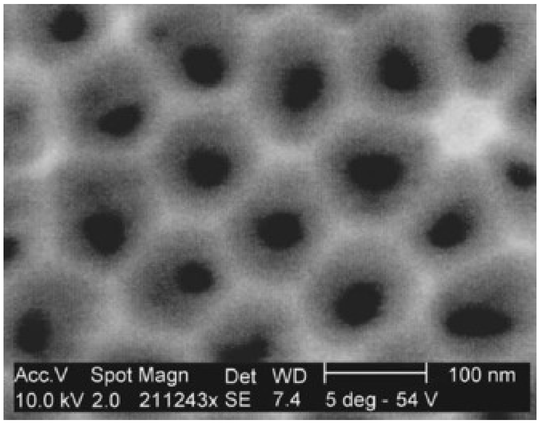

Figure 6.1: SEM image of the top surface of a porous alumina sample [5].

Motivated by these points, in this paper we explore an X-ray wakefield accelerator within a nanotube. By comparing the two cases of a coherent, ultrafast X-ray pulse and 1eV optical laser, the identical wake structure after normalization to the laser wavelength has been confirmed in the limit of the collisionless PIC modeling. However, the radiation in these two cases are quite different when the effect of quantum electrodynamics (QED) is considered. Photons with energy ∼ O(10MeV) have been generated in the X-ray laser case for the much stronger wakefield and the emittance of energetic electrons becomes three orders of magnitude lower. Based on the simulation results, we summarize the wakefield scalings with laser intensity, nanotube radius, and nanotube density.

6.1 Nanotube versus uniform plasma

In the kind of intense irradiation of such an X-ray laser onto a solid material regardless if it is a metal or dielectric, the high energy of photons ($\varepsilon = h\omega_L \sim O(\text{keV})$, where ω_L is the laser frequency) and the high intensity ($a_0 = eE_L/m_e\omega_L c = O(1)$, where E_L is the laser field) both contribute to allow us to treat the material well approximated as plasma at a metallic density as mentioned in the previous section [104, 105, 106, 23]. The high energy of the photons makes a substantial amount of electrons (either the electrons in the conduction band or in the shallowly ($<$ 1keV) bound electrons) respond to the X-ray fields directly. The high intensity of the X-ray pulse results the instantaneous ionization of some of the bound electrons per atomic site, thereby contributing to free electrons. Even some remaining bound electrons may be treated a solid plasma as shown in Ref. [121], where additional optical phonon modes and Buchsbaum resonances are allowed. Two dimensional (2D) PIC simulations have been performed by using the EPOCH code written in SI units [122]. The simulation box is 60 nm(x) × 100 nm(y), which corresponds to a moving window with 3000 × 500 cells and ten particles per cell. For the base case, the laser and plasma parameters are listed in Table 6.1. The laser pulse of wavelength $\lambda_L = 1$ nm (corresponding 1keV X-ray laser), the normalized peak amplitude used is $a_0 = 4$ which means the peak pulse intensity is $2.2 \times 10^{25}/\text{cm}^2$. The tube wall density is given in terms of the critical density by $n_{tube} = 4.55 \times 10^{-3} n_c$. That is, for modeling the

Laser wavelength λ_L	Peak amplitude a_0	Laser width radius σ_L	Laser length radius σ_x	Plasma density n_{tube}	tube radius σ_{tube}
1 nm	4	5 nm	3 nm	$5 \times 10^{24}/\mathrm{cm}^{-3}$	2.5 nm
1 µm	4	5 µm	3 µm	$5 \times 10^{18}/\mathrm{cm}^{-3}$	2.5 µm

Table 6.1: Summary of the laser and plasma parameters for the base case

nanotube, a solid tube with wall density of $5 \times 10^{24}/\mathrm{cm}^3$ is used. The tube location is $2\lambda_L < x < 8000\lambda_L$ and $-5\lambda_L < y < 5\lambda_L$. At $t = 0$, the laser pulse enters the simulation box from the left boundary.

Figures 6.2 and 6.3 show the comparison between the nanotube case and uniform density case driven by the X-ray pulse, in which a small spot size of over a short length of is chosen according to the approach proposed in Ref. [48]. For the uniform density case, see Fig. 6.2 (b, d, f, h) and Fig. 6.3, the Rayleigh length is short due to the small spot size, so the laser pulse quickly diverges as it propagates. Due to the defocusing laser field, the laser field decreases rapidly with the propagation distance, and thus the strong longitudinal wakefield only keeps a very short time and then goes weaker and gradually disappears. In this case, the driving pulse dissipated after propagating a distance of $2000\lambda_L$and the wakefield is not stable during the whole process. However, in the nanotube case, as we see in the Fig. 6.2 (a, c, e, g) and Fig. 6.3, the X-ray pulse maintains a small spot size that can be well controlled and guided by the surrounding nanotube walls. The induced wakefield stays stable and the short laser pulse continues propagating even after a distance of $4500\lambda_L$, which is more than twice that of the uniform density case. By comparison, we see the nanotube wakefield is akin to the nonlinear wakefield in the bubble regime, while the uniform plasma wakefield seems to be rather quasi-linear wakefield. Both the longitudinal wakefield contributing to the accelerating force and transverse wakefield contributing to the focusing force on electrons are more stable and appropriate in the nanotube case. This stability over a long distance is important for the acceleration to obtain a high energy beam. Thus we see superior wakefield quality in a nanotube in comparison with the case in its comparable uniform medium.

To make a comparison, the simulations driven with an optical 1 eV laser pulse under analogous conditions are carried out. In this case when the same $a_0 = 4$ is used for the laser wavelength of $\lambda_L = 1$µm, it corresponds to a laser peak intensity of 2.2×10^{19} W/cm^2. It is expected that the wake structures are almost identical after all physical parameters are normalized by the laser wavelength and the simulation results confirm this. Considering the real physical parameters, it can be found the wakefield is higher than 2 TV/cm when driven by the X-ray pulse, which is three orders higher than that of the optical laser case. This means the energy gain gradient is 2 TeV/cm instead of 2 GeV/cm and opens the possibility to realize a very compact accelerator capable of reaching ultrahigh energies. In addition, the wakefield for the uniform plasma case can be estimated from $E_0 = a_0^{\sim 1-2} m_e \omega_p c/e$, which is about $2.2 a_0^{\sim 1-2}$ TV/cm using the parameters in above simulations, where ω_p is the plasma frequency. This expected value agrees well with the observed one in Fig. 6.2, which means in the narrow limit of the tube, the wakefield scaling resembles that in the uniform plasma formulation.

6.2 Optical versus x-ray driven nanotube wakefields

Similar momenta (energy gains) are expected if the same ratio is kept between the laser and plasma wavelengths over one dephasing length, irrespective of the laser wavelength and background density. However, for the electron beam accelerated in the X-ray driven wakefield, one important signature is that the emittance can be improved significantly due to the much smaller size in the transverse dimension. As well known, beam emittancerelated to both the transverse dimension and the electron momentumis an

Laser wavelength λ_L	Peak amplitude a_0	Laser width radius σ_L	Laser length radius σ_x	Plasma density n_{tube}	tube radius σ_{tube}
1 nm	10	5 nm	3 nm	$5 \times 10^{24}/\text{cm}^{-3}$	2.5 nm
1 µm	10	5 µm	3 µm	$5 \times 10^{18}/\text{cm}^{-3}$	2.5 µm

Table 6.2: Summary of the laser and plasma parameters for the electron acceleration case

important parameter with many applications requiring it to remain low. Similar energy gain is confirmed in Fig. 6.4, which shows the wakefield (a,b) and the relativistic factor (c,d) of the accelerated electrons driven by an X-ray pulse and an optical laser, respectively. The laser and plasma parameters are listed in Table 6.2 for the electron acceleration case. Here a higher $a_0 = 10$ is used to ensure the occurrence of self-injection. Fig. 6.4 demonstrates the confinement of the top 30% of the highest energy electrons locally within the nanometer-scale tube for the X-ray driven case. We see the accelerated electrons is broken into two main parts. This is because electrons are trapped non-consecutively because of the nonlinear evolution of the wakefield. Moreover, electrons of energy below top 30% are excluded, so the cut phenomenon is much clearer. The transverse radius of the electron beam is almost three orders of magnitude smaller than that of the optical laser case, while the phase space remains nearly the same, which is beneficial to the beam emittance. According to the expression [123] for the beam emittance which is given by,

$$\varepsilon_{N_{rms}} = \langle \gamma\beta \rangle \sqrt{\langle y^2 \rangle \langle y'^2 \rangle - \langle yy' \rangle^2} \tag{6.2}$$

where $\gamma\beta$ is the momentum, $y' = p_y/p_x$, and p_x, p_y are the longitudinal and transverse momenta, the normalized emittance of the top 30% highest energy electrons for the X-ray case is about 0.0187mm mrad, which is almost three orders of magnitude smaller than the 28.5mm mrad for the optical laser case. Such an electron beam with low emittance and promising ultrahigh energy holds potential for the application for a future collider. In addition to this, there are also other promising advantages by using the nanotube, such as the better field structures for the significant improvement of the acceleration as concluded in Ref. [124] in the optical laser case. These may be observed in Figs. 6.2 and 6.3. In addition, the linear density of top 30% and 80% highest energy electrons (that is, electrons of energy higher than $E_{e1} = 604$ MeV and $E_{e2} = 173$ MeV are considered) is 3.2×10^{14}/m and 1.54×10^{15}/m for the case of optical laser, and the linear density of top 30% and 80% highest energy electrons (electrons of energy higher than $E_{e1} = 621$MeV and $E_{e2} = 177$ MeV are considered) is 3.1×10^{14}/m and 1.56×10^{15}/m for the case of X-ray laser. Here top 80% is chosen instead of 100% to exclude the immobile background electrons. Assuming that the third dimension is proportional to the wavelength, the number of accelerated electrons in the X-ray laser case is 103 times lower than that in the optical laser case. Here one point that should be emphasized is that the total laser energy $\varepsilon_L \sim a_0^2 \sigma_L^2 \sigma_x / \lambda_L^2$ which also scales with the laser wavelength, that is, the X-ray laser energy is 10^3 times smaller than that of the optical laser. The energy transfer efficiency from laser to accelerated electrons is nearly unchanged. The emittance of top 80% energetic electrons is 0.069 mm mrad for the X-ray laser, while the emittance of top 80% energetic electrons is 64 mm mrad for the optical laser, 10^3 times lower than that in the X-ray laser case.

It is well known that electrons also undergo betatron oscillations due to the transverse wakefield as they are gaining energy in the longitudinal wakefield and radiate X-ray or gamma-ray photons [125, 126, 7]. As mentioned above, when the ratio between the laser and the plasma wavelengths is constant, the energy gain is almost the same. However, the betatron radiation is quite different and cannot be normalized by the laser wavelength when QED effects are considered because the photon emission scales with the real electric field while the energy gain scales with the normalized laser amplitude a_0. As shown in Figs. 6.4 and 6.6, similar wakefield structure and energy gain, but quite different photon energy distributions in the two different laser wavelength cases are shown. Hundreds of keV to MeV photons are generated in the optical laser case, in which the high energy may be resulted from the wide oscillating radius since the injection position in transverse direction depends on the tube diameter. On the other hand, although the electron energy gain is only several hundred MeV, which is almost the same as that of the optical laser case, the photon radiation energy is high to hundreds of MeV when undergoing the much stronger field in the X-ray laser case, which may be applied in astrophysics research, and cosmic ray generation.

According to the classical radiation theory [127, 7], the photon critical energy due to betatron radiation scales with $\gamma^2 n_e r_\beta$, where γ is the electron relativistic factor, n_e is the electron density and r_β is the betatron amplitude, which implies there should be an increase by a factor of $1/\lambda_L$ in the photon energy for the X-ray case over that of the optical laser case. However, the simulation including QED effects shows it to be smaller than this, or about a factor of 200 as seen in Fig. 6.6. This results from the quantum effects and can be partially explained by the replacement of $\nu \to \nu(1 + h\nu/E)$, which shows the quantum mechanical correction, where ν is the photon frequency and E is the electron energy [61, 128].

In addition, according to QED theory [129], if the QED parameter $\eta = \gamma E \sin\theta / E_{crit}$ is close to, or of order unity, the QED effects become important. Here θ is the angle between the electric field E and the electron momentum, and $E_{crit} = 1.3 \times 10^{16}$ V/cm is the Schwinger field. According to classical theory, electrons are expected to emit photons with a most probable value of $\hbar\omega_{mp} = 0.44\eta\gamma m_e c^2$. Using the maximum energy electrons in the wakefield $\gamma = 1700$, which experiences a transverse wakefield of $E \sim 5 \times 10^{12}$ V/cm [of the order of longitudinal wakefield as shown in Fig. 6.4 (a)], the maximum QED parameter is found to be $\eta_{max} = 0.577$. Therefore, the expected value of most probable photon energy corresponding to the highest energy electrons is predicted to be $\hbar\omega_{mp} = 221$ MeV. This expected value agrees reasonably well with the observed photon cut-off value $E_{p-cutoff} = 300$ MeV as shown in Fig. 6.6 (c). Here one point should be noted that there is nearly no difference of the electron energy between Fig. 6.4 (c) and (d), which means there is little radiation reaction effect in the X-ray laser case although the photon energy is much higher than that in the optical laser case. By comparing with the case in which the radiation reaction was turned off for the X-ray laser case, the results turn out that little radiation reaction effect on electron beam dynamics, i.e., energy and emittance are found. According to the Landau-Lifshitz prescription [129], the ratio of the damping force (radiation reaction force) to the ordinary Lorentz force scales with $\gamma^2 E$. In the X-ray laser case, E is about 10^3 times higher, which means the radiation reaction force becomes much more important. However, the energy loss of electrons (radiation reaction effect) depends on the acting time/distance, so radiation reaction effect in the X-ray laser case is possible to be weak because of the much shorter (10^3 times) acting time/distance. In addition, the ratio of the total energy of all photons to the total energy of all electrons is 9.4×10^{-3} in the X-ray laser case. That means the radiation reaction effect is still weak, although the value is much higher than that of 2.2×10^{-5} in the optical laser case. According to the above analysis, the effect of the laser frequency on the betatron radiation is expected to be quite important under the condition of the same laser power. For the current laser level in the near term, the triple frequency ($3\omega_L$) laser can be chosen to drive a more intense wakefield and get higher energy photons. Simulations have confirmed that, driven by the triple frequency laser, the obtained average photon energy is at least twice of that from the fundamental one, which can be considered as an effective approach to increase the radiation photon energy.

6.3 Scalings in the x-ray regime and discussion

Here we survey the property of X-ray wakefield acceleration in nanotubes with respect to several parametric scalings. Compared with the uniform density case, the laser pulse can be well confined in the nanotube and propagate over a longer distance. Therefore, the tube radius is critical to the wakefield and the acceleration in addition to the other two common parameters, i.e., laser intensity and tube density. Fig. 6.7 (a) shows the result when the tube radius varies while the other parameters are kept the same. The wakefield is strong due to the nonlinear evolution when the tube radius is small. As the radius ratio goes up, the effective density decreases. This results in a decrease in wakefield strength since it is proportional to the density, and energy gain is expected to increase if the ratio is not too large because the acceleration length is extended. In the present case, the wakefield scales with the tube radius ratio as $E_x \propto (\sigma_{tube}/\sigma_L)^{-1.827}$. It should be noted that when the tube radius is small or can be compared to the laser pulse width, such as the present cases, the physics becomes closer to a uniform plasma case. On the other hand, for much wider tube cases, the wakefield becomes less intense and deviates away from the uniform plasma wakefield acceleration. For this case, the physics may more closely resemble to the dielectric wakefield acceleration [123, 130, 131, 132]. However, the driving unwanted higher order-mode (dipole, quadrupole, etc) in this case may be an issue, which is different with the present plasma regime where only the plasma frequency is important for acceleration. When the channel radius is fixed, for example as in Fig. 6.7 (b), $\sigma_{tube}/\sigma_L = 1$, at first the wakefield increases along with the tube density (n_{tube}) but tends to saturate because it is hard to excite a wakefield when the parameters of the laser pulse and density are mismatched. More importantly, the significant feature is that lower density results in higher energy gain. The wakefield scales with the tube wall density as $E_x \propto n_{tube}^{0.47}$ in the low density region. When the laser intensity (a_0) goes up, the effective density grows higher because of the increasing plasma wavelength. In the present case, the wakefield scales with the laser field as $E_x \propto a_0^{1.875}$ when $\sigma_{tube}/\sigma_L = 0.5$ and $E_x \propto a_0^{1.763}$ when $\sigma_{tube}/\sigma_L = 1$, which shows a similar scaling for different radius ratios. Compared with the linear wakefield theory $E_x \propto \omega_p \propto n^{1/2}$, 1D nonlinear theory $E_x \propto (a_0^2/2)(1 + a_0^2/2)\omega_p$ [103] and 3D nonlinear (Bubble) theory $E_x \propto a_0^{1/2}\omega_p$, $\omega_p \propto n_e^{1/2}a_0^{1/2}$ [102] in the uniform plasma, as well as the previous theoretical results on X-ray wakefield accelerator in solid-density plasma channels $E_x \propto \omega_p P^{1/2} \sim n_e^{1/2}a_0$ [133, 134, 114], the wakefield scaling with the wall density in our the nanotube case is in principle agrees with the theory expected as $E_x \propto n^{1/2}$ in the uniform density case and the wakefield scaling with the laser intensity is close to the 1D nonlinear theory.

For the parameters in the above discussion, there are several technological challenges to be considered in the experiments, such as the X-ray intensity and wakefield strength, the focus of such X-ray beam onto a nanometer size tube, and the compression of the present state-of-the-art coherent X-ray pulse down to a few nanometers. In reality, in the short term the parameters can be extended to the acceptable region since the results scale with the laser wavelength. On the other hand, as we know, wakefields may be created not only by lasers, but also by a beam of electrons or ions because the plasma responses to these drivers are essentially the same [135, 136]. Beam driven acceleration in ultra-dense plasma, including a hollow plasma channel with density of $10^{25} - 10^{28}/\mathrm{m}^3$ has been explored [104, 105] and a high acceleration gradient of TeV/m has been obtained [115]. Moreover, a hollow channel, as a more efficient structure in controlling beam parameters in the dense plasma interaction, has been confirmed. In this beam driven case, beam density is especially critical to increasing the acceleration gradient, just as with the laser intensity. When the beam density is high enough to be compared with that of the dense plasma, such as $10^{30}/\mathrm{m}^3$, and the beam size is small enough to be at nanometer scale (however, these are tall orders in the current beam technology), similar results with that driven by the X-ray are expected. In the short term, particle beams instead of X-ray lasers can be used as the driver in a nanotube. For current particle beams, as they pass through a nano-material, a periodic pattern such as wakefield is expected to be generated. Such patterns can serve as optical elements for the beam, and, correspondingly, linear phenomena such as diffraction, beam bending or focusing, are expected to be exhibited.

6.4 Conclusion

In conclusion, owing to the latest invention of the thin film compression technique, one single-cycled optical laser pulse can in principle be converted into a coherent ultrashort X-ray pulse via relativistic compression. A new and promising scheme employing such an X-ray driven wakefield in a nanotube has been demonstrated by a computer simulation for a compact accelerator to attain ultra-high acceleration gradient for charged particle acceleration. In this case, an acceleration gradient of TeV/cm is generated and high energy electrons with much lower emittance are obtained in such a wakefield. In a very narrow limit of the tube, the energy scalings resemble those in the uniform medium formulation. In addition to the aspect of acceleration, under the X-ray driven nanotube wakefield scheme, hard photons with energies at $\sim$ O(100MeV) are emitted. Those may be invoked as a tool to serve as a novel light source in very high energies in a compact fashion and to explore more unknown physics, although there are several technological challenges in the future in the realization of the experimental operation and parameters suggested in our work. These include such an X-ray laser pulse generation and the manipulation of such small size laser and target. In this regard the recent thrust in ultraintense laser developments [25] leads us to a high hope that such projects can accelerate the progress in this new exciting field with an added impetus.

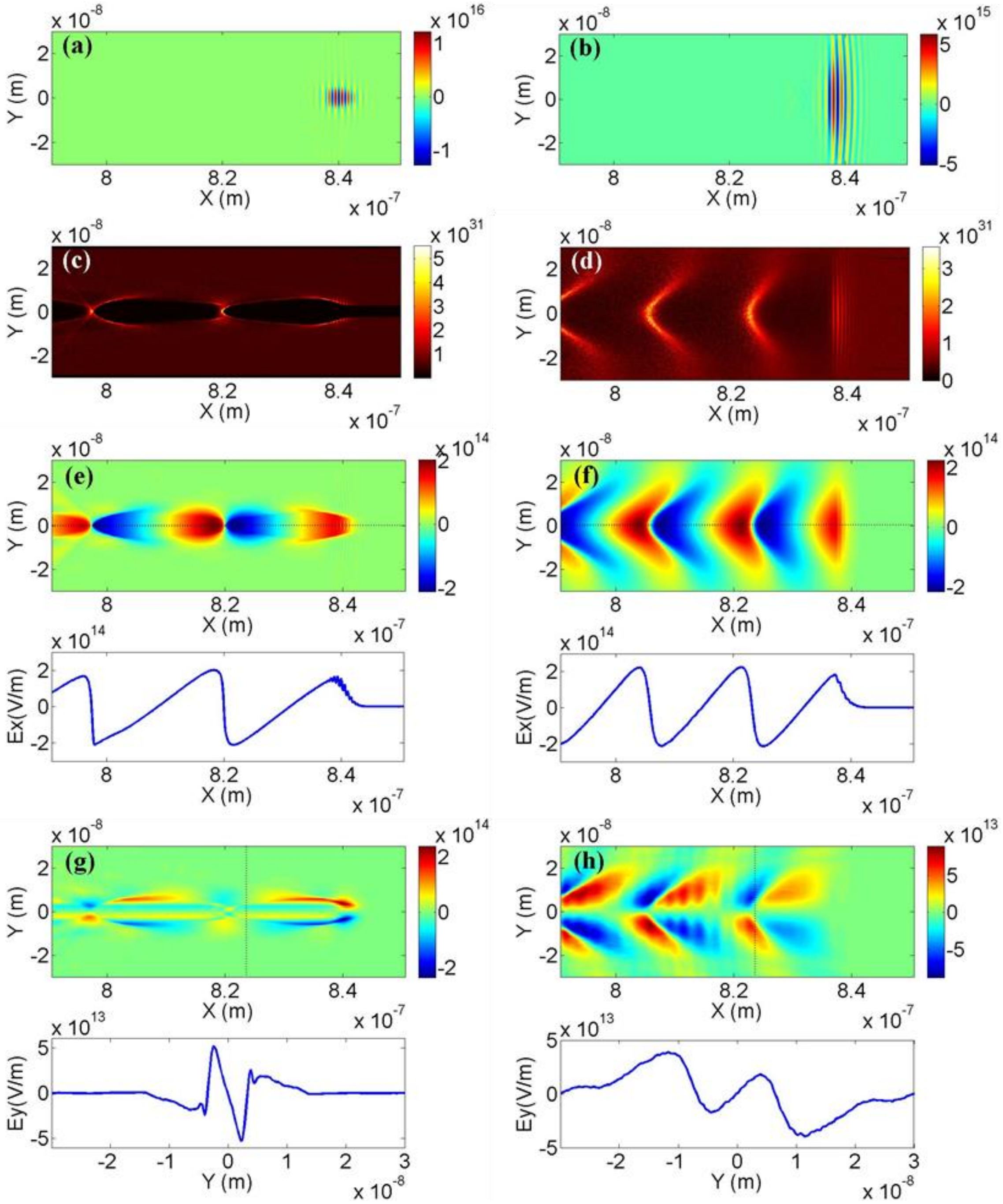

Figure 6.2: The base case wakefield excitation with X-ray laser in a tube, in comparison with a wakefield in a uniform system. Distributions of (a) and (b) the laser field E_z(V/m), (c) and (d) electron density n_e(m^{-3}), (e) and (f) longitudinal wakefield E_x(V/m) including the E_x lineout at $y = 0$ axis (the position of dot line), and (g) and (h) transverse wakefield E_y(V/m) including the E_y lineout at $x = 8.24 \times 10^{-7}$m axis (the position of dotted line) in terms of (a),(c),(e) and (g) tube and (b),(d),(f) and (h) uniform density cases driven by the X-ray pulse.

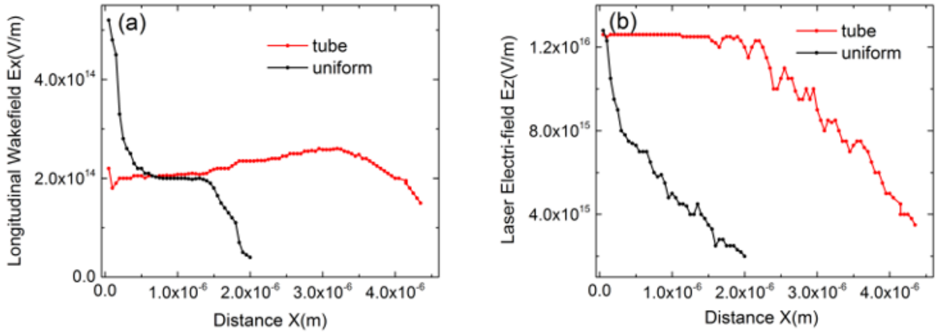

Figure 6.3: Evolution of the maximum longitudinal wakefield E_x(V/m) and the laser field E_z(V/m) as a function of propagation distance x(m) for both nanotube (red dotted line) and uniform plasma (black dotted line) cases with the same conditions as Fig. 6.2.

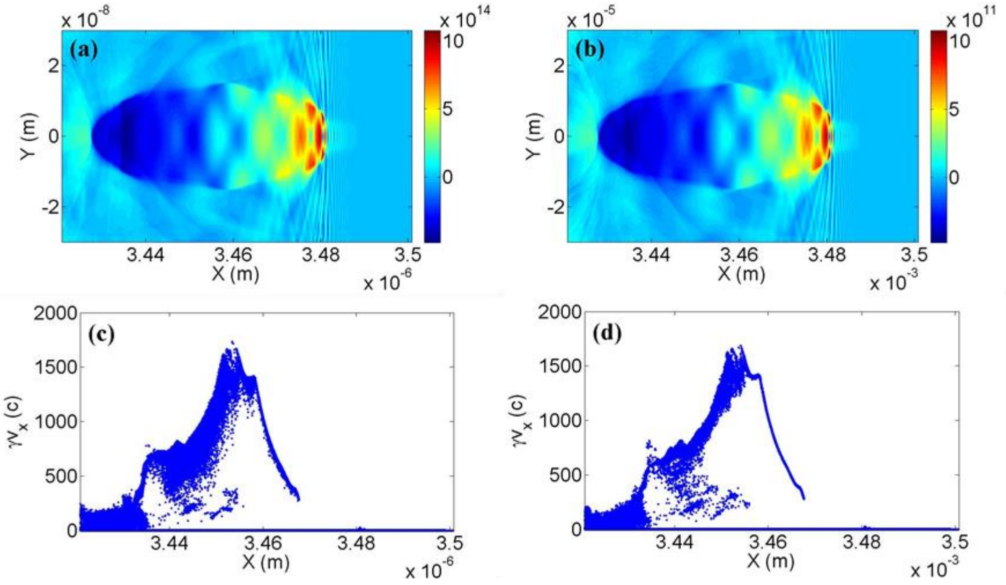

Figure 6.4: Comparison and a certain scalability between the X-ray and optical regime. Distributions of (a) and (b) the longitudinal wakefield Ex(V/m) and (c) and (d) electron longitudinal momentum γv_x induced by (a) and (c) the X-ray laser pulse and (b) and (d) 1eV optical laser pulse in a tube when $a_0 = 10$.

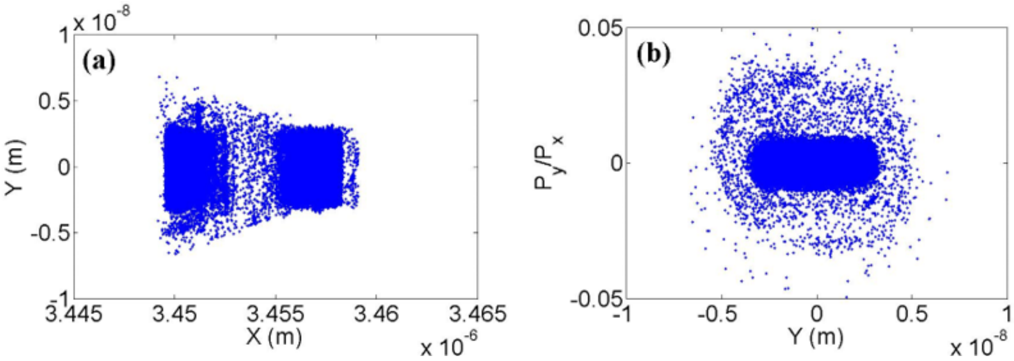

Figure 6.5: (a) The accelerated electron beam quality in the X-ray wakefield in a tube. The space distribution (x, y) and (b) the transverse phase space $(y,\ py/px)$ of the top 30% highest energy electrons in the case of X-ray laser. The parameters are same as in Fig. 6.4.

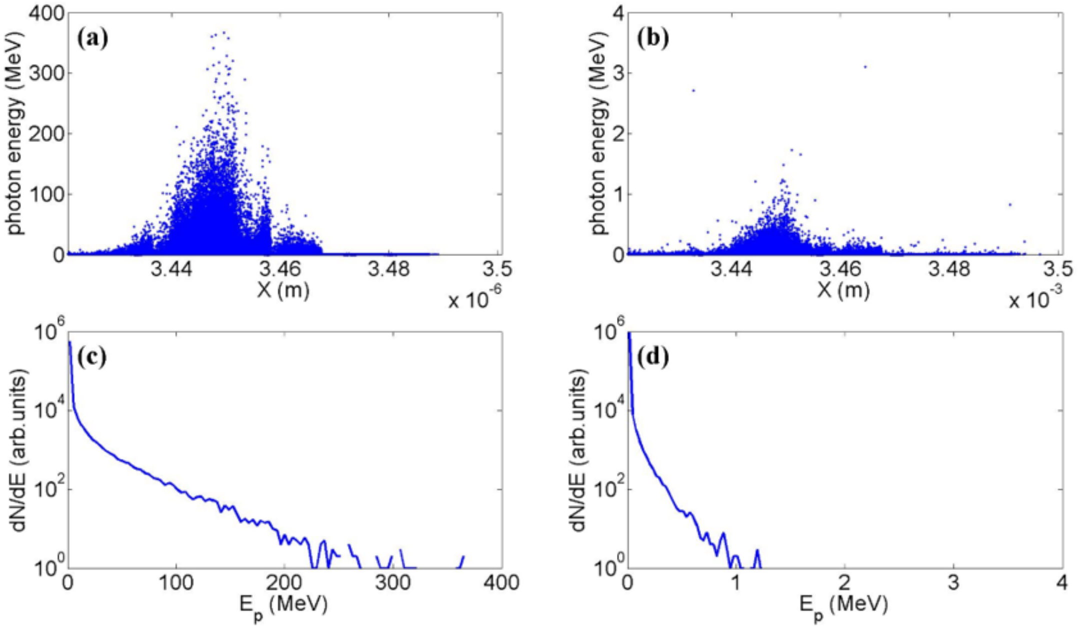

Figure 6.6: The energy spectrum and spatial distribution of photons emitted from the wakefield driven by an X-ray and optical laser. (a) and (b) Photon energy distributions and (c) and (d) photon energy spectrum in the (a) and (c) X-ray driven case and (b) and (d) 1eV optical laser driven case in a tube. The parameters are same as in Fig. 6.5.

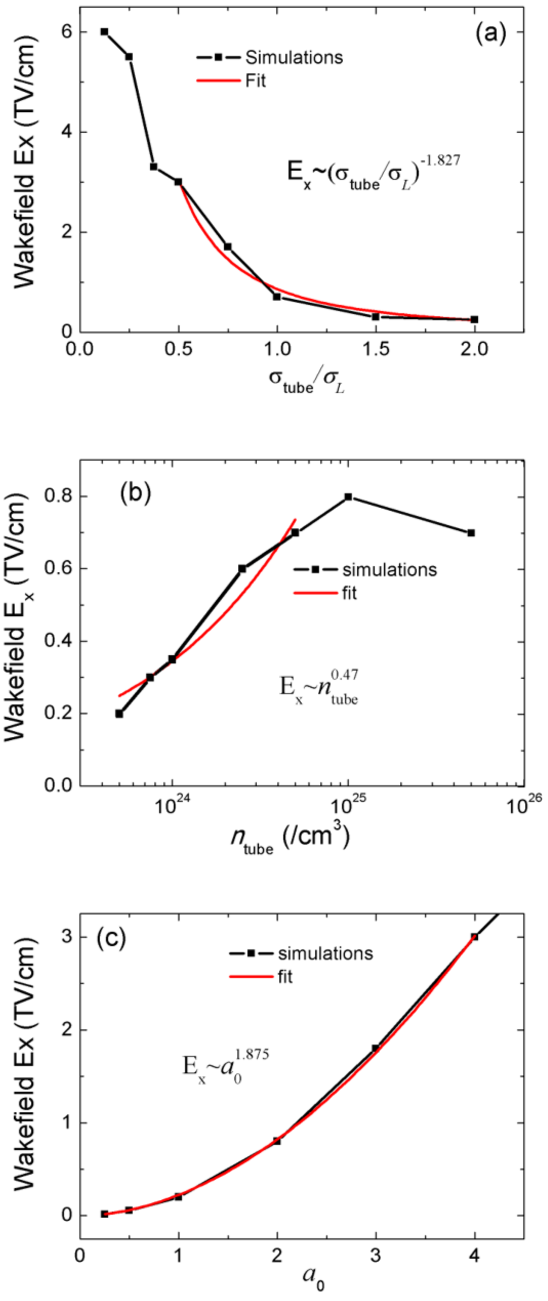

Figure 6.7: Wakefield scalings in the X-ray regime with (a) tube radius, (b) tube wall density when the tube radius is fixed $\sigma_{tube}/\sigma_L = 1$, and (c) laser intensity when the tube radius is fixed $\sigma_{tube}/\sigma_L = 0.5$

Chapter 7

Wakefield astrophysical scaling investigation

In addition to providing ultra compact particle acceleration and high energy photon emission in laboratories on earth, laser wakefields also may be a contributing radiation mechanism present in the jets of active galactic nuclei such as blazars. This chapter considers this claim by investigating the electron acceleration and photon emission characteristics of wakefields under typical laboratory conditions and scales them in the direction of the astrophysical environment to motivate recent observational findings.

7.1 Introduction

The laser wakefield acceleration (LWFA) [21] method and its sister beam-driven wakefield acceleration [135, 136] (let us call here wakefield acceleration (WFA) in general) have found themselves in laboratories for future accelerators of various purposes. In LWFA, the robust intensity of the laser pulse is such that the ponderomotive potential (the photon pressure force potential) of the laser in the plasma amounts to $\Phi = mc^2\sqrt{(1+a_0^2)}$, so that the excited plasma wave motion acquires the electron momentum of mca_0. Here the normalized vector potential of the laser is $a_0 = eE_0/m\omega_l c$, where E_0 and ω_l are the electric field and frequency of the laser, m and c are the mass of the electron and the speed of light. The ponderomotive force arises from the nonlinear Lorentz force $v \times B/c$, which causes the polarization of electrons in the plasma in the longitudinal direction, even though the electric field of the laser is in the transverse direction. This polarization $E_p = m\omega_p ca_0/e$ yields the electrostatic field in the longitudinal direction in turn in the same magnitude. This is the origin of the excited wakefield. More details may be found in reviews such as Refs. [137, 103, 138, 7].

Recently LWFA finds applicability in the regime of much higher frequency laser pulses than the original optical regime, i.e. in the X-ray regime. This development occurred due to the invention of a novel laser compression method [24], in which a single cycled optical laser pulse may be created by a thin film technique. This development immediately triggered the possibility to compress it further to create a single-cycled X-ray laser by adopting the already known approach of relativistic compression of ultra-short laser pulses (particularly effective if it is a single-cycled optical pulse) on the surface of solid metallic target [3]. This opening of a (relatively) straightforward path toward ultra-high intensity single-cycled X-ray laser pulses stimulated the thought of using such X-rays in driving LWFA at solid densities [83, 23, 139].

In addition to the high frequency and density applications the LWFA mechanism may be also present in nature. Ebisuzaki and Tajima have suggested [140] that LWFA underlines the acceleration mechanism present in jets of an active galactic nucleus (AGN). This mechanism not only allows for the possibility of extremely high energy ion acceleration, but also seems to chime well with the accompanying phenomenology of gamma ray burst emission based on WFA electrons. The earlier work found in Refs. [141, 142, 143] laid the foundation of this work [140]. Since the well-known astrophysical acceleration mechanism of Fermi [144, 145] is inherently stochastic, the Fermi acceleration process tends to lose rather than gain energy by synchrotron radiation even off protons at the highest energy cosmic ray regime ($> 10^{19}$ eV), while the LWFA mechanism sees no such limitation [140]. In the AGN the electromagnetic pulse that drives the LWFA process is in very low frequency radiowaves. Thus the original LWFA in the optical regime has, on one hand, extended itself to much longer wavelengths of radiowaves in astrophysics and now, on the other hand, to much shorter wavelengths of X-rays. These broad ranges of LWFA applicabilities in density of plasma, frequency, and intensity of drivers prompt us to investigate the radiative signatures involved in WFA, which otherwise may not matter in the more "traditional regime" of parameters.

For the above mentioned astrophysical processes and cosmic ray genesis the understanding of the radiative processes is very important, as almost all observational information comes from the radiation of various frequencies. In laboratory LWFA experiments studies of radiation such as betatron radiation from LWFA have gained their importance in recent years (see Refs. [125, 7]). In addition, as our interest rises in the X-ray driving of LWFA, which implies much higher density operation of the wakefields and related radiative processes, it is expected that some quantum mechanical radiative processes may become important under such conditions. These prompt us to consider with increased importance, the radiations from LWFA, particularly that from betatron radiation. We thus put emphasis on this in our study. If the radiative processes in the X-ray regime are distinct from those in the optical regime, we may have a unique opportunity and invent devices related in the X-ray regime exploiting such an opportunity.

On one hand, the basic physics of LWFA applies regardless of its frequency domain, an attractive attribute of its fundamental mechanism. On the other hand, it is of interest to explore if and how the disparately different scale-lengths may change some of the physics and implications. In this work we first study scaling laws of the basic LWFA and its self-injection of electrons and its associated betatron radiation processes so that we can glance at the broad LWFA horizon. It is also noted [140, 146] that as the laser becomes highly relativistic, the relative importance of the ponderomotive acceleration itself rather than its induced wakefield acceleration becomes important, where the highly relativistic regime is defined by $a_0 >> 1$. For this reason we will investigate the scaling laws for both LWFA and ponderomotive acceleration processes and their associated radiative processes here.

In Sec. 3 we give a brief overview of the numerics used in the simulations, describe the base case, and introduce the laser and plasma parameters. Further, we outline our methodology for investigating LWFA electron acceleration and high energy photon emission. Specifically, we examine the energy evolution, trajectory, and ultimately energy saturation of injected electrons. The resulting maximum electron energy saturation ($\varepsilon_{e,max}$) is utilized in predicting the expected high energy photon emission characteristics. We then create a time-integrated photon spectrum of the emission data from the fraction of the simulation window containing electrons undergoing betatron oscillations. This spectrum is then fit with the asymptotic form of the classical synchrotron function [147] to obtain an associated photon critical energy ($\hbar\omega_{\gamma,crit}$) value. In the sections that follow, we investigate how these electron acceleration, and associated photon emission characteristics change, as several different laser and plasma parameters are scaled. Section 7.3 studies the effect of varying the parameter ω_l/ω_p. The effect of varying ω_l and ω_p are considered separately. The scalings obtained are then compared to the expected scalings from 1D wakefield theory for the electron acceleration, and synchrotron radiation theory as presented in Ref. [7] for the photon emission. Section 7.4 studies the effect of varying the laser intensity parameter (a_0). In this section two different mechanisms for electron acceleration and subsequent radiation are studied. First, the betatron mechanism is studied, and second, the ponderomotive mechanism. The betatron electron acceleration and photon emission scaling investigations are carried out analogously to Sec. 7.3. However, for the ponderomotive mechanism, since the electrons experiencing acceleration are located in the region of the simulation window containing the laser field, only electrons and photons from this region are analyzed. Electron acceleration is analyzed in the exact same way as the case of the self-injected electrons by tracking $\varepsilon_{e,max}$. In contrast to the analysis of high energy photon emission due to the betatron mechanism, in the ponderomotive analysis the photon spectrum is fit to a power law to obtain a cut-off value ($\hbar\omega_{\gamma,cut-off}$). Scaling of these values representing electron acceleration and photon emission for the ponderomotive mechanism are then reported. Finally, in Sec. 7.5 we conclude and provide some possible implications in various applications.

7.2 Methods

7.2.1 Overview of PIC code with radiative processes

EPOCH is a code with the standard relativistic electromagnetic (1D-3D) Particle-in-Cell (PIC) algorithm [148], which is also equipped with various options for radiative processes that are well beyond a standard PIC code. These include both quantum and classical radiative processes. Specifically, subroutines capable of simulating quantum-corrected synchrotron radiation (in addition to radiation reaction and pair production) are included in EPOCH [149, 150, 151, 122]. In this paper the synchrotron radiation functionality is solely used, leaving the pair production and radiation reaction modules turned off, as these appear to be of secondary importance, which will be discussed later. In our investigations we find that radiation reaction effects remain minor compared to the main effects. We caution ourselves, however, that the finite difference field solver in space creates numerical inaccuracies in extreme high energy regimes.

7.2.2 The base case of LWFA

In the current study we employ the use of EPOCH 2D with a second-order field solver to investigate several different properties of LWFA of self-injected electrons and their betatron radiation signature. In our base case the following parameters in Table 7.1 are used to determine all physical properties of the system.

Laser Intensity	a_0	5
Frequency Ratio	ω_l/ω_p	10
Density	n_e	$10^{24}\mathrm{m}^{-3}$
Aspect Ratio	$w_0/(\lambda_p\sqrt{a_0})$	$1/\pi$

Table 7.1: Summary of the laser and plasma parameters for our base case.

The wakefield is driven in a fully ionized hydrogen plasma by a laser pulse with a supergaussian profile ($f(x) \propto \exp\big[-((x-x_0)/\sqrt{2}\sigma)^8\big]$) in length and width polarized in $\hat{z}$ dimension. The Full-Width at Half-Max (FWHM) length is chosen based on the wakefield relativistic resonant condition of the background plasma ($\tau_l = \lambda_p\sqrt{a_0}/(2c)$) and the FWHM width is chosen based on matching the waist of the laser pulse to the plasma bubble radius ($w_0 = \lambda_p\sqrt{a_0}/\pi$).[7, 102] Here $\lambda_p = 2\pi c/\omega_p$ is the plasma wavelength, where ω_p is the plasma frequency.

7.2.3 Electron acceleration

The wake is excited behind the laser pulse, forming a void of electrons (ie. bubble). The extent to which these electrons are displaced is characterized by the bubble radius and is

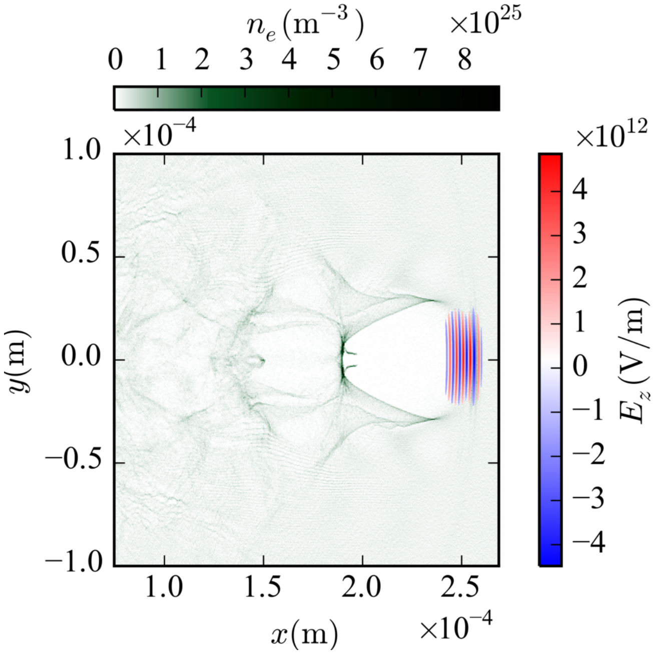

Figure 7.1: The laser wakefield structure in our base case. Plasma density structure is shown (dark green ranging up to $\sim 9 \times 10^{25}\mathrm{m}^{-3}$) behind the laser pulse (electric field ranging to $\sim \pm 5 \times 10^{12}$V/m) which is linearly polarized in $\hat{z}$. Electron acceleration and photon emission data are collected from the region of the primary ion cavity containing self-injected electrons in the betatron investigation and from the laser field and its leading edge in the ponderomotive investigation.

a result of the balance of space charge of the background species and the ponderomotive potential of the laser as discussed in more detail by Ref. [102]. Electrons can become trapped in the rear of the bubble and experience a longitudinal accelerating field due to the structure of the wakefield electric field. This acceleration continues until the electrons overtake this accelerating region (dephase), or until the laser pulse weakens to the point at which it can no longer support the bubble (pump depletion). The onset of either of these phenomena is sufficient for longitudinal electron acceleration to cease. At this point the trapped electrons are understood to have reached energy saturation, as seen in Fig. 7.2 (c). The maximum electron energy saturation, $\varepsilon_{e,max}$ is utilized as a diagnostic to describe the accelerating potential of the wakefield created by the laser pulse. More importantly, however, the snapshot at which maximum electron energy saturates is used to bound all runs. After this saturation occurs the photon radiation begins to become weaker and nonlinear factors begin to dominate.

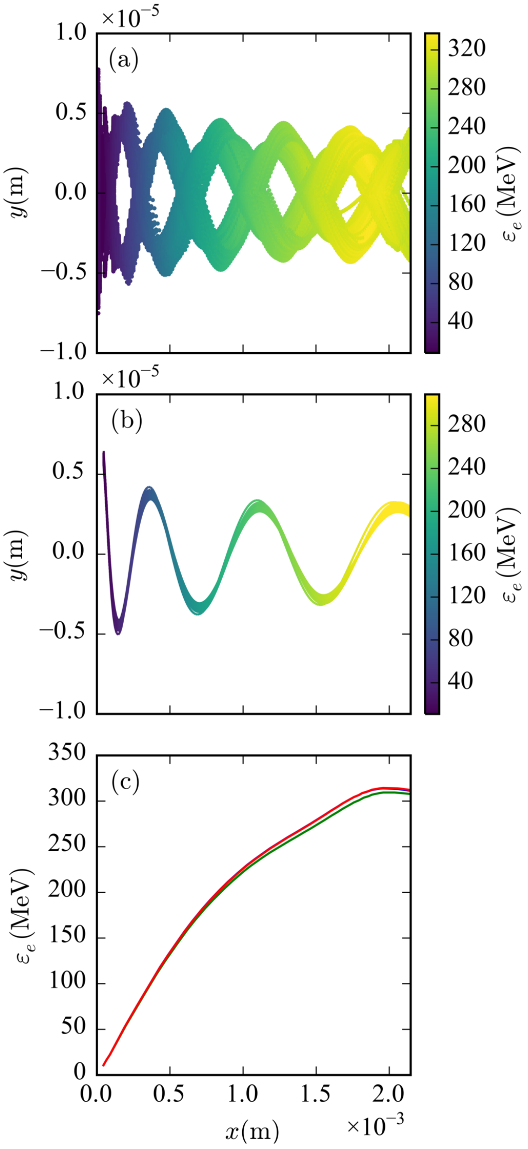

Figure 7.2: Electron energy increase as a function of propagation distance (x). (a) The location and energy of the top 5% highest energy electrons within each snapshot. (b) The trajectory and energy evolution of a subset of 50 particles which end the simulation with the top 5% highest energy [6, 7]. (c) The energy evolution and subsequent energy saturation of electrons randomly selected from the subset plotted in (b). Transverse motion (y) is shown in (a) and (b) as they are related to the betatron radiation mechanism.

Electron trapping in the current study is a result of the transverse self-focusing of initially trapped off-axis electrons, which results in electrons being injected into the accelerating region of the wakefield. As seen in Fig. 7.1, at high laser intensities ($a_0 \gtrsim 4-5$) these off-axis electrons are injected with transverse momentum. These self-injected electrons in the ion cavity execute transverse (betatron) oscillations ($\hat{y}$) induced by the structure of the travelling wakefield's transverse electric potential, as seen in Fig. 7.2 (a),(b).

7.2.4 Photon emission and betatron analysis

The betatron motion seen in Fig. 7.2, executed by self-injected electrons, produces synchrotron emission in a narrow cone of $\Delta\theta$ and sweeps out an angle of ψ with respect to the $\hat{x}$-direction [7]. All investigations are carried out in the wiggler regime, which is defined as the regime in which the undulator strength parameter $K > 1$, where K is defined [7] as

$$K = 1.33 \times 10^{-10} \sqrt{(\gamma_e n_e[\mathrm{cm}^{-3}])}\, r_\beta[\mu\mathrm{m}], \tag{7.1}$$

where γ_e is the electron lorentz factor, n_e is the background plasma density, and r_β is the amplitude of the betatron oscillation. In this regime $\psi > \Delta\theta$ the photon emission spectrum (synchrotron spectrum) is characterized classically by a series of harmonics up to a critical frequency $\omega_{\gamma,crit}$. It is important to note in the wakefield case the trapped electrons are subject to a longitudinal acceleration, which means γ_e is not a constant but a function of time. As mentioned in Ref. [7], for the purposes of obtaining scaling laws we can sidestep this complication by fitting to the high energy tail of the photon spectrum.

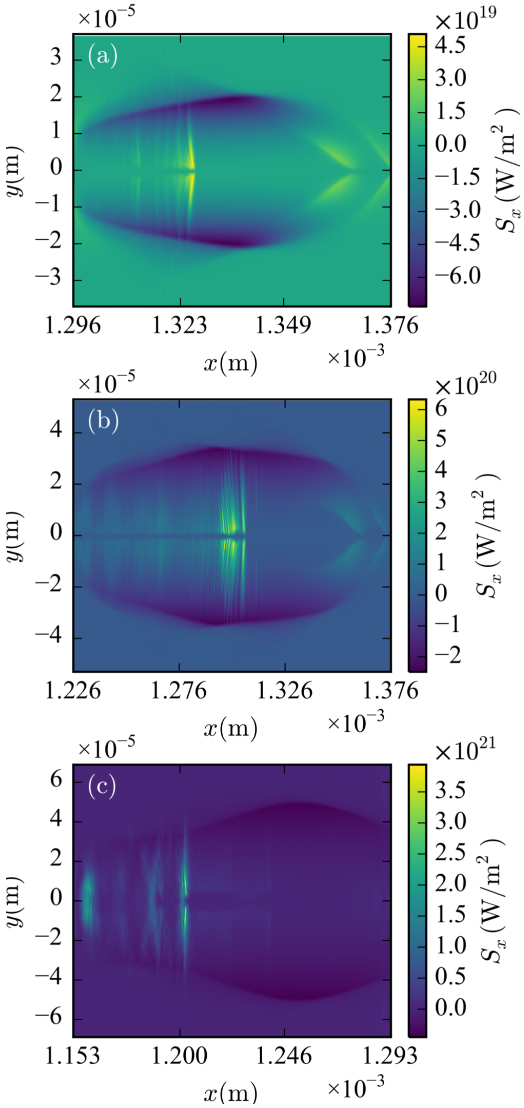

Figure 7.3: Induced radiation intensity as shown through the brightness of the emitted Poynting vector (S_x in the $\hat{x}$ direction) for electron beam driven ((a) and (b)), and laser driven WFA (c). The gaussian electron beam, located from $\sim 1.35 \times 10^{-3}$m to the leading edge of the window, has $E_b = 500$MeV, and $r_x = r_y = 25\mu$m, with $n_b/n_p = 0.5$ (a), and $n_b/n_p = 1$ (b). The laser (c) is $\hat{z}$-polarized with a supergaussian (exponent 8) profile with $a_0 = 10$, and a slightly larger spot size than (a), and (b). The laser field is omitted to fully visualize the Poynting vector originating from the self-injection. r is the full-width at half max, and the subscripts b and p denote beam and plasma respectively.

This then defines a critical photon energy characteristic of photon emission from electrons at maximum energy saturation, as seen in Fig. 7.2 (c) given by the equation below [152, 7]

$$\hbar\omega_{\gamma,crit}[\text{eV}] = 5.24 \times 10^{-21}\gamma_e^2 n_e[\text{cm}^{-3}] r_\beta[\mu\text{m}]. \tag{7.2}$$

The spatial structure of the intensity of the wakefield as measured by the Poynting vector ($1/\mu_0 E_y \times B_z$) driven by the electron bunch or by the laser pulse is shown in Fig. 7.3. In the electron bunch driven wakefield we observe a coherent oscillatory structure (fish-bone like structure) in the tail part of the wakefield bubble. These oscillations are reflective of the injected electron betatron oscillations in each case of Fig. 7.3(a), (b), and (c). The arrow-like structure that appears at the front of the wakefield coincides with the driver electron bunch modulation (Fig. 7.3 (a), and (b)). Although the base case laser intensity ($a_0 = 5$) also has similar phenomenology, a laser intensity of $a_0 = 10$ is used here to highlight the structure of radiation in the primary ion cavity.

By time integrating photon counts in a small region of the simulation window containing self-injected electrons executing betatron oscillations we are able to construct a spectral profile of the photon emission, as seen in Fig. 7.4. (In Figs. 7.4-7.9 shown are all laser-driven wakefield properties.) Though there is a high population of low energy photons due to radiation from lower energy (background) electrons throughout the simulation, we are able to fit the tail of the spectrum with the asymptotic classical synchrotron profile ($f(\xi) = 0.777\sqrt{\xi}\exp\big[-\xi\big]$) [147] to obtain the critical energy as a fit parameter.

In the following sections we investigate how electron maximum energy saturation and photon critical energy change as the base case parameters are scaled. These scaling investigations will give us insight, on one hand, in the direction of astrophysical regimes, where a_0 is very large and ω_l/ω_p increases as a wakefield structure would propagate along the jet, and on the other hand in the direction of the high density (solid) regimes appropriate for X-ray wakefields.

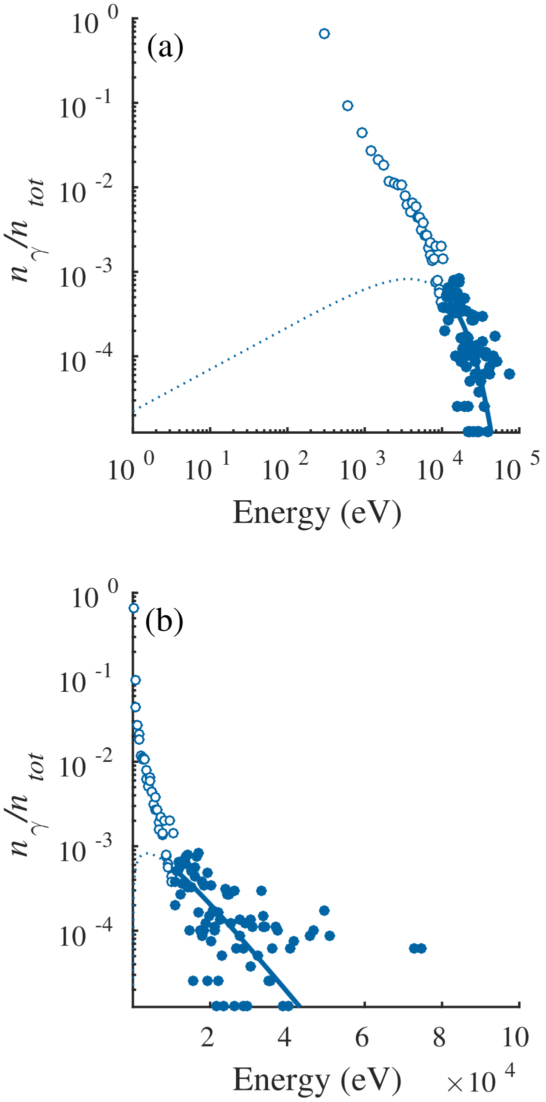

Figure 7.4: Normalized number of photons (n_γ / n_{tot}) emitted from the wakefield as a function of photon energy (photon spectrum), shown in log-log (a) and semi-log (b) plots. The spectrum was taken from the region containing self-injected electrons, integrated over time, and normalized by the total number of photons. The high energy tail of the spectrum was fit to the asymptotic synchrotron function with a least squares algorithm. Bold lines and filled data points represent the region where the fitting took place, whereas dotted lines and empty data points represent regions omitted from the fitting algorithhm.

7.3 Frequency scaling of electron and photon energies

7.3.1 Betatron investigation

Electron maximum energy saturation $\varepsilon_{e,max}$ and photon critical energy $\hbar\omega_{\gamma,crit}$ values are obtained by the methods described in Sec. 3 at several values of the frequency ratio (ω_l/ω_p) to observe scalings. The frequency ratio is investigated in two different ways. First by changing the plasma frequency (ω_{l0}/ω_p) and second by changing the laser frequency (ω_l/ω_{p0}). As seen in Fig. 7.5 (a), the electron maximum energy saturation scales less than quadratic (as expected from 1D theory) at $\varepsilon_{e,max} \propto (\omega_{l0}/\omega_p)^{1.73}$.

Using this electron maximum energy scaling together with the photon critical energy scaling relationship from Eq. (7.2) and the fact that $\varepsilon_e \propto \gamma_e$, the scaling of the photon critical energy from these electrons at maximum energy saturation can be estimated as $\hbar\omega_{\gamma,crit} \propto \varepsilon_{e,max}^2 n_e r_\beta$, as suggested in Ref. [7]. Further, assuming r_β scales the same as the bubble radius $(r_b = 2\sqrt{a_0}/k_p \propto \omega_p^{-1})$[102, 7], the expected plasma frequency scaling is $\hbar\omega_{\gamma,crit} \propto (\omega_{l0}/\omega_p)^{2.46}$. As shown above in Fig. 7.5 (b), the photon critical energy scales as $\hbar\omega_{\gamma,crit} \propto (\omega_{l0}/\omega_p)^{2.05}$. The difference between the simulation observed value and this simple estimate may arise from inherent limitations on accuracy associated with the fitting method, and more significantly, from the fact that the plasma frequency scaling of r_β is not precisely known.

When examining the laser frequency scaling, it is shown in Fig. 7.6 (a) that the electron maximum energy saturation again scales slightly less than expected from 1D theory $\varepsilon_{e,max} \propto (\omega_l/\omega_{p0})^{1.74}$. This nearly identical result is expected from wakefield theory, since the electron maximum energy saturation is known to depend on the ratio ω_l/ω_p. The

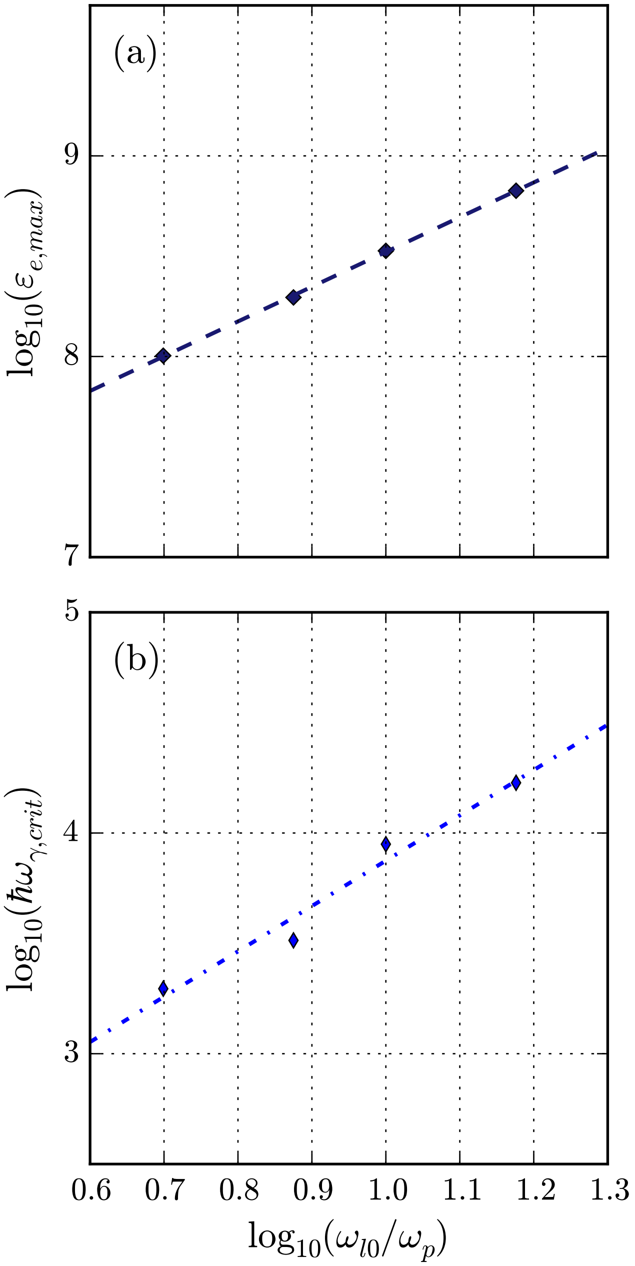

Figure 7.5: Scaling relationship of the self-injected electron energy and emitted photon energy as a function of ω_{l0}/ω_p. (a) shows the electron maximum energy saturation scaling, and (b) shows the photon critical energy scaling.

photon critical energy, however, scales differently depending on how the ratio is altered. Shown in Fig. 7.6 (b), the photon critical energy scales as $\hbar\omega_{\gamma,crit} \propto (\omega_{l0}/\omega_p)^{2.69}$.

Assuming again $r_\beta \propto r_b$, the betatron amplitude r_β should be constant when scanning the laser frequency, since the plasma frequency and laser intensity are held constant. This logic leads to an expected scaling of $\hbar\omega_{\gamma,crit} \propto (\omega_l/\omega_{p0})^{3.48}$. This overestimate is expected noting two important considerations. As laser frequency is increased, so is the dephasing time, and as electrons execute betatron oscillations, r_β becomes smaller (See Fig. 7.2 (a),(b)). Therefore, as (ω_l/ω_{p0}) increases, r_β of electrons at the latest times (highest energies) decreases. It is again noted here that the scaling relationships are defined by the high-energy tail of the spectra, which are achieved near the dephasing time. This means that as (ω_l/ω_{p0}) increases, r_β decreases, leading to a potential for the overestimate.

It is interesting to note that betatron photon energy scales more strongly with laser frequency than the inverse of plasma frequency. This means that the usage of the new frequency upconversion technique (such as in Ref. [23]) should be able to take advantage of this scaling by increasing the ratio ω_l/ω_p through an increase in ω_l, an alternative path to the decrease of ω_p.

7.4 Intensity scaling of electron and photon energies

7.4.1 Betatron investigation

Laser intensity (a_0) scalings of electron maximum energy saturation ($\varepsilon_{e,max}$) and photon critical energy ($\hbar\omega_{\gamma,crit}$) by the methods described in Sec. 3 are investigated and plotted below in Fig. 7.7. The photon critical energy is found to scale as $\hbar\omega_{\gamma,crit} \propto a_0^{3.81}$. The scaling relationship taken from Eq. (7.2) ($\hbar\omega_{\gamma,crit} \propto \varepsilon_{e,max}^2 n_e r_\beta$) taken together again with simulation results from electron maximum energy saturation are used to motivate an expected photon critical energy scaling. The maximum electron energy saturation scaling seen in Fig. 7.7 (a) is found to be $\varepsilon_{e,max} \propto a_0^{1.54}$. With this result, and assuming that r_β scales as bubble radius ($r_b = 2\sqrt{a_0}/k_p \propto a_0^{0.5}$)[102, 7], the predicted photon critical energy scaling is $\hbar\omega_{\gamma,crit} \propto a_0^{3.58}$, which is slightly below the result obtained through the photon spectrum analysis. This deviation again likely originates from inherent limitations on accuracy associated with the fitting method, and more significantly, from the fact that the laser intensity scaling of r_β is not precisely known. It is also noted here that at $a_0 = 5$ in Fig. 7.7 (a) and (b) the electron maximum energy saturation and photon critical energy deviate from a linear scaling, which may indicate a regime change.

7.4.2 Ponderomotive investigation

In addition to inducing the wakefield, the ponderomotive force is itself responsible for electron acceleration and subsequent radiation [140, 146]. The ponderomotive potential of the laser driver longitudinally accelerates electrons to energy saturation, while interactions with the laser field itself cause said electrons to radiate longitudinally. The electrons and photons located from the leading edge of the simulation window including the extent of the laser field are examined in order to determine scaling laws. The maximum energy of electrons in this simulation window are recorded until saturation occurs. This saturation is then recorded for each run as in the previous sections and plotted below in Fig. 7.8 (a). The relationship between electron maximum energy saturation and laser intensity is found to be $\varepsilon_{e,max} \propto a_0^{1.42}$. This 2D result is lower than the nearly quadratic 1D result from Ref. [146], as expected due to higher dimensional effects.

Contrary to the photon spectrum analysis methods motivated by betatron radiation and outlined in Sec. 3, the ponderomotive analysis involved fitting the high energy tail of the photon spectrum with a power law to obtain a cut-off value. Seen in Fig. 7.8 (b), the relationship between photon cut-off energy and laser intensity is found to be $\hbar\omega_{\gamma,cut-off} \propto a_0^{2.26}$.

It is interesting to note that photon energy from the wakefield scales more strongly with laser intensity than photon emission from the laser region itself. This means that next generation laser facilities utilizing solid density plasma with x-rays may be in a unique position to explore such scaling of betatron photon emission from wakefields. It is also noted here, however, that there are expected to be QED effects such as radiation reaction and pair production that must be accounted for in order to motivate realistic expectations.

7.5 Discussion

In the current study we investigate scaling laws of LWFA processes and their associated high energy photon emission from wakefields. This investigation is carried out by simulating acceleration and emission of self-injected electrons trapped in the primary ion cavity of the wakefield as well as electrons accelerated by the field of the laser driver. Specifically we study the maximum electron energy saturation ($\varepsilon_{e,max}$) and the critical photon energy ($\hbar\omega_{\gamma,crit}$) as a function of the laser frequency (ω_l), plasma frequency (ω_p) (or equivalently the plasma density) as well as the normalized vector potential (a_0). The electron maximum energy saturation $\varepsilon_{e,max}$ is found by recording the maximum energy of electrons over time until that energy saturates. The photon critical energy $\hbar\omega_{\gamma,crit}$ is found by integrating photon counts over time from the self-injected electrons and the tail of the resultant spectrum is fit with the asymptotic classical synchrotron function to return $\hbar\omega_{\gamma,crit}$ as a fit parameter. The scaling of a series of these parameters are then compared to expected scaling based on theory from Ref. [152, 7] shown in Eq. (7.2). In addition to examining the scaling of electron acceleration and photon emission of self-injected wakefield electrons, we also investigate the scaling of these processes due to the laser driver itself through the ponderomotive mechanism.

The studies are carried out using a 2D electromagnetic PIC code (EPOCH) that includes radiative processes such as quantum corrected synchrotron radiation. This QED (quantum corrected) synchrotron module is used to generate all photon emission. The degree to which quantum effects intervene is determined by the parameter $\eta = \frac{e\hbar}{m_e^3 c^4}|F_{\mu\nu}p^{\nu}| = E_{RF}/E_S$, where E_{RF} is the electric field in the relativistic electron's rest frame and $E_S = 1.3 \times 10^{18}\text{V/m}$ is the Schwinger field [151, 122, 129]. At $\eta \ll 1$ the quantum synchrotron function reduces to the classical synchrotron function, but as $\eta \rightarrow 1$, the classical synchrotron function begins to deviate significantly from the quantum-corrected form, where QED effects begin to become important near $\eta \gtrsim 0.1$ [153, 122, 151]. Figure 7.9 shows the number of photons emitted with varied values of a_0 and η associated with the spectra of some of our highest energy runs. The η parameter is calculated using the critical photon energy fit parameter together with an approximation of the transverse wakefield strength. At each respective η value the quantum mechanical synchrotron function ($\text{F}[\eta, \chi]$)[153, 151], the classical synchrotron function ($f_{\text{synch}}[4\chi/3\eta^2]$)[153], and its asymptotic form are shown.

All simulations in this study have photon spectra with $\eta < 0.01$ and are, therefore, fit with the asymptotic form of the classical synchrotron function to obtain an approximation of the photon critical energy. EPOCH also has the ability to simulate radiation reaction and pair production. The radiation reaction functionality is tested on several different simulations with laser intensity in the range $a_0 = 5 - 20$. The effect of enabling radiation reaction proves to be inconsequential to the current study as expected, as there is no noticeable effect on the photon spectrum. Similarly the parameter $\chi = \frac{e\hbar^2}{2m_e^3 c^4}|F^{\mu\nu}k_{\nu}|$ determines the cross-section for pair production. It is noted in Ref. [153] that pair production becomes important for $\eta > 0.1$, where the most probable parametrized photon energy from synchrotron theory would be greater than $\chi_{mp} \approx 0.22\eta^2 = 2.2 \times 10^{-3}$.[154] In the $a_0 = 50$ case ($\eta = 0.0062$) $\chi_{mp} \approx 8.5 \times 10^{-6}$ and even in the sparsely populated high energy tail ($\hbar\omega \sim 600\text{MeV}$) $\chi_{\text{tail}} \sim 5.9 \times 10^{-4}$. Pair production is, therefore, disabled in our scaling investigations.

Through our study we find in general that the higher the density regime is, the more important the quantum mechanical radiative processes are. It has been seen that in high density plasmas when the ambient fields are strong [149] QED effects become non-negligible. Thus in X-ray LWFA, radiation characterized by quantum mechanical processes becomes dominant. In such cases, radiative effects[155, 156] may become important. Thus we find that radiation sources based on this X-ray LWFA may become an important topic of future investigations. On the other hand, the quantum mechanical radiative processes become nearly negligible in the lower density cases and in particular to our astrophysical acceleration processes [140]. In the diffuse astrophysical environment where the ambient fields are weak, we suspect that QED effects in the structures studied here in this particular sense to be negligible. We understand that if the electron energies become very high, quantum effects become important again.

As mentioned in Sec. 7.3 and Sec. 7.4, the scaling results may be reasonably interpretable from our understanding. Due to numerical limitations we stop short of extreme highly relativistic regimes, which may be of interest in the future laboratory experiments and in various astrophysical applications. We regard that although these scalings are useful guidance to see how plasma and laser parameters scale to determine the energies of electrons and resultant photons, these scalings are only a glimpse into regimes of far more nonlinear extreme parameters.

By investigating the electron acceleration and the resultant photon emission associated with an increase in various laser and plasma parameters, we have gained some insight into astrophysical regimes where these parameters such as a_0 and ω_l/ω_p are much too large to directly simulate with conventional PIC codes. We have investigated the scalings of these parameters arising from two processes of electron acceleration and subsequent radiation that could be present in astrophysical jets, namely LWFA and the ponderomotive acceleration (PA). PA is particularly relevant to astrophysical cases [140, 146] and is additionally of much import in the case of the radiation pressure acceleration (RPA) [157].

Natural generation of these radiating structures could be driven by episodic eruptions of accretion disks of Active Galactic Nuclei (AGN) and Blazars due to the Magneto-Rotational-Instability (MRI). Specifically, there are phenomena associated with episodic eruptions of the disk plasma due to the MRI (see Refs. [158, 159, 160]) that seem to be closely related to the episodic nature of gamma ray burst emissions [161, 162]. Such emissions may be related to those from AGN. These eruptions can give rise to the excitation of intense Alfvén waves which can then mode convert into electromagnetic pulses, which, we surmise, are related to the emission of bursts of gamma rays and extreme high energy cosmic ray (EHECR) genesis [140]. Therefore, if the scaling laws investigated here hold for higher parameter spaces, it could be interpreted that episodic high energy gamma ray photons received from blazars are in part due to radiation from the driver pulse and/or betatron radiation of electrons trapped in a plasma wakefield in Blazar jets.

The frequency ratio (ω_l/ω_p) scaling results are applicable to the astrophysical case, where the radio wave accelerating structure would be exposed to increasingly lower plasma densities as it propagates along the AGN jet. This makes the extremely powerful electromagnetic pulse (converted from the Alfvén wave) fit to make wakes behind it. The laser intensity (a_0) scaling results are again relevant to the astrophysical case, where the radio wave accelerating structure's a_0 is very large due to its long wavelength. It is noted here that when $a_0 \gg 1$ the ponderomotive mechanism for electron acceleration and subsequent radiation is understood to be the dominant mechanism due to the similarity of the electron and ion response to the driver[146].

Additionally a recent realization that X-ray (or γ-ray) radiation signatures are crucial elements in discerning the γ-ray signal from a possible heavy dark matter candidate from the core of our galaxy [163] makes it important to consider the wakefield mechanism in the surviving plasma in the core. As our galaxy is old compared to Blazars considered in Ref. [164] and Microquasars in Ref. [164] and thus the disk is largely stable, the main possible actions are confined to the core. It is still important to study the characteristics of the plasma instabilities present in the core of our galaxy, particularly near the central black hole ($\sim 10^6 M_\odot$). We should also investigate if and what processes can excite strong waves whose phase velocities exceed sufficiently that of the bulk motion such as its thermal velocity so that these motions are amenable for inducing wakefields [165]. If so, these wakefields may constitute additional sources of X-rays and γ-rays coming out of the galactic core. Finally, when one tries to compare the γ-ray spectrum observed from astrophysical objects with the theoretical model for the electron energies based on LWFA, as commented in Refs. [141, 135], and [140], the wakefield needs to be allowed to dephase, which introduces the phase stochasticity. In the present work we have not touched on this subject. If we include this effect as shown in Refs. [141, 135, 140, 164], the spectrum of electrons (and thus impacting the γ-ray spectrum), gets a general power spectrum of negative 2 (in an ideal 1D geometry and greater than 2 in higher dimensional cases). Such a comparison work should be interesting and is left for a future investigation.

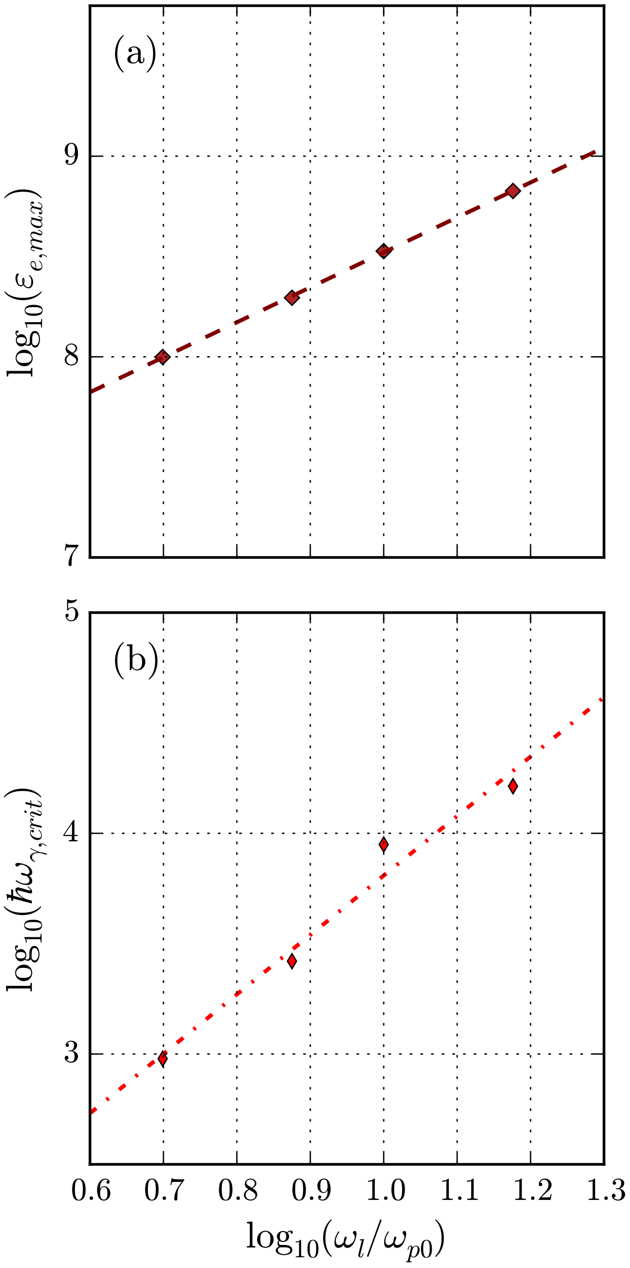

Figure 7.6: Scaling relationship of the self-injected electron energy and emitted photon energy as a function of ω_l/ω_{p0}. (a) shows the electron maximum energy saturation scaling, and (b) shows the photon critical energy scaling.

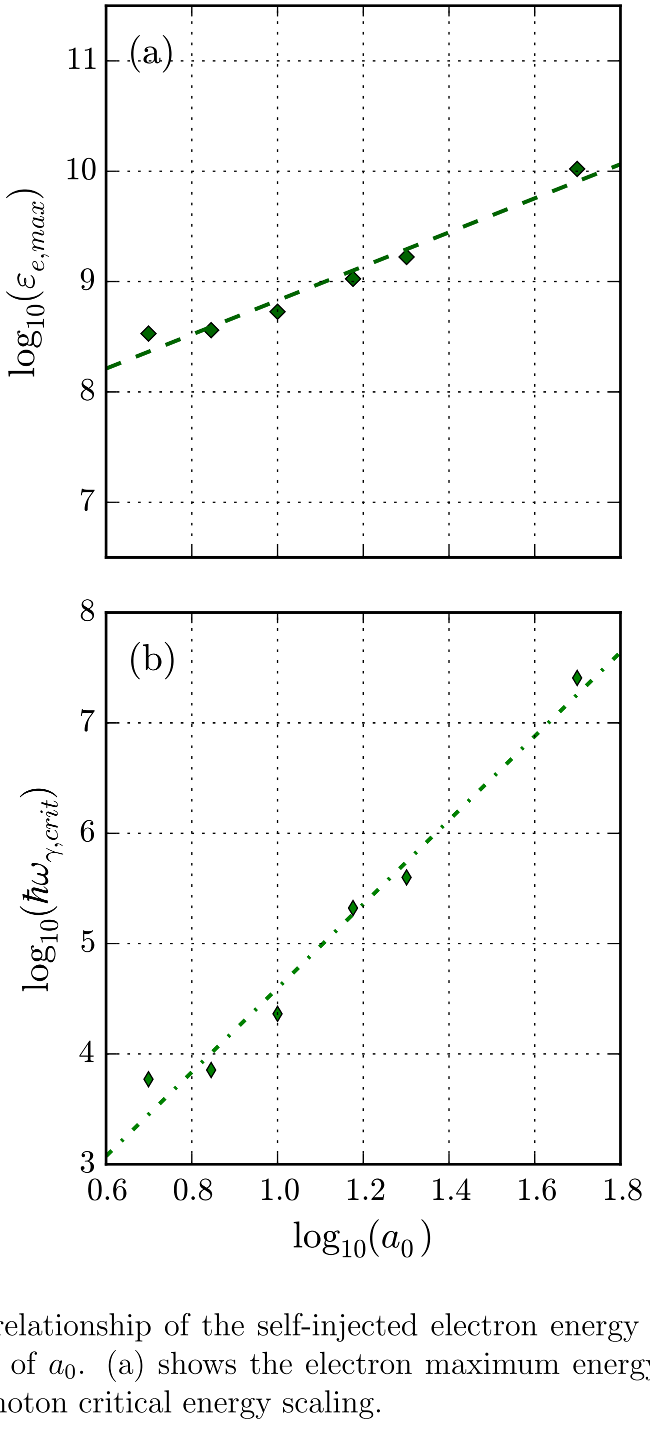

Figure 7.7: Scaling relationship of the self-injected electron energy and emitted photon energy as a function of a_0. (a) shows the electron maximum energy saturation scaling, and (b) shows the photon critical energy scaling.

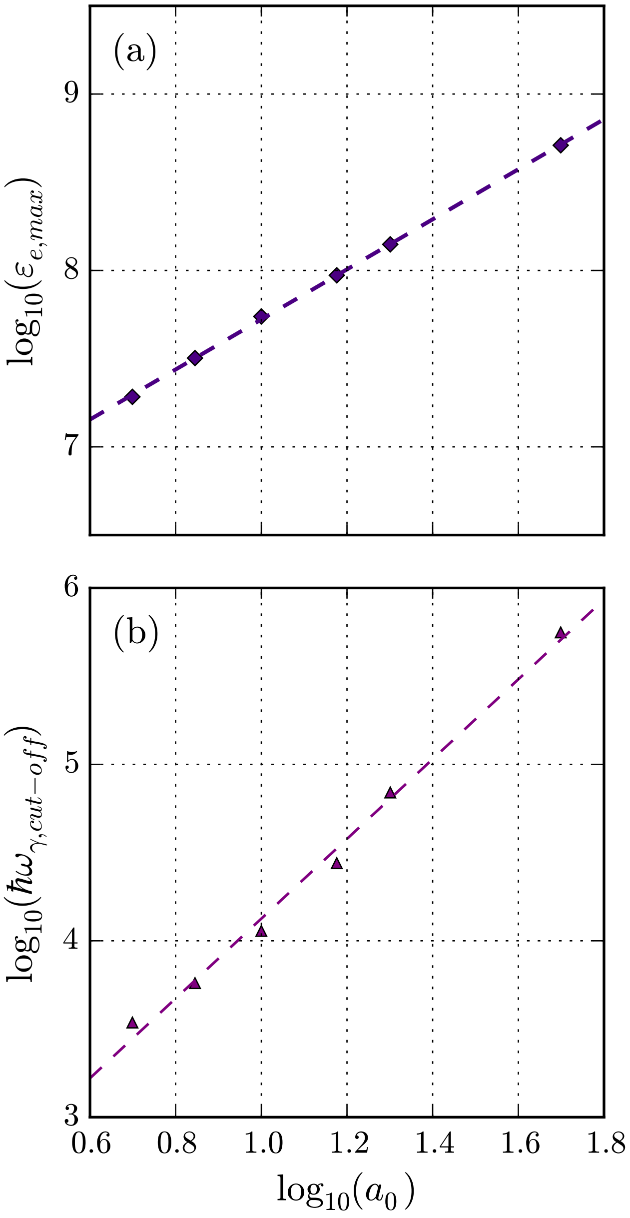

Figure 7.8: Scaling relationship of electron energy and emitted photon energy of electrons in the simulation window as a function of a_0. (a) shows the electron maximum energy saturation scaling, and (b) shows the photon cut-off energy scaling.

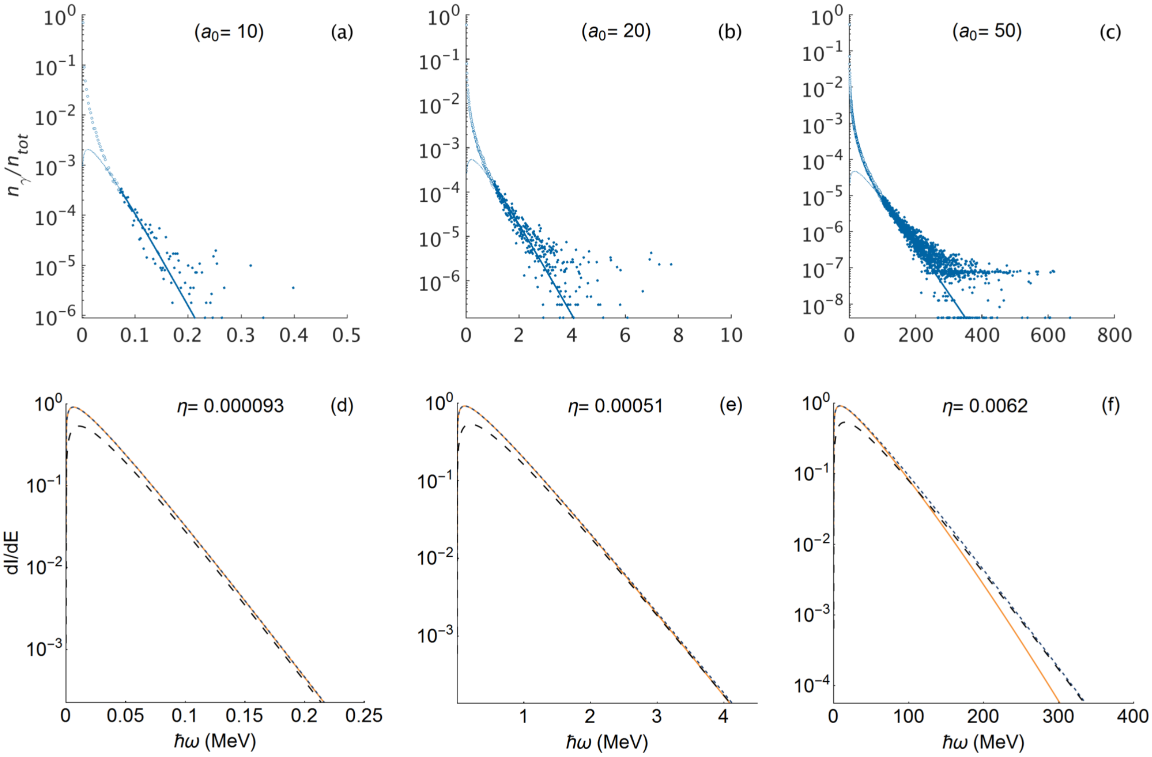

Figure 7.9: Normalized number of photons emitted from the wakefield (n_γ/n_{tot}) as a function of photon energy (photon spectrum) driven by lasers with $a_0 = 10$ (a), $a_0 = 20$ (b), and $a_0 = 50$ (c). The theoretical quantum mechanical (F$[\eta, \chi]$ - solid), classical ($f_{\text{synch}}[4\chi/3\eta^2]$ - short dashed) and the classical asymptotic (long dashed) synchrotron radiation intensity (dI/dE), normalized to the photon emission as a function of photon energy is shown in (d), (e), and (f) respectively. The η value associated with each asymptotic fit can be seen directly below each respective simulated spectrum. The critical photon energy in conjunction with the approximate transverse wakefield strength for each case was used to calculate η.

Chapter 8

TW/cm^2 Pulse measurement by fused silica wafers

This section presents a novel pulse measurement technique for measuring high intensity (~ 1 TW/cm^2) laser pulses on a shot to shot basis through self-phase modulation in thin (~ 1 mm) fused silica wafers. After briefly reviewing some theoretical background, a short explanation of the technique will be presented and an example pulse measurement will be shown and verified by a pulse duration measurement retrieved by scanning SHG FROG. Finally, it will be shown that *at least* quadratic phase information is contained in the SPM spectrum and therefore in addition to a pulse measurement, SPM can also provide insight in to the chirp present in an ultrashort laser pulse.

8.1 Background

The nonlinear Schrödinger equation was developed in the context of fiber optics to model pulse propagation [42] in optical fibers.

$$i\frac{\partial A}{\partial z} = -i\frac{\alpha}{2}A + \frac{\beta_2}{2}\frac{\partial^2 A}{\partial t^2} - \gamma|A|^2 A \tag{8.1}$$

Here A is the slowly varying amplitude of the pulse envelope. The first three terms on the right correspond to power loss (absorption), dispersion, and the nonlinear phase shift due to the change in nonlinear index respectively. In transparent dielectrics like fused silica the absorption coefficient of near optical wavelengths is very low as evidenced by its transparent nature. Transmitted power measurements of 0.945mJ 35 fs 800 nm (~ 1.3 TW/cm^2) laser pulses confirm a transmission of $\sim 99\%$ energy throughput when the wafer is oriented at Brewster's angle, therefore this term is neglected in Eq. 8.4. Furthermore, the effect of dispersion on ultrashort laser pulses of $\sim$ 35 fs duration in 1mm of fused silica is negligible. For example, the change in pulse duration of a transform limited 35 fs laser pulse due to dispersion after transmission through 1 mm of fused silica is $\sim$ 0.1 fs. This means that its peak intensity is very nearly constant during propagation. Though the technique can be performed with less intense pulses, the pulse must experience a significant nonlinear phase shift ($B \sim 2$) without experiencing significant dispersion. Where B in practical units for fused silica can be seen below in Eq. 8.2

$$B = 1.57 \times \frac{I_0[\frac{\mathrm{TW}}{\mathrm{cm}^2}]z[\mathrm{mm}]}{\lambda_0[\mu\mathrm{m}]} \tag{8.2}$$

Here I_0 is the peak intensity, z is the thickness of the fused silica wafer, and λ_0 is the central wavelength of the pulse. If these conditions are met, the only relevant term in Eq. 8.4 is the term pertaining to the nonlinear phase shift. In this case the pulse envelope does not change at all (~ 0.1 fs in this particular case), but the propagation of the pulse through the wafer satisfies

$$\frac{\partial A}{\partial z} = i\gamma|A|^2 A \tag{8.3}$$

which has the solution

$$A(z,t) = A(0,t)e^{i\gamma|A(t)|^2 z} \tag{8.4}$$

Therefore after passing through a material with a length L the pulse acquires a nonlinear phase shift $\Delta\phi(t)_{\mathrm{NL}} = \gamma|A(t)|^2 L$, where $\gamma = 2\pi n_2/\lambda_0 A_{\mathrm{eff}}$. Here A_{eff} is the effective mode area of a fiber and λ_0 and n_2 are the central wavelength and nonlinear index of refraction respectively. Or equivalently as described in Chap. 2, $\Delta\phi(t)_{\mathrm{NL}} = \frac{2\pi}{\lambda_0} n_2 I(t) z$. This nonlinear phase shift results in a change in the instantaneous frequency of the laser pulse since $\omega(t)_{\mathrm{inst}} \equiv d\phi(t)/dt$, where

$$\Delta\omega(t)_{\mathrm{inst}} = \frac{2\pi}{\lambda_0} n_2 \frac{dI(t)}{dt} z. \tag{8.5}$$

Therefore the maximum change in instantaneous frequency (and therefore spectral broadening) will be proportional to the actual pulse duration by

$$\Delta\omega_{\max} \propto \frac{2\pi}{\lambda_0} n_2 \frac{F_0}{\tau_0^2} L, \tag{8.6}$$

where F_0 is the peak fluence, and τ_0 is the fwhm pulse duration. Since λ_0, n_2, F_0, and L are easily obtained experimentally, if one could obtain a measurement of $\Delta\omega_{\max}$, the determination of the actual pulse duration τ_0 would collapse into simple algebra. However since $\Delta\omega_{\text{max}}$ does not seem to line up nicely with any obvious spectral features that I have been able to identify yet (ie. bimodal peaks, 1/e, fwhm, 1/e^2 etc.), in the next section I investigate the spectral broadening associated with various nonlinear phase shifts and compare simulated to experimental broadened spectrum to obtain a holistic (at this point) pulse measurement.

8.2 Application

The pulse to be temporally measured has $F_0 = 43.95$ mJ/cm^3 and, $\lambda_0 = 787$ nm and is transmitted through a thin film of fused silica with $n_2 = 2.5 \times 10^{-16}$ cm^2/W and $L = 1.2$ mm (when accounting for refraction at Brewster's angle). An unchirped temporal shape of *sech*^{2} is chosen to model the broadening with an initial guess for τ_0. The constants listed above are used in Eq. 8.7 that then determines the laser electric field with nonlinear phase shift

$$E(t) \propto \sqrt{I_0} Sech(1.76\frac{t}{\tau_0}) e^{i(\omega_0 t - \phi(t)_{NL} L)} \tag{8.7}$$

where $I(t)$ in the nonlinear phase shift is defined by

$$I(t) = I_0 Sech^2(1.76\frac{t}{\tau_0}). \tag{8.8}$$

After the nonlinear phase shift without a change in pulse envelope, the spectrum is broadened as discussed in Chap. 2. This can be seen by taking the Fourier transform of the laser field with the nonlinear phase shift (ie. the Fourier transform of Eq. 8.7).

A pulse duration scan is carried out in the range 30 - 45 fs in steps of 1 fs while holding all other values constant (ie. F_0, λ_0, n_2, L). The resultant broadened simulated spectrum (blue) is then overlapped with the experimentally obtained spectrum (red) is shown in Fig. 8.1 to look for agreement.

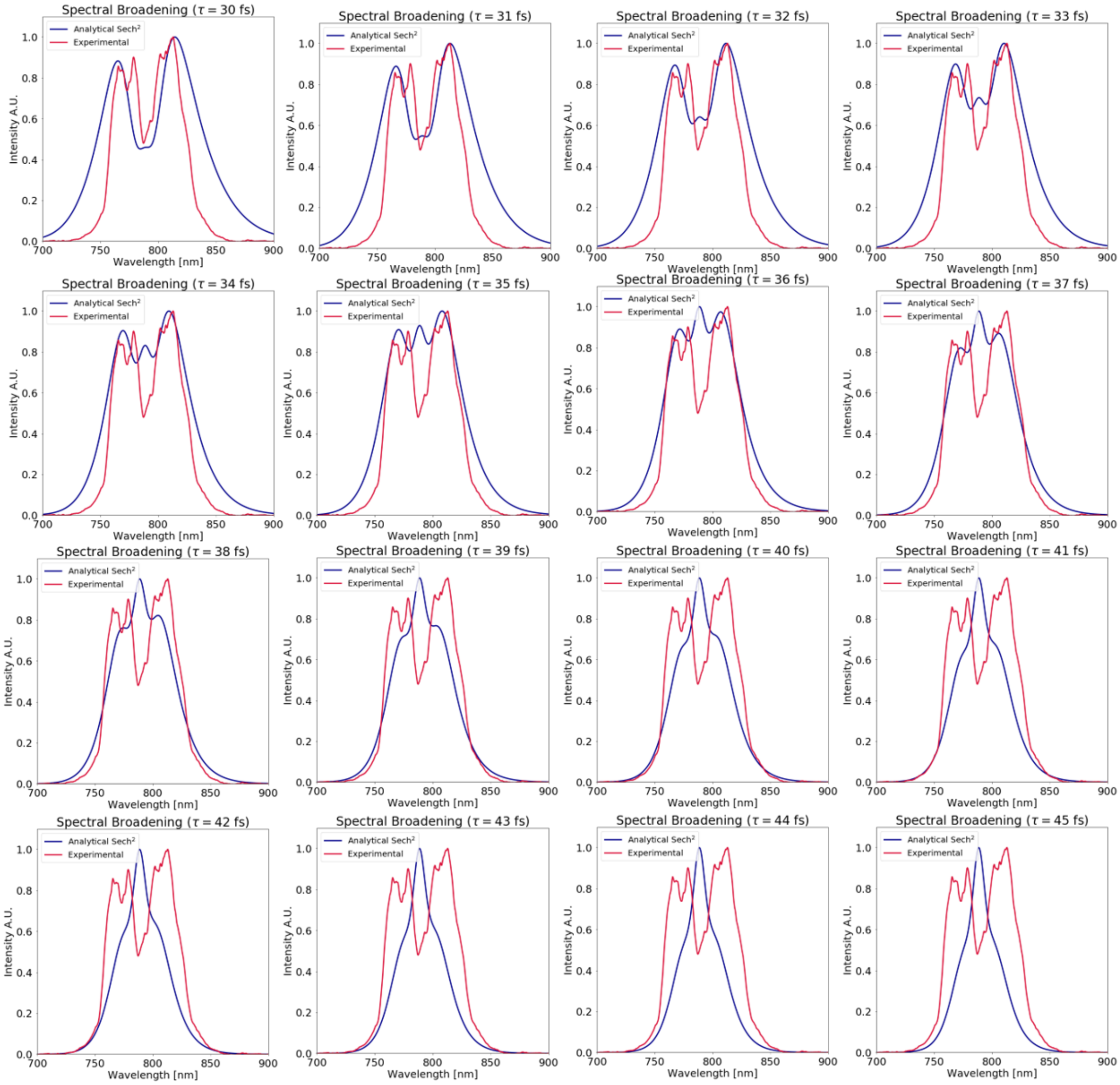

Figure 8.1: Shown above is the result of scanning the analytical pulse duration and comparing the resultant broadening (blue) to the measured experimental broadening (red) due to SPM

The difference between the experimental and simulated broadened spectrum is minimized for $\tau = 37$ fs. However, since there are discrepancies in the bimodal shape and the tails between the experimental and simulated spectrum in each of the spectral comparisons, error bars will need to encompass each of these scenarios. For example, if the tails are the critical feature that needs to be matched, pulses of up to 40 fs could be predicted by this method. Alternatively, if the overlap of the center of the peaks of the bimodal structure is most important, pulses down to 34 fs could be predicted. Whereas under no circumstances could spectral comparisons near 30 fs or 45 fs be considered good fits to the data. Therefore this method (in its infancy) predicts that this spectrum was generated by a 37± 3 fs laser pulse.

It is noted here that the experimentally measured bimodal structure will be produced by SPM only if the second order phase is minimized and the higher order phase terms are small (the closer to zero phase the laser pulse has, the better the prediction of this simple measurement). This interesting fact is explored very briefly in the next section. To validate this pulse measurement technique with experimental data, we compare to a pulse measurement by scanning SHG FROG. As described in Chap. 3 this technique is completely different than the method being explored in this chapter. Scanning SHG FROG uses the laser pulse to interfere with itself in a nonlinear crystal and spectrally resolve the intensity autocorrelation as the pulse is delayed with respect to a cloned reference pulse. The measured spectrogram and intensity autocorrelation can be seen in Fig. 8.2.

The pulse length as determined by intensity autocorrelation (vertically binned spectrogram) is measured to be $\sim$ 35.5 fs. Similarly, as seen below in Fig. 8.3 the pulse duration determined by phase retrieval was found to be $\sim$ 35.6 fs. Additionally, as expected due to its bimodal spectral broadening this pulse is seen to have very flat phase inside its fwhm pulse duration.

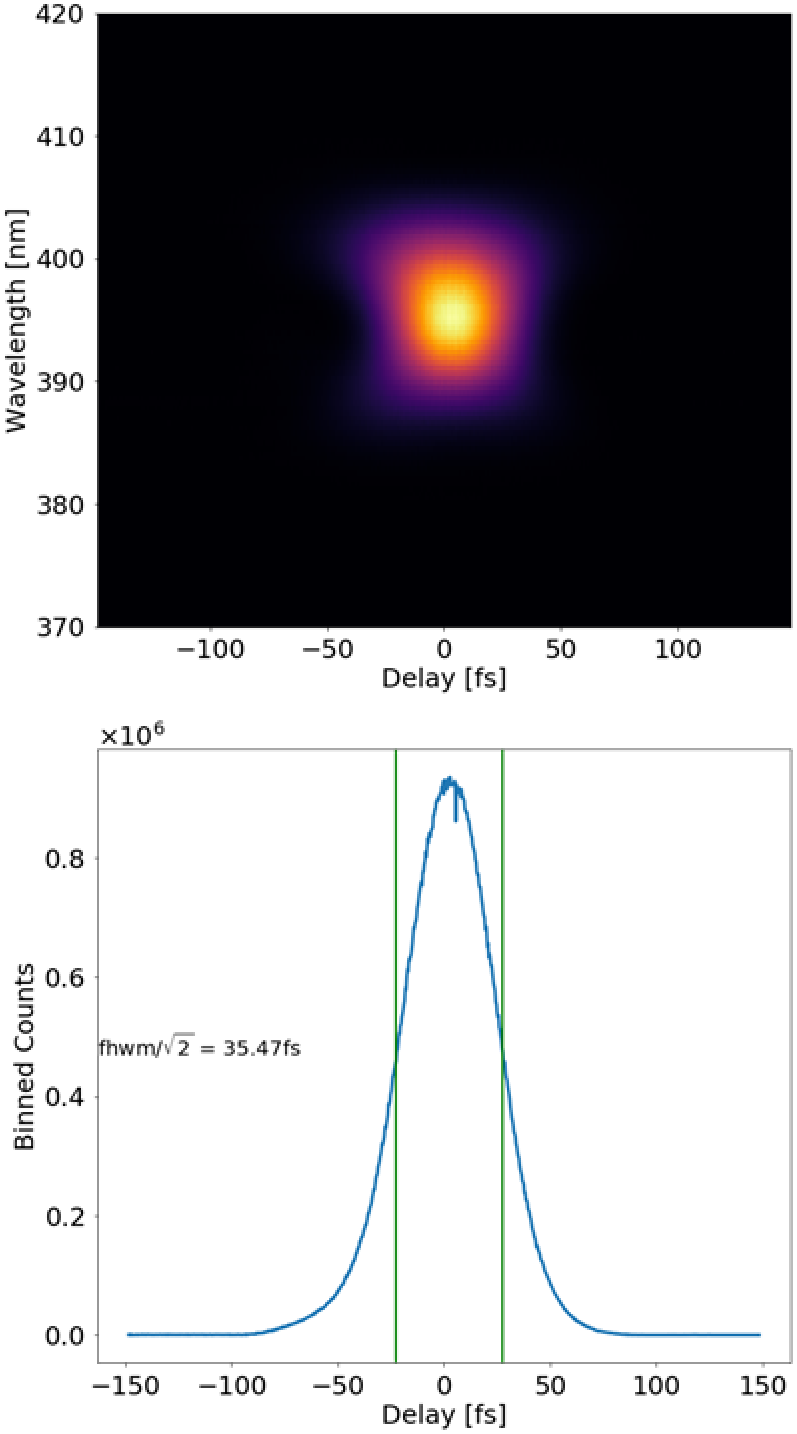

Figure 8.2: The measured spectrogram (top) and intensity autocorrelation (bottom) of the laser pulse.

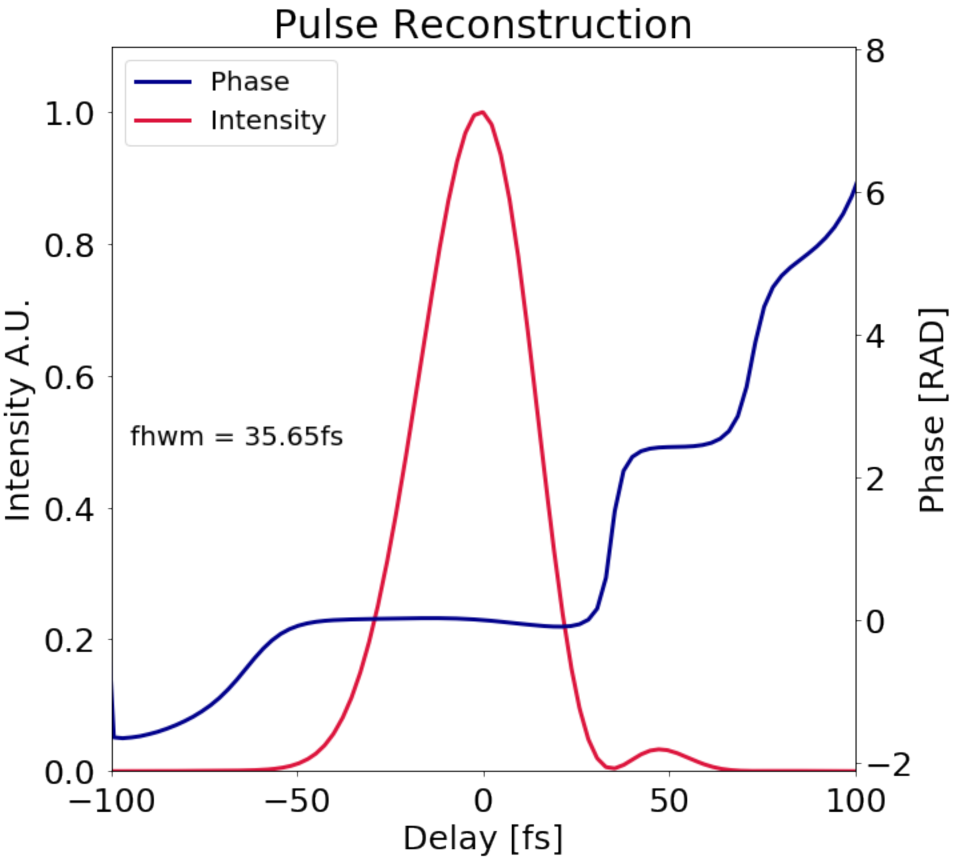

Figure 8.3: The pulse duration determined through phase retrieval of the SHG FROG trace. The intensity profile (red) and phase (blue) of the pulse determined through phase retrieval of the SHG FROG trace

Based empirically on these experimental findings, the centers of the bimodal peaks may be a more critical factor to match as opposed to the tails of the experimental spectrum in order to accurately predict the pulse length of intense unchirped laser pulses by the method presented in this chapter. For example, in Fig. 8.1 the center of the bimodal peaks in the experimental and simulated spectrum line up best somewhere between $\tau = 35$ and $\tau = 36$. Where the short wavelength peak just begins to poorly match at $\tau = 34$ and the long wavelength peak begins to poorly match at $\tau = 37$. If this is the case, this method could predict pulse durations nearly as accurately as the SHG FROG.

It is worth re-iterating that this method is much cheaper and requires vastly less infrastructure than a scanning SHG FROG (ie. no specially cut/grown nonlinear crsytals, motorized stages, LabVIEW programs etc.). Furthermore, this method is not restricted to the 800 nm wavelength, can be used in pulses below the duration limited by most BBO crystals (due to low conversion efficiency), and can be used as a single-shot diagnostic. Furthermore, if more experiments can empirically verify that matching bimodal peaks accurately predicts pulse duration down to 1 fs resolution for unchirped ~ 1 TW/cm^2 pulses, this method could reproduce SHG FROG measurements down to 1 fs resolution. Last but not least, since SPM is a third order effect, when pulses do not have zero chirp they produce unique spectral signatures depending on the sign of their chirp (which isn't the case with second order effects) as will be briefly explored in the next section.

8.3 Second order phase effects

As mentioned in the previous section, SPM produces a unique spectrum depending on the second order phase, or lack thereof. A compressor sweep carried out at UCI to determine the location of most significant SPM broadening (shortest FTL) of 1.3 TW/cm^2 laser pulses in 1.2 mm of fused silica is shown below in Fig. 8.4 (e). Figure 8.4 (a) shows the unbroadened laser spectrum, which was obtained by stretching the pulse out in time by increasing the amount of positive chirp until the point at which no spectral broadening was observed. The remaining spectra in Fig. 8.4, show the unique spectral SPM signatures of having slight positive chirp (b), near zero chirp (c), and slight negative chirp (d). When chirp is positive, there is some spectral broadening, but since the pulse intensity is not maximized it is not as strong as when the chirp is near zero. When the chirp is negative, SPM actually produces spectral narrowing [88] as seen below through not only the visual decrease in fwhm, but also in the increase of FTL in the compressor sweep in the region

> 5295. Recall from Chap. 3 that at UCI, when the compressor has actuator positions $>$ 5295 the pulse has negative chirp, and at actuator positions < 5295 the pulse has positive chirp.

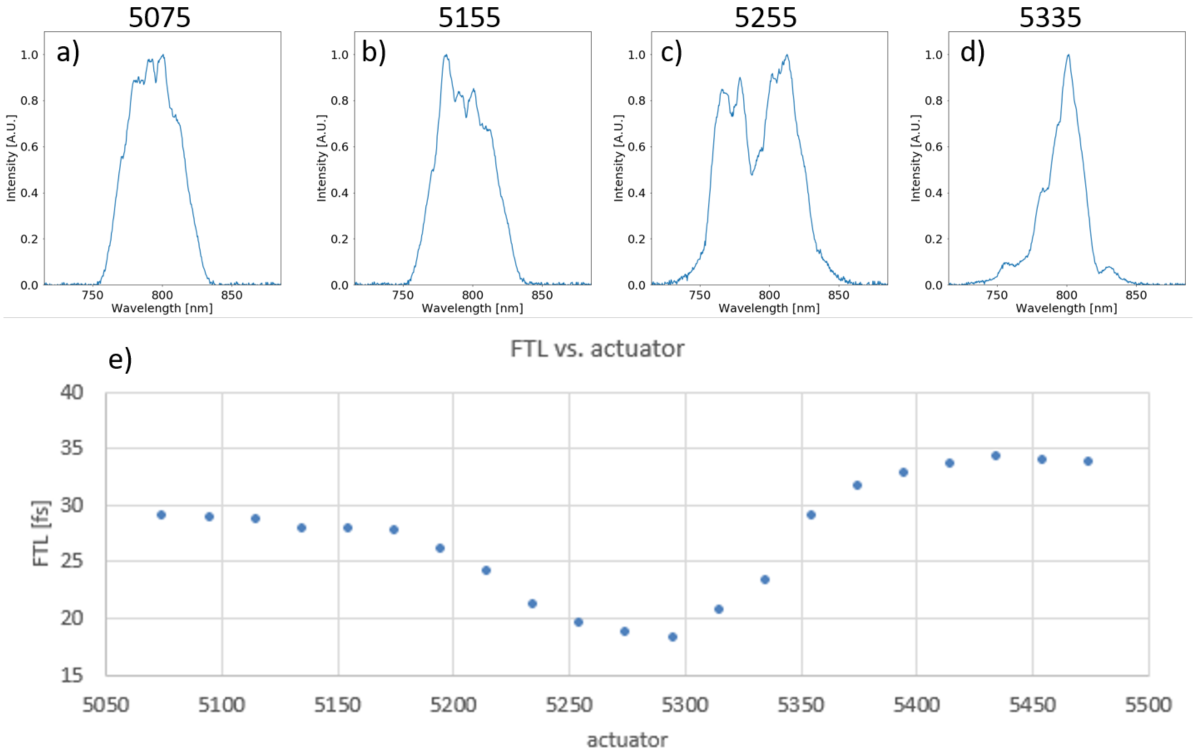

Figure 8.4: SPM spectra (a - d) generated at UCI by ~ 1.3 TW/cm^2 pulses in 1.2 mm of fused silica with varying amounts of quadratic chirp. A spectrum sufficiently chirped (low enough intensity) such that it has no spectral modulations is shown (a) to compare to SPM with slightly positive chirp (b), near zero quadratic chirp (c), and negative chirp (d). A compressor scan is shown in (e) to show that the broadest bimodal spectra are generated near zero quadratic phase, and that the FTL actually decreases on the negative chirp through spectral narrowing

A similar compressor sweep was carried out during one of the experimental campaigns at the HERCULES laser. Laser pulses of $\sim 0.6 - 0.8$ TW/cm^2 were spectrally broadened in 0.5 mm of fused silica, where again the compressor sweep was utilized to determine the location of the most significant SPM broadening. Again here, Figure 8.5 (d) shows the unbroadened laser spectrum, which was obtained by stretching the pulse out in time by increasing the amount of negative chirp until the point at which no spectral modulation was observed. The remaining spectra in Fig. 8.4, show the unique spectral SPM signatures of having slight positive chirp (a), near zero chirp (b), and slight negative chirp (c). When chirp is positive, again there is some spectral broadening, but since the pulse intensity is not maximized it is not as strong as when the chirp is near zero. Again here negatively chirped pulses are shown to visually decrease in fwhm, and also slightly increase of FTL in the compressor sweep in the region $>$ -3.1 mm. In this particular case, I do not have a phase calibration for the compressor sweep to verify the positively chirped and negatively chirped sides, but we know from the SPM spectra which is which.

The upshot of this is that not only can we determine the pulse duration of the shortest un-chirped pulse by the method described in this chapter, but we can also determine whether it is positively or negatively chirped by simply looking at the SPM spectrum. The sign of the chirp is another thing we cannot get from second order effects like SHG FROG, but we get for free by using SPM in fused silica wafers. During the development of this technique by the author, a much more mature technique using multiple wafers and phase retrieval algorithms was discovered in the literature [166]. The simplicity and implicitly limited scope distinguishes the method described in this chapter from the cited method. Since the output spectra from SPM is unique depending on not only the amount of chirp, but also the sign of the chirp it also may be possible to utilize machine learning algorithms (trained by SHG FROG) to uniquely determine the pulse duration and phase, when only provided a spectrum.

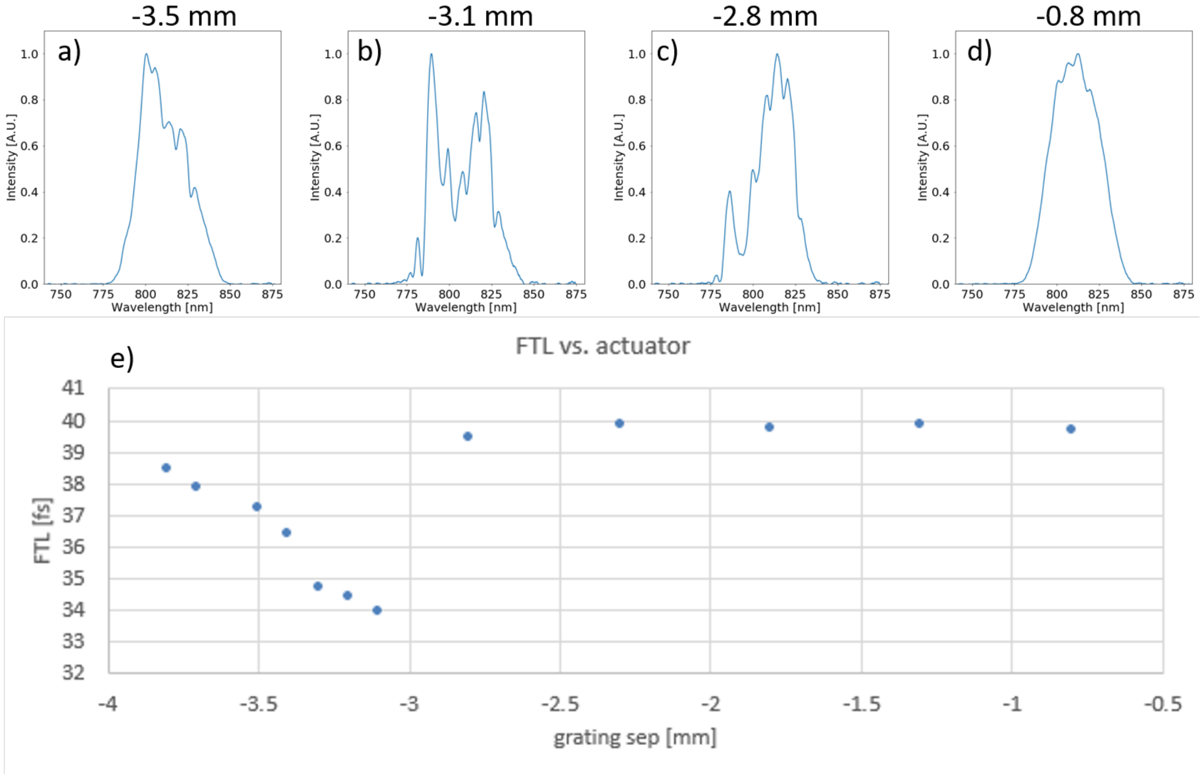

Figure 8.5: SPM spectra (a - d) generated at HERCULES by $\sim 0.6 - 0.8$ TW/cm^2 pulses in 0.5 mm of fused silica with varying amounts of quadratic chirp. A spectrum sufficiently chirped (low enough intensity) such that it has no spectral modulations is shown (d) to compare to SPM with slightly positive chirp (a), near zero quadratic chirp (b), and negative chirp (d). A compressor scan is shown again in (e) to show that the broadest bimodal spectra are generated near zero quadratic phase, and that the FTL actually decreases on the negative chirp through spectral narrowing

Chapter 9

Future applications and outlook

The most significant pulse compression results from the experiments carried out in this thesis work came from using high intensity (~ 2 TW/cm^2) laser pulses and a several thin (4x 0.1 mm) plastic films of Zeonor as the SPM target. Laser pulses were compressed to less than half of their original duration to ~ 23 fs using chirped mirrors to compensate their phase. This promising result suggests that plastics appear be a very tantalizing alternative to fused silica due to their strong nonlinear response as suggested by [48]. Future experiments looking to utilize thin film compression in experiments using Zeonor or other plastics will require the use of optical quality plastic films when they become available. Alternatively, other materials with higher n_2 could also be used, but plastics are routinely made into sub-millimeter films and are inexpensive and therefore expendable- making them an ideal candidate for these exploratory studies. On the other hand, optical quality fused silica wafers can be used as a robust reusable source for of nonlinearity, but may require higher intensities or several stages of compression to reap the benefits of TFC due to the smaller n_2.

9.1 Multi-stage thin film compression

A second stage of thin film compression could be used to take laser pulses to even shorter durations toward the single-cycle limit. Since $\Delta\omega \propto dI/dt$, shorter pulses will require less material to produce the same spectral broadening. For thin film compression to work most effectively, one should begin with as little noise in the near field intensity pattern as possible and a flat-top beam. As discussed at several points throughout the experimental portion of this thesis, laser pulses from high power facilities are rarely "flat-top" and due to small scale spatial intensity fluctuations are susceptible to filamentation [82]. This filamentation can lead to mode-collapse [81] resulting in hot-spots that can damage optics and a ultimately produce a less usable mode. In any real system, there will be some amount of spatial noise in the initial beam that will self-focus and produce filamentation. To address these challenges Mourou *et al.* suggested the use of a spatial filter and deformable mirror after spectral broadening in a thin film [48]. This procedure removes high frequency noise and corrects the wave-front of the compressed pulse to prepare the pulse for a second stage of compression. Single stage pulse compression by $\sim$ a factor of two was demonstrated several systems in this thesis, slightly higher results are likely possible.

Important limiting factors are the multi-photon ionization threshold of the nonlinear media, and the intensity distribution of the near field of the initial laser pulse. The damage threshold of the chirped mirrors themselves also must be high enough to support the compressed intensities. For example, the initial proposal suggested the compression of 5 TW/cm^2 27 fs laser pulses to the single cycle limit. If losses are low, this would bring the intensities close to the multi-photon ionization limit for fused silica ($\sim$ 30 TW/cm^2) [167].

9.2 Self-compression

Additionally for optical wavelengths, materials like fused silica normally have positive GVD which means that the pulse stretches out in time, and makes it very difficult to maintain pulse length with ultra-short pulses. However, in the NIR there exists a wavelength around ~ 1270 nm at which the GVD for fused silica goes to zero. Taking this a step further by going beyond the zero dispersion point we can tune to wavelengths that have negative GVD in fused silica. This means we may be able to investigate wavelengths that self-compress in fused silica without the need for compressive optics like chirped mirrors. This effect has been studied in fibers and when the positive chirp from SPM and the negative chirp from GVD perfectly counteract each other it can lead to soliton formation [65]. Therefore in the case that the GVD compensates for the linear chirp added through SPM it is referred to as soliton compression, as dispersion will compress the newly added linearly chirped bandwidth [95].

9.3 Short-cut to the QED regime

The compression schemes mentioned above have the potential to extend pulse compression further towards the single-cycle regime. As explored in Chap. 1, optical laser pulses in the single-cycle regime have been shown in simulations to produce 10% efficient Doppler up-shifted laser pulses through a coherent relativistic reflection from an overdense plasma [3]. Further scaling of this physical mechanism suggests that laser pulses from Joule class lasers could generate pulses down to 1-10 attoseconds. This relativistic compression to higher frequency could serve as a powerful shortcut to the QED regime as seen in Fig. 9.1.

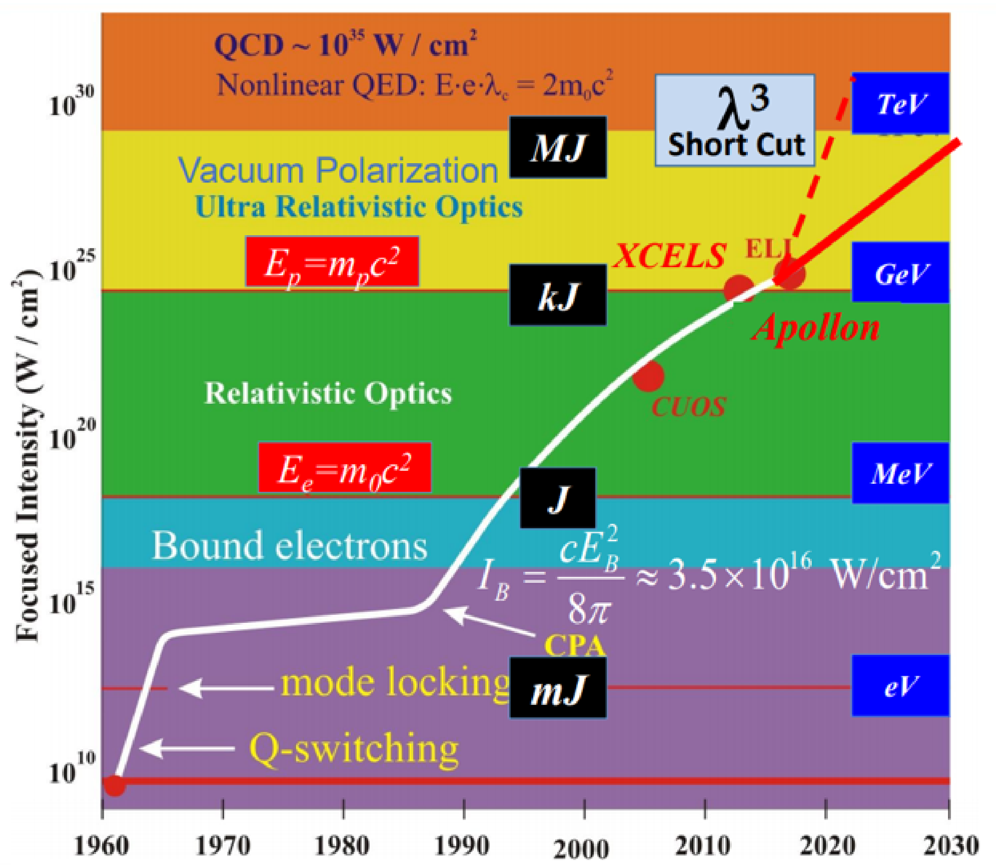

Figure 9.1: Shown above is focused peak intensity versus time. The so-called λ^3 short-cut could grant access to the QED regime, and can be accessed by high energy laser pulses compressed to the single-cycle regime through the relativistic mirror mechanism. Image credit: [1]

These intense, short pulses are anticipated to have many applications in nuclear physics and medicine [2]. Furthermore, these pulses are well-suited to driving wakefields in media with much higher critical density (ie. solids) enabling higher acceleration gradients and extremely compact accelerators with acceleration gradients of TeV/cm^2 [139]. Previously, the path to exawatt power seemingly required ever increasing energy such as MJ lasers. Compression to the optical single-cycle regime and subsequent relativistic compression presents a tantalizing secondary path to this new frontier of high-field science.

Bibliography

[1] G. Mourou and T. Tajima. Exploring fundamental physics at the highest-intensity-laser frontier | SPIE Homepage: SPIE.

[2] T. Tajima, K. Nakajima, and G. Mourou. Laser acceleration. *Nuovo Cimento Rivista Serie*, 40:33–133, February 2017.

[3] N.M. Naumova, J.A. Nees, I.V. Sokolov, B. Hou, and G.A. Mourou. Relativistic generation of isolated attosecond pulses in a lambda 3 focal volume. *Physical review letters*, 92(6):063902, 2004.

[4] T. Tajima. High-energy Lasers: Extreme light in zeptoseconds, 2016.

[5] R. J. Lazarowich, P. Taborek, B.-Y. Yoo, and N. V. Myung. Fabrication of porous alumina on quartz crystal microbalances. *Journal of Applied Physics*, 101(10):104909, May 2007.

[6] F. Albert, R. Shah, K. Phuoc, R. Fitour, F. Burgy, J. Rousseau, A. Tafzi, D. Douillet, T. Lefrou, and A. Rousse. Betatron oscillations of electrons accelerated in laser wakefields characterized by spectral x-ray analysis. *Physical Review E*, 77(5):056402, May 2008.

[7] S. Corde, K. Ta Phuoc, G. Lambert, R. Fitour, V. Malka, A. Rousse, A. Beck, and E. Lefebvre. Femtosecond x rays from laser-plasma accelerators. *Reviews of Modern Physics*, 85(1):1–48, January 2013.

[8] T. H. Maiman. Stimulated optical emission in ruby. In *Journal of the Optical Society of America*, volume 50, pages 1134–1134. AMER INST PHYSICS 1305 WALT WHITMAN RD, STE 300, MELVILLE, NY 11747-4501 USA, 1960.

[9] A. L. Schawlow and C. H. Townes. Infrared and Optical Masers. *Physical Review*, 112(6):1940–1949, December 1958.

[10] J. Hecht. *Understanding lasers an entry-level guide.* IEEE Press understanding science & technology series. IEEE Press, Piscataway, NJ, 3rd ed. edition, 2008.

[11] F. J. McClung and R. W. Hellwarth. Giant Optical Pulsations from Ruby. *Journal of Applied Physics*, 33(3):828–829, March 1962.

[12] H. W. Mocker and R. J. Collins. Mode competition and selflocking effects in a qswitched ruby laser. *Applied Physics Letters*, 7(10):270–273, November 1965.

[13] A. J. DeMaria, D. A. Stetser, and H. Heynau. Self mode-locking of lasers with saturable absorbers. *Applied Physics Letters*, 8(7):174–176, 1966.

[14] G. A. Mourou, C. P. Barty, and M. D. Perry. Ultrahigh-intensity laser: physics of the extreme on a tabletop. Technical Report UCRL-ID-128698, Lawrence Livermore National Lab., CA (United States), October 1997.

[15] Y. R. Shen. Self-focusing: Experimental. *Progress in Quantum Electronics*, 4:1–34, April 1975.

[16] E. S. Bliss, D. R. Speck, J. F. Holzrichter, J. H. Erkkila, and A. J. Glass. Propagation of a highintensity laser pulse with smallscale intensity modulation. *Applied Physics Letters*, 25(8):448–450, October 1974.

[17] G. Mourou. The ultrahigh-peak-power laser: present and future. *Applied Physics B*, 65(2):205–211, August 1997.

[18] D. Strickland and G. Mourou. Compression of amplified chirped optical pulses. *Optics communications*, 56(3):219–221, 1985.

[19] M. D. Perry, D. Pennington, B. C. Stuart, G. Tietbohl, J. A. Britten, C. Brown, S. Herman, B. Golick, M. Kartz, J. Miller, H. T. Powell, M. Vergino, and V. Yanovsky. Petawatt laser pulses. *Optics Letters*, 24(3):160–162, February 1999.

[20] R.A. Snavely, M.H. Key, S.P. Hatchett, T.E. Cowan, M Roth, T.W. Phillips, M.A. Stoyer, E.A. Henry, T.C. Sangster, M.S. Singh, and others. Intense high-energy proton beams from petawatt-laser irradiation of solids. *Physical Review Letters*, 85(14):2945, 2000.

[21] T. Tajima and J.M. Dawson. Laser electron accelerator. *Physical Review Letters*, 43(4):267, 1979.

[22] M.L. Zhou, X.Q. Yan, G. Mourou, J.A. Wheeler, J.H. Bin, J. Schreiber, and T. Tajima. Proton acceleration by single-cycle laser pulses offers a novel monoenergetic and stable operating regime. *Physics of Plasmas (1994-present)*, 23(4):043112, 2016.

[23] T. Tajima. Laser acceleration in novel media. *The European Physical Journal Special Topics*, 223(6):1037–1044, May 2014.

[24] G. Mourou, S. Mironov, E. Khazanov, and A. Sergeev. Single cycle thin film compressor opening the door to Zeptosecond-Exawatt physics. *The European Physical Journal Special Topics*, 223(6):1181–1188, 2014.

[25] eli laser. ELI Delivery Consortium|Home, 2018.

[26] E. Cartlidge. Physicists are planning to build lasers so powerful they could rip apart empty space. 2018.

[27] G. Mourou and T. Tajima. More intense, shorter pulses. *Science*, 331(6013):41–42, 2011.

[28] C. Toth, D. Evans, A. J. Gonsalves, M. Kirkpatrick, A. Magana, G. Mannino, H.-S. Mao, K. Nakamura, J. R. Riley, S. Steinke, T. Sipla, D. Syversrud, N. Ybarrolaza, and W. P. Leemans. Transition of the BELLA PW laser system towards a collaborative research facility in laser plasma science. *AIP Conference Proceedings*, 1812(1):110005, March 2017.

[29] V. Yanovsky, V. Chvykov, G. Kalinchenko, P. Rousseau, T. Planchon, T. Matsuoka, A. Maksimchuk, J. Nees, G. Cheriaux, G. Mourou, and K. Krushelnick. Ultra-high intensity- 300-TW laser at 0.1 Hz repetition rate. *Optics Express*, 16(3):2109–2114, February 2008.

[30] cetal.inflpr.ro. CETAL-PW. 2018.

[31] F. Shimizu. Frequency Broadening in Liquids by a Short Light Pulse. *Physical Review Letters*, 19(19):1097–1100, November 1967.

[32] T. K. Gustafson, J. P. Taran, H. A. Haus, J. R. Lifsitz, and P. L. Kelley. Self-Modulation, Self-Steepening, and Spectral Development of Light in Small-Scale Trapped Filaments. *Physical Review*, 177(1):306–313, January 1969.

[33] R. A. Fisher, P. L. Kelley, and T. K. Gustafson. Subpicosecond pulse generation using the optical kerr effect. *Applied Physics Letters*, 14(4):140–143, February 1969.

[34] A. Laubereau. External frequency modulation and compression of picosecond pulses. *Physics Letters A*, 29(9):539–540, July 1969.

[35] G. Steinmeyer, D. H. Sutter, L. Gallmann, N. Matuschek, and U. Keller. Frontiers in Ultrashort Pulse Generation: Pushing the Limits in Linear and Nonlinear Optics. *Science*, 286(5444):1507–1512, November 1999.

[36] P. L. Kelley. Self-Focusing of Optical Beams. *Physical Review Letters*, 15(26):1005–1008, December 1965.

[37] D. Grischkowsky and A.C. Balant. Optical pulse compression based on enhanced frequency chirping. *Applied Physics Letters*, 41(1):1–3, 1982.

[38] R. H. Stolen and Chinlon Lin. Self-phase-modulation in silica optical fibers. *Physical Review A*, 17(4):1448, 1978.

[39] B. Nikolaus and D. Grischkowsky. 12 pulse compression using optical fibers. *Applied Physics Letters*, 42(1):1–2, January 1983.

[40] C. V. Shank, R. L. Fork, R. Yen, R. H. Stolen, and W. JACK Tomlinson. Compression of femtosecond optical pulses. *Applied Physics Letters*, 40(9):761–763, 1982.

[41] W. H. Knox, R. L. Fork, M. C. Downer, R. H. Stolen, C. V. Shank, and J. A. Valdmanis. Optical pulse compression to 8 fs at a 5-kHz repetition rate. *Applied Physics Letters*, 46(12):1120–1121, 1985.

[42] G. P. Agrawal. *Nonlinear fiber optics.* Academic, Oxford, 5th ed. edition, 2013.

[43] M. Nisoli, S. Stagira, S. De Silvestri, O. Svelto, S. Sartania, Z. Cheng, M. Lenzner, C. Spielmann, and F. Krausz. A novel-high energy pulse compression system: generation of multigigawatt sub-5-fs pulses. *Applied Physics B*, 65(2):189–196, August 1997.

[44] M. Nisoli, S. De Silvestri, and O. Svelto. Generation of high energy 10 fs pulses by a new pulse compression technique. *Applied Physics Letters*, 68(20):2793–2795, 1996.

[45] M. Nisoli, S. De Silvestri, O. Svelto, R. Szipcs, K. Ferencz, Ch. Spielmann, S. Sartania, and F. Krausz. Compression of high-energy laser pulses below 5 fs. *Optics letters*, 22(8):522–524, 1997.

[46] S. Bohman, A. Suda, T. Kanai, S. Yamaguchi, and K. Midorikawa. Generation of 5.0 fs, 5.0 mJ pulses at 1 kHz using hollow-fiber pulse compression. *Optics letters*, 35(11):1887–1889, 2010.

[47] C. Rolland and P. B. Corkum. Compression of high-power optical pulses. *JOSA B*, 5(3):641–647, 1988.

[48] G. Mourou and T. Tajima, editors. *Zetta-Exawatt Science and Technology*, volume 223 of *Eur. Phys. J. Spec. Top.* Springer Verlag, Berlin, 2014.

[49] M. L. Zhou, S. Zhao, H. Y. Wang, C. Lin, H. Y. Lu, Y. R. Lu, T. Tajima, X. T. He, C. E. Chen, Y. Q. Gu, and X. Q. Yan. Instability-free ion acceleration by two laser pulses. *The European Physical Journal Special Topics*, 223(6):1031–1035, May 2014.

[50] A. Maksimchuk, S. Gu, K. Flippo, D. Umstadter, and V. Yu Bychenkov. Forward ion acceleration in thin films driven by a high-intensity laser. *Physical Review Letters*, 84(18):4108, 2000.

[51] E.L. Clark, K. Krushelnick, M. Zepf, F.N. Beg, M. Tatarakis, A. Machacek, M.I.K. Santala, I. Watts, P.A. Norreys, and A.E. Dangor. Energetic heavy-ion and proton generation from ultraintense laser-plasma interactions with solids. *Physical Review Letters*, 85(8):1654, 2000.

[52] X. Q. Yan, T. Tajima, M. Hegelich, L. Yin, and D. Habs. Theory of laser ion acceleration from a foil target of nanometer thickness. *Applied Physics B*, 98(4):711–721, March 2010.

[53] X.Q. Yan, C. Lin, Z.-M. Sheng, Z.Y. Guo, B.C. Liu, Y.R. Lu, J.X. Fang, J.E. Chen, and others. Generating high-current monoenergetic proton beams by a circularlypolarized laser pulse in the phase-stableacceleration regime. *Physical review letters*, 100(13):135003, 2008.

[54] T. Tajima, D. Habs, and X. Yan. Laser acceleration of ions for radiation therapy. *Reviews of Accelerator Science and Technology*, 2(01):201–228, 2009.

[55] H. Daido, M. Nishiuchi, and A.S. Pirozhkov. Review of laser-driven ion sources and their applications. *Reports on Progress in Physics*, 75:056401, 2012.

[56] A. Macchi, M. Borghesi, and M. Passoni. Ion acceleration by superintense laser-plasma interaction. *Reviews of Modern Physics*, 85(2):751, 2013.

[57] A. Macchi. A Review of Laser-Plasma Ion Acceleration. December 2017.

[58] M. Hentschel, R. Kienberger, Ch Spielmann, G. A. Reider, N. Milosevic, T. Brabec, P. Corkum, U. Heinzmann, M. Drescher, and F. Krausz. Attosecond metrology. *Nature*, 414(6863):509–513, November 2001.

[59] R. Kienberger, M. Hentschel, M. Uiberacker, Ch Spielmann, M. Kitzler, A. Scrinzi, M. Wieland, Th Westerwalbesloh, U. Kleineberg, U. Heinzmann, M. Drescher, and F. Krausz. Steering Attosecond Electron Wave Packets with Light. *Science*, 297(5584):1144–1148, August 2002.

[60] E. Goulielmakis, M. Schultze, M. Hofstetter, V. S. Yakovlev, J. Gagnon, M. Uiberacker, A. L. Aquila, E. M. Gullikson, D. T. Attwood, R. Kienberger, F. Krausz, and U. Kleineberg. Single-Cycle Nonlinear Optics. *Science*, 320(5883):1614–1617, June 2008.

[61] J. D. Jackson. *Classical electrodynamics*. Wiley, Lieu de publication inconnu, 2012. OCLC: 967941463.

[62] Frits Zernike & John E. Midwinter. *Applied Nonlinear Optics*. John Wiley and Sons Inc.

[63] R. P. Feynman, R. B. Leighton, and M. L. Sands. *The Feynman lectures on physics*. Addison-Wesley Pub. Co., Reading, Mass., 1963. OCLC: 531535.

[64] RefractiveIndex.INFO - Refractive index database.

[65] A. Weiner. *Ultrafast Optics*. John Wiley & Sons, September 2011. Google-Books-ID: fhohaV7wJbYC.

[66] R. Trebino. *Frequency-Resolved Optical Gating: The Measurement of Ultrashort Laser Pulses*. Springer Science & Business Media, December 2012. Google-Books-ID: 257aBwAAQBAJ.

[67] R. W. Boyd. *Nonlinear Optics*. Elsevier, January 2003. Google-Books-ID: 3vHb7WGXmSQC.

[68] D. L. Mills. *Nonlinear optics: basic concepts*. Springer Science & Business Media, 2012.

[69] G. S. He. *Nonlinear optics and photonics*. OUP Oxford, 2014.

[70] N. Bloembergen. *Nonlinear Optics*. Addison-Wesley Publishing Company, January 1991. Google-Books-ID: zqcYAQAAMAAJ.

[71] A. Owyoung. *The origins of the nonlinear refractive indices of liquids and glasses*. phd, California Institute of Technology, 1972.

[72] G. Duffing. *Erzwungene Schwingungen bei vernderlicher Eigenfrequenz und ihre technische Bedeutung*. Number 41-42. F. Vieweg & sohn, 1918.

[73] P. D. Maker and R. W. Terhune. Study of Optical Effects Due to an Induced Polarization Third Order in the Electric Field Strength. *Physical Review*, 148(2):990–990, August 1966.

[74] N. Boling, A. Glass, and A. Owyoung. Empirical relationships for predicting nonlinear refractive index changes in optical solids. *IEEE Journal of Quantum Electronics*, 14(8):601–608, August 1978.

[75] C. Li. *Nonlinear Optics: Principles and Applications*. Springer Singapore, 2017.

[76] G. Fibich, S. Eisenmann, B. Ilan, Y. Erlich, M. Fraenkel, Z. Henis, A. L. Gaeta, and A. Zigler. Self-focusing distance of very high power laser pulses. *Optics Express*, 13(15):5897–5903, July 2005.

[77] G. Fibich and A. L. Gaeta. Critical power for self-focusing in bulk media and in hollow waveguides. *Optics Letters*, 25(5):335–337, March 2000.

[78] S.V. Chekalin and V Kandidov. From self-focusing light beams to femtosecond laser pulse filamentation. *Physics-Uspekhi*, 56:123, February 2013.

[79] W. Koechner. Laser Amplifier. In *Solid-State Laser Engineering*, Springer Series in Optical Sciences, pages 156–209. Springer, New York, NY, 2006.

[80] K. D. Moll, Alexander L. Gaeta, and Gadi Fibich. Self-Similar Optical Wave Collapse: Observation of the Townes Profile. *Physical Review Letters*, 90(20):203902, May 2003.

[81] T. D. Grow, A. A. Ishaaya, L. T. Vuong, A. L. Gaeta, N. Gavish, and G. Fibich. Collapse dynamics of super-Gaussian beams. *Optics Express*, 14(12):5468–5475, June 2006.

[82] V. I. Bespalov and V. I. Talanov. Filamentary Structure of Light Beams in Nonlinear Liquids. *ZhETF Pisma Redaktsiiu*, 3:471, June 1966.

[83] G. A. Mourou, T. Tajima, and S. V. Bulanov. Optics in the relativistic regime. *Reviews of Modern Physics*, 78(2):309–371, April 2006.

[84] D. J. Kane and R. Trebino. Characterization of arbitrary femtosecond pulses using frequency-resolved optical gating. *IEEE Journal of Quantum Electronics*, 29(2):571–579, February 1993.

[85] S. Y. Mironov, V. V. Lozhkarev, E. Khazanov, and G. Mourou. Compression of femtosecond pulses with a Gaussian temporal and spatial intensity distribution. *Quantum Electronics*, 43(8):711, 2013.

[86] S. Mironov, P. Lassonde, J.-C. Kieffer, E. Khazanov, and G. Mourou. Spatially-uniform temporal recompression of intense femtosecond optical pulses. *The European Physical Journal Special Topics*, 223(6):1175–1180, 2014.

[87] P. Lassonde, S. Mironov, S. Fourmaux, S. Payeur, E. Khazanov, A. Sergeev, J.-C. Kieffer, and G. Mourou. High energy femtosecond pulse compression. *Laser Physics Letters*, 13(7):075401, 2016.

[88] M. Oberthaler and R. A. Hopfel. Special narrowing of ultrashort laser pulses by self phase modulation in optical fibers. *Applied Physics Letters*, 63(8):1017–1019, August 1993.

[89] W. H. Lowdermilk and J. E. Murray. The multipass amplifier: Theory and numerical analysis. *Journal of Applied Physics*, 51(5):2436–2444, May 1980.

[90] R. W. Boyd. Chapter 7 - Processes Resulting from the Intensity-Dependent Refractive Index. In *Nonlinear Optics (Third Edition)*, pages 329–390. Academic Press, Burlington, 2008.

[91] A. J. Taylor, Tracy Sharp Clement, and G. Rodriguez. Determination of n 2 by direct measurement of the optical phase. *Optics letters*, 21(22):1812–1814, 1996.

[92] A. M. Rubenchik, S. K. Turitsyn, and M. P. Fedoruk. Modulation instability in high power laser amplifiers. *Optics Express*, 18(2):1380–1388, January 2010.

[93] Y.-C. Cheng, C.-H. Lu, Y.-Y. Lin, and A. H. Kung. Supercontinuum generation in a multi-plate medium. *Optics Express*, 24(7):7224–7231, April 2016.

[94] J. T. Hunt, J. A. Glaze, W. W. Simmons, and P. A. Renard. Suppression of self-focusing through low-pass spatial filtering and relay imaging. *Applied Optics*, 17(13):2053–2057, July 1978.

[95] W. J. Tomlinson, R. H. Stolen, and C. V. Shank. Compression of optical pulses chirped by self-phase modulation in fibers. *JOSA B*, 1(2):139–149, April 1984.

[96] C. Gardner and R. McWilliams. Personal Communication. 2017.

[97] W.P. Leemans, A.J. Gonsalves, H.-S. Mao, K. Nakamura, C. Benedetti, C.B. Schroeder, Cs. Tth, J. Daniels, D.E. Mittelberger, S.S. Bulanov, and others. Multi-GeV electron beams from capillary-discharge-guided subpetawatt laser pulses in the self-trapping regime. *Physical review letters*, 113(24):245002, 2014.

[98] J.S. Liu, C.Q. Xia, W.T. Wang, H.Y. Lu, Ch. Wang, A.H. Deng, W.T. Li, H. Zhang, X.Y. Liang, Y.X. Leng, and others. All-optical cascaded laser wakefield accelerator using ionization-induced injection. *Physical review letters*, 107(3):035001, 2011.

[99] W.P. Leemans, B. Nagler, A.J. Gonsalves, Cs. Toth, K. Nakamura, C.G.R. Geddes, E. Esarey, C.B. Schroeder, and S.M. Hooker. GeV electron beams from a centimetre-scale accelerator. *Nature physics*, 2(10):696–699, 2006.

[100] K. Nakajima, D. Fisher, T. Kawakubo, H. Nakanishi, A. Ogata, Y. Kato, Y. Kitagawa, R. Kodama, K. Mima, H. Shiraga, and others. Observation of ultrahigh gradient electron acceleration by a self-modulated intense short laser pulse. *Physical Review Letters*, 74(22):4428, 1995.

[101] M. Litos, E. Adli, W. An, C. I. Clarke, C. E. Clayton, S. Corde, J. P. Delahaye, R. J. England, A. S. Fisher, J. Frederico, S. Gessner, S. Z. Green, M. J. Hogan, C. Joshi, W. Lu, K. A. Marsh, W. B. Mori, P. Muggli, N. Vafaei-Najafabadi, D. Walz, G. White, Z. Wu, V. Yakimenko, and G. Yocky. High-efficiency acceleration of an electron beam in a plasma wakefield accelerator. *Nature*, 515(7525):92–95, November 2014.

[102] W. Lu, M. Tzoufras, C. Joshi, F. S. Tsung, W. B. Mori, J. Vieira, R. A. Fonseca, and L. O. Silva. Generating multi-GeV electron bunches using single stage laser wakefield acceleration in a 3d nonlinear regime. *Physical Review Special Topics - Accelerators and Beams*, 10(6):061301, June 2007.

[103] E. Esarey, C. B. Schroeder, and W. P. Leemans. Physics of laser-driven plasma-based electron accelerators. *Rev. Mod. Phys.*, 81(3):1229–1285, August 2009.

[104] P. Chen and R. J. Noble. Channeled Particle Acceleration by Plasma Waves in Metals. In *Relativistic Channeling*, NATO ASI Series, pages 517–522. Springer, Boston, MA, 1987.

[105] P. Chen and R. J. Noble. A solid state accelerator. *AIP Conference Proceedings*, 156(1):222–227, May 1987.

[106] T. Tajima and M. Cavenago. Crystal x-ray accelerator. *Physical Review Letters*, 59(13):1440–1443, September 1987.

[107] B. S. Newberger and T. Tajima. High-energy beam transport in crystal channels. *Physical Review A*, 40(12):6897–6903, December 1989.

[108] B. Newberger, T. Tajima, F. R. Huson, W. Mackay, B. C. Covington, J. R. Payne, Z. G. Zou, N. K. Mahale, and S. Ohnuma. Application of novel material in crystal accelerator concepts. In *, Proceedings of the 1989 IEEE Particle Accelerator Conference, 1989. Accelerator Science and Technology*, pages 630–632 vol.1, March 1989.

[109] T. Tajima, B.S. Newberger, F.R. Huson, W.W. Mackay, B.C. Covington, J. Payne, N.K. Mahale, and S. Ohnuma. Beam Transport in the crystal x-ray accelerator. *Particle Acclerators*, 32:235, 1990.

[110] B. Newberger and T. Tajima. FokkerPlanck transport in solid state accelerator concepts. *AIP Conference Proceedings*, 193(1):290–294, October 1989.

[111] Z. Huang, P. Chen, and R. D. Ruth. Radiation Reaction in a Continuous Focusing Channel. *Physical Review Letters*, 74(10):1759–1762, March 1995.

[112] P. Chen and R. J. Noble. Crystal channel collider: Ultra-high energy and luminosity in the next century. *AIP Conference Proceedings*, 398(1):273–285, March 1997.

[113] D. S. Gemmell. Channeling and related effects in the motion of charged particles through crystals. *Reviews of Modern Physics*, 46(1):129–227, January 1974.

[114] Y.-M. Shin, D. A. Still, and V. Shiltsev. X-ray driven channeling acceleration in crystals and carbon nanotubes. *Physics of Plasmas*, 20(12):123106, December 2013.

[115] Young-Min Shin. Beam-driven acceleration in ultra-dense plasma media. *Applied Physics Letters*, 105(11):114106, September 2014.

[116] P.A. Walker, N. Bourgeois, W. Rittershofer, J. Cowley, N. Kajumba, A.R. Maier, J. Wenz, C.M. Werle, S. Karsch, F. Gruner, and D.R. Symes. Investigation of GeV-scale electron acceleration in a gas-filled capillary discharge waveguide. *New Journal of Physics*, 15(4):045024, 2013.

[117] F. S. Tsung, Ritesh Narang, W. B. Mori, C. Joshi, R. A. Fonseca, and L. O. Silva. Near-GeV-Energy Laser-Wakefield Acceleration of Self-Injected Electrons in a Centimeter-Scale Plasma Channel. *Physical Review Letters*, 93(18):185002, October 2004.

[118] S. Iijima. Helical microtubules of graphitic carbon. *Nature*, 354(6348):56–58, November 1991.

[119] N. V. Myung, J. Lim, J.-P. Fleurial, M. Yun, W. West, and D. Choi. Alumina nanotemplate fabrication on silicon substrate. *Nanotechnology*, 15(7):833, 2004.

[120] H. Hou, A. K. Schaper, F. Weller, and A. Greiner. Carbon Nanotubes and Spheres Produced by Modified Ferrocene Pyrolysis. *Chemistry of Materials*, 14(9):3990–3994, September 2002.

[121] T. Tajima and S. Ushioda. Surface polaritons in LO-phonon-plasmon coupled systems in semiconductors. *Physical Review B*, 18(4):1892–1897, August 1978.

[122] T. D. Arber, K. Bennett, C. S. Brady, A. Lawrence-Douglas, M. G. Ramsay, N. J. Sircombe, P. Gillies, R. G. Evans, H Schmitz, A. R. Bell, and C. P. Ridgers. Contemporary particle-in-cell approach to laser-plasma modelling. *Plasma Physics and Controlled Fusion*, 57(11):113001, 2015.

[123] M.C. Thompson. 2004.

[124] A. Pukhov, O. Jansen, T. Tueckmantel, J. Thomas, and I.Yu. Kostyukov. Field-Reversed Bubble in Deep Plasma Channels for High-Quality Electron Acceleration. *Physical Review Letters*, 113(24):245003, December 2014.

[125] F. Albert, B. B. Pollock, J. L. Shaw, K. A. Marsh, J. E. Ralph, Y.-H. Chen, D. Alessi, A. Pak, C. E. Clayton, S. H. Glenzer, and C. Joshi. Angular Dependence of Betatron X-Ray Spectra from a Laser-Wakefield Accelerator. *Physical Review Letters*, 111(23):235004, December 2013.

[126] S. Cipiccia, M. R. Islam, B. Ersfeld, R. P. Shanks, E. Brunetti, G. Vieux, X. Yang, R. C. Issac, S. M. Wiggins, G. H. Welsh, M.-P. Anania, D. Maneuski, R. Montgomery, G. Smith, M. Hoek, D. J. Hamilton, N. R. C. Lemos, D. Symes, P. P. Rajeev, V. O. Shea, J. M. Dias, and D. A. Jaroszynski. Gamma-rays from harmonically resonant betatron oscillations in a plasma wake. *Nature Physics*, 7(11):867–871, November 2011.

[127] E. Esarey, B. A. Shadwick, P. Catravas, and W. P. Leemans. Synchrotron radiation from electron beams in plasma-focusing channels. *Physical Review E*, 65(5):056505, May 2002.

[128] J. Schwinger. The Quantum Correction in the Radiation by Energetic Accelerated Electrons. *Proceedings of the National Academy of Sciences*, 40(2):132–136, February 1954.

[129] A. R. Bell and John G. Kirk. Possibility of Prolific Pair Production with High-Power Lasers. *Physical Review Letters*, 101(20):200403, November 2008.

[130] R. Keinigs, W. Peter, and M. E. Jones. A comparison of the dielectric and plasma wakefield accelerators. *Physics of Fluids B: Plasma Physics*, 1(9):1872–1879, September 1989.

[131] M. C. Thompson, H. Badakov, J. B. Rosenzweig, G. Travish, M. J. Hogan, R. Ischebeck, N. Kirby, R. Siemann, D. Walz, P. Muggli, A. Scott, and R. Yoder.

Observation of multi-GeV breakdown thresholds in dielectric wakefield structures. In *2007 IEEE Particle Accelerator Conference (PAC)*, pages 3026–3028, June 2007.

[132] G. Andonian, D. Stratakis, M. Babzien, S. Barber, M. Fedurin, E. Hemsing, K. Kusche, P. Muggli, B. OShea, X. Wei, O. Williams, V. Yakimenko, and J. B. Rosenzweig. Dielectric Wakefield Acceleration of a Relativistic Electron Beam in a Slab-Symmetric Dielectric Lined Waveguide. *Physical Review Letters*, 108(24):244801, June 2012.

[133] N. Saito and A. Ogata. Plasmon linac: A laser wake-field accelerator based on a solid-state plasma. *Physics of Plasmas*, 10(8):3358–3362, July 2003.

[134] I. Y. Dodin and N. J. Fisch. Charged particle acceleration in dense plasma channels. *Physics of Plasmas*, 15(10):103105, October 2008.

[135] P. Chen, J.M. Dawson, R. W. Huff, and T. Katsouleas. Acceleration of electrons by the interaction of a bunched electron beam with a plasma. *Physical review letters*, 54(7):693, 1985.

[136] A. Caldwell, K. Lotov, A. Pukhov, and F. Simon. Proton-driven plasma-wakefield acceleration. *Nature Physics*, 5(5):363–367, 2009.

[137] T. Tajima. High energy laser plasma accelerators. *Laser and Particle Beams*, 3(4):351–413, 1985.

[138] Toshiki Tajima. Laser acceleration and its future. *Proceedings of the Japan Academy, Series B*, 86(3):147–157, 2010.

[139] X. Zhang, T. Tajima, D. Farinella, Y.-M. Shin, G. Mourou, J. Wheeler, P. Taborek, P. Chen, F. Dollar, and B. Shen. Particle-in-cell simulation of x-ray wakefield acceleration and betatron radiation in nanotubes. *Physical Review Accelerators and Beams*, 19(10):101004, October 2016.

[140] T. Ebisuzaki and T. Tajima. Pondermotive acceleration of charged particles along the relativistic jets of an accreting blackhole. *The European Physical Journal Special Topics*, 223(6):1113–1120, 2014.

[141] Y. Takahashi, L. W. Hillman, and T. Tajima. Relativistic Lasers and High Energy Astrophysics. In *High-Field Science*, pages 171–221. Springer, Boston, MA, 2000.

[142] P. Chen, T. Tajima, and Y. Takahashi. Plasma Wakefield Acceleration for Ultrahigh-Energy Cosmic Rays. *Physical Review Letters*, 89(16):161101, September 2002.

[143] J. S. T. Ng and P. Chen. Prospects of high energy laboratory astrophysics. *International Journal of Modern Physics B*, 21(03n04):312–318, February 2007.

[144] E. Fermi. On the Origin of the Cosmic Radiation. *Physical Review*, 75(8):1169–1174, April 1949.

[145] E. Fermi. Galactic Magnetic Fields and the Origin of Cosmic Radiation. *The Astrophysical Journal*, 119:1, January 1954.

[146] C.K. Lau, P.-C. Yeh, O. Luk, J. McClenaghan, T. Ebisuzaki, and T. Tajima. Ponderomotive acceleration by relativistic waves. *Physical Review Special Topics-Accelerators and Beams*, 18(2):024401, 2015.

[147] H. Wiedemann. *Particle Accelerator Physics.* Springer-Verlag, Berlin Heidelberg, 3 edition, 2007.

[148] T. Tajima. *Computational plasma physics. With applications to fusion and astrophysics.* 1989.

[149] N. P. Klepikov. Emission of photons or electron-positron paris in magnetic fields. *Zhur. Eksptl.' i Teoret. Fiz.*, Vol: 26, January 1954.

[150] T. Erber. High-Energy Electromagnetic Conversion Processes in Intense Magnetic Fields. *Reviews of Modern Physics*, 38(4):626–659, October 1966.

[151] C. P. Ridgers, J. G. Kirk, R. Duclous, T. G. Blackburn, C. S. Brady, K. Bennett, T. D. Arber, and A. R. Bell. Modelling gamma-ray photon emission and pair production in high-intensity lasermatter interactions. *Journal of Computational Physics*, 260:273–285, March 2014.

[152] I. Kostyukov, S. Kiselev, and A. Pukhov. X-ray generation in an ion channel. *Physics of Plasmas*, 10(12):4818–4828, November 2003.

[153] J. G. Kirk, A. R. Bell, and I. Arka. Pair production in counter-propagating laser beams. *Plasma Physics and Controlled Fusion*, 51(8):085008, 2009.

[154] R. Duclous, J. G. Kirk, and A. R. Bell. Monte Carlo calculations of pair production in high-intensity laserplasma interactions. *Plasma Physics and Controlled Fusion*, 53(1):015009, 2011.

[155] A. Zhidkov, J. Koga, A. Sasaki, and M. Uesaka. Radiation Damping Effects on the Interaction of Ultraintense Laser Pulses with an Overdense Plasma. *Physical Review Letters*, 88(18):185002, April 2002.

[156] S. V. Bulanov, T. Zh. Esirkepov, M. Kando, J. K. Koga, and S. S. Bulanov. Lorentz-Abraham-Dirac versus Landau-Lifshitz radiation friction force in the ultrarelativistic electron interaction with electromagnetic wave (exact solutions). *Physical Review E*, 84(5):056605, November 2011.

[157] T Esirkepov, M Borghesi, SV Bulanov, G Mourou, and T Tajima. Highly efficient relativistic-ion generation in the laser-piston regime. *Physical review letters*, 92(17):175003, 2004.

[158] T. Tajima and K. Shibata. Plasma astrophysics. 1997.

[159] A. Mizuta, T. Ebisuzaki, T. Tajima, and S. Nagataki. Production of intense episodic Alfven pulses: GRMHD simulation of black hole accretion disks. *arXiv:1707.08799 [astro-ph]*, July 2017. arXiv: 1707.08799.

[160] N. E. Canac, K. N. Abazajian, T. Tajima, T. Ebisuzaki, and S. Horiuchi. Observational Signatures of Gamma Rays from Bright Blazars and Wakefield Theory. *arXiv:1709.06535 [astro-ph]*, September 2017. arXiv: 1709.06535.

[161] A. A. Abdo, M. Ackermann, M. Ajello, E. Antolini, L. Baldini, J. Ballet, G. Barbiellini, D. Bastieri, K. Bechtol, R. Bellazzini, B. Berenji, R. D. Blandford, E. D. Bloom, E. Bonamente, A. W. Borgland, A. Bouvier, J. Bregeon, A. Brez, M. Brigida, P. Bruel, R. Buehler, T. H. Burnett, S. Buson, G. A. Caliandro, R. A. Cameron, P. A. Caraveo, S. Carrigan, J. M. Casandjian, E. Cavazzuti, C. Cecchi, elik, A. Chekhtman, C. C. Cheung, J. Chiang, S. Ciprini, R. Claus, J. Cohen-Tanugi, L. R. Cominsky, J. Conrad, L. Costamante, S. Cutini, C. D. Dermer, A. de Angelis, F. de Palma, E. do Couto e Silva, P. S. Drell, R. Dubois, D. Dumora, C. Farnier, C. Favuzzi, S. J. Fegan, W. B. Focke, P. Fortin, M. Frailis, Y. Fukazawa, S. Funk, P. Fusco, F. Gargano, D. Gasparrini, N. Gehrels, S. Germani, B. Giebels, N. Giglietto, P. Giommi, F. Giordano, T. Glanzman, G. Godfrey, I. A. Grenier, M.-H. Grondin, J. E. Grove, S. Guiriec, D. Hadasch, M. Hayashida, E. Hays, S. E. Healey, D. Horan, R. E. Hughes, R. Itoh, G. Jhannesson, A. S. Johnson, W. N. Johnson, T. Kamae, H. Katagiri, J. Kataoka, N. Kawai, J. Kndlseder, M. Kuss, J. Lande, S. Larsson, L. Latronico, M. Lemoine-Goumard, F. Longo, F. Loparco, B. Lott, M. N. Lovellette, P. Lubrano, G. M. Madejski, A. Makeev, E. Massaro, M. N. Mazziotta, J. E. McEnery, P. F. Michelson, W. Mitthumsiri, T. Mizuno, A. A. Moiseev, C. Monte, M. E. Monzani, A. Morselli, I. V. Moskalenko, M. Mueller, S. Murgia, P. L. Nolan, J. P. Norris, E. Nuss, M. Ohno, T. Ohsugi, N. Omodei, E. Orlando, J. F. Ormes, M. Ozaki, J. H. Panetta, D. Parent, V. Pelassa, M. Pepe, M. Pesce-Rollins, F. Piron, T. A. Porter, S. Rain, R. Rando, M. Razzano, A. Reimer, O. Reimer, S. Ritz, A. Y. Rodriguez, R. W. Romani, M. Roth, F. Ryde, H. F.-W. Sadrozinski, A. Sander, J. D. Scargle, C. Sgr, M. S. Shaw, P. D. Smith, G. Spandre, P. Spinelli, J.-L. Starck, M. S. Strickman, D. J. Suson, H. Takahashi, T. Takahashi, T. Tanaka, J. B. Thayer, J. G. Thayer, D. J. Thompson, L. Tibaldo, D. F. Torres, G. Tosti, A. Tramacere, Y. Uchiyama, T. L. Usher, V. Vasileiou, N. Vilchez, V. Vitale, A. P. Waite, E. Wallace, P. Wang, B. L. Winer, K. S. Wood, Z. Yang, T. Ylinen, and M. Ziegler. Gamma-ray Light Curves and Variability of Bright Fermi-detected Blazars. *The Astrophysical Journal*, 722(1):520, 2010.

[162] A. A. Abdo, M. Ackermann, M. Ajello, W. B. Atwood, M. Axelsson, L. Baldini, J. Ballet, G. Barbiellini, D. Bastieri, K. Bechtol, R. Bellazzini, B. Berenji, R. D. Blandford, E. D. Bloom, E. Bonamente, A. W. Borgland, A. Bouvier, J. Bregeon, A. Brez, M. Brigida, P. Bruel, T. H. Burnett, S. Buson, G. A. Caliandro, R. A. Cameron, P. A. Caraveo, S. Carrigan, J. M. Casandjian, E. Cavazzuti, C. Cecchi,

elik, E. Charles, A. Chekhtman, C. C. Cheung, J. Chiang, S. Ciprini, R. Claus, J. Cohen-Tanugi, J. Conrad, S. Cutini, C. D. Dermer, A. de Angelis, F. de Palma, S. W. Digel, E. do Couto e Silva, P. S. Drell, R. Dubois, D. Dumora, C. Farnier, C. Favuzzi, S. J. Fegan, W. B. Focke, P. Fortin, M. Frailis, Y. Fukazawa, S. Funk, P. Fusco, F. Gargano, D. Gasparrini, N. Gehrels, S. Germani, B. Giebels, N. Giglietto, P. Giommi, F. Giordano, T. Glanzman, G. Godfrey, I. A. Grenier, M.-H. Grondin, J. E. Grove, L. Guillemot, S. Guiriec, A. K. Harding, R. C. Hartman, M. Hayashida, E. Hays, S. E. Healey, D. Horan, R. E. Hughes, M. S. Jackson, G. Jhannesson, A. S. Johnson, W. N. Johnson, T. Kamae, H. Katagiri, J. Kataoka, N. Kawai, M. Kerr, J. Kndlseder, M. Kuss, J. Lande, L. Latronico, M. Lemoine-Goumard, F. Longo, F. Loparco, B. Lott, M. N. Lovellette, P. Lubrano, G. M. Madejski, A. Makeev, M. N. Mazziotta, W. McConville, J. E. McEnery, C. Meurer, P. F. Michelson, W. Mitthumsiri, T. Mizuno, A. A. Moiseev, C. Monte, M. E. Monzani, A. Morselli, I. V. Moskalenko, S. Murgia, P. L. Nolan, J. P. Norris, E. Nuss, T. Ohsugi, N. Omodei, E. Orlando, J. F. Ormes, D. Paneque, J. H. Panetta, D. Parent, V. Pelassa, M. Pepe, M. Persic, M. Pesce-Rollins, F. Piron, T. A. Porter, S. Rain, R. Rando, M. Razzano, A. Reimer, O. Reimer, T. Reposeur, S. Ritz, L. S. Rochester, A. Y. Rodriguez, R. W. Romani, M. Roth, F. Ryde, H. F.-W. Sadrozinski, D. Sanchez, A. Sander, P. M. Saz Parkinson, J. D. Scargle, C. Sgr, E. J. Siskind, D. A. Smith, P. D. Smith, G. Spandre, P. Spinelli, M. S. Strickman, D. J. Suson, H. Tajima, H. Takahashi, T. Takahashi, T. Tanaka, J. B. Thayer, J. G. Thayer, D. J. Thompson, L. Tibaldo, D. F. Torres, G. Tosti, A. Tramacere, Y. Uchiyama, T. L. Usher, V. Vasileiou, N. Vilchez, M. Villata, V. Vitale, A. P. Waite, P. Wang, B. L. Winer, K. S. Wood, T. Ylinen, and M. Ziegler. Spectral Properties of Bright Fermi-Detected Blazars in the Gamma-Ray Band. *The Astrophysical Journal*, 710(2):1271, 2010.

[163] M. Ajello, A. Albert, W. B. Atwood, G. Barbiellini, D. Bastieri, K. Bechtol, R. Bellazzini, E. Bissaldi, R. D. Blandford, E. D. Bloom, R. Bonino, E. Bottacini, T. J. Brandt, J. Bregeon, P. Bruel, R. Buehler, S. Buson, G. A. Caliandro, R. A. Cameron, R. Caputo, M. Caragiulo, P. A. Caraveo, C. Cecchi, A. Chekhtman, J. Chiang, G. Chiaro, S. Ciprini, J. Cohen-Tanugi, L. R. Cominsky, J. Conrad, S. Cutini, F. DAmmando, A. de Angelis, F. de Palma, R. Desiante, L. Di Venere, P. S. Drell, C. Favuzzi, E. C. Ferrara, P. Fusco, F. Gargano, D. Gasparrini, N. Giglietto, P. Giommi, F. Giordano, M. Giroletti, T. Glanzman, G. Godfrey, G. A. Gomez-Vargas, I. A. Grenier, S. Guiriec, M. Gustafsson, A. K. Harding, J. W. Hewitt, A. B. Hill, D. Horan, T. Jogler, G. Jhannesson, A. S. Johnson, T. Kamae, C. Karwin, J. Kndlseder, M. Kuss, S. Larsson, L. Latronico, J. Li, L. Li, F. Longo, F. Loparco, M. N. Lovellette, P. Lubrano, J. Magill, S. Maldera, D. Malyshev, A. Manfreda, M. Mayer, M. N. Mazziotta, P. F. Michelson, W. Mitthumsiri, T. Mizuno, A. A. Moiseev, M. E. Monzani, A. Morselli, I. V. Moskalenko, S. Murgia, E. Nuss, M. Ohno, T. Ohsugi, N. Omodei, E. Orlando, J. F. Ormes, D. Paneque, M. Pesce-Rollins, F. Piron, G. Pivato, T. A. Porter, S. Rain, R. Rando, M. Razzano, A. Reimer, O. Reimer, S. Ritz, M. Snchez-Conde, P. M. Saz Parkinson, C. Sgr, E. J.

Siskind, D. A. Smith, F. Spada, G. Spandre, P. Spinelli, D. J. Suson, H. Tajima, H. Takahashi, J. B. Thayer, D. F. Torres, G. Tosti, E. Troja, Y. Uchiyama, G. Vianello, B. L. Winer, K. S. Wood, G. Zaharijas, and S. Zimmer. Fermi-LAT Observations of High-Energy Gamma-Ray Emission toward the Galactic Center. *The Astrophysical Journal*, 819(1):44, 2016.

[164] T. Ebisuzaki and T. Tajima. Astrophysical ZeV acceleration in the relativistic jet from an accreting supermassive blackhole. *Astroparticle Physics*, 56:9–15, April 2014.

[165] T Tajima and M Binderbauer. *The Physics of Plasma-driven Accelerators and Accelerator-driven Fusion: The Proceedings of Norman Rostoker Memorial Symposium*. AIP Publishing.

[166] E. A. Anashkina, V. N. Ginzburg, A. A. Kochetkov, I. V. Yakovlev, A. V. Kim, and E. A. Khazanov. Single-shot laser pulse reconstruction based on self-phase modulated spectra measurements. *Scientific Reports*, 6:33749, September 2016.

[167] V. V. Temnov, K. Sokolowski-Tinten, P. Zhou, A. El-Khamhawy, and D. Von Der Linde. Multiphoton ionization in dielectrics: comparison of circular and linear polarization. *Physical review letters*, 97(23):237403, 2006.

Appendix A

EPOCH QED synchrotron

The photon emission package in the simulation code EPOCH is based on quantum corrected synchrotron radiation theory developed by Klepikov [149]. It closely resembles theory developed by Schwinger in the same year [128]. This section will very briefly review the classical synchrotron function and discuss its limitations. Finally it will present the quantum corrected functions from Schwinger and Klepikov (the relevant model for EPOCH).

A.1 Classical synchrotron function

When the Lorentz factor of high energy electrons executing sinusoidal motion becomes large enough, the trajectory becomes distorted in the lab frame. The radiation from this motion is called Synchrotron radiation and is characterized by a series of harmonics up to a critical energy ε_{cr} [61].

$$\hbar\omega_{cr} = \varepsilon_{cr} = \frac{3}{2}\frac{\hbar c}{r}\gamma_e^2 \tag{A.1}$$

This photon energy-determined by the bending radius r, and the electron Lorentz factor γ_e fully determines the synchrotron spectrum given by ε_{cr} [61].

$$\frac{dI}{d\left(\frac{\varepsilon}{\varepsilon_{cr}}\right)}\frac{1}{I} = S\left(\frac{\varepsilon}{\varepsilon_{cr}}\right) = \frac{9\sqrt{3}}{8\pi}\left(\frac{\varepsilon}{\varepsilon_{cr}}\right)\int_{\varepsilon/\varepsilon_{cr}}^{\infty} K_{5/3}(x)dx \tag{A.2}$$

Here $I = 4\pi e^2\gamma_e^4/(3r)$ and $K_{5/3}$ is the modified Bessel function. One thing to note about the classical function is that when the electron energy and bending fields become strong enough, the model begins to predict photons with higher energies than their parent electrons [128]. In Table A.1, typical bending fields present in laser wakefields in solids O($\sim 10^{12}$ V/m), along with different electron energies in the range $\sim$ 5 - 500 GeV are shown. It is seen that as the electron energies become large, the classical model becomes nonphysical - violating energy conservation.

η	E [V/m]	γ_e	E_e [GeV]	ε_{crit}[GeV]
0.01	10^{12}	10^4	5.1	0.077
0.1	10^{12}	10^5	51	7.7
1	10^{12}	10^6	510	770

Table A.1: Predicted values for critical photon energy in classical synchrotron theory. Near $\eta \sim 1$, photon energies with more energy that their emitting electrons are predicted, violating energy conservation. A quantum corrected theory was developed by Schwinger and Klepikov in 1954.

A.2 QED corrected synchrotron function

Klepikov introduced parameters χ and η which serve as the parameterized unitless photon and electron energies [149, 153].

$$\eta = \gamma_e \sin\theta \frac{E}{E_S} \tag{A.3}$$

$$\chi = \frac{h\nu}{2m_e c^2}\frac{E}{E_S} \tag{A.4}$$

Here $E_S = m_e^2 c^3/(e\hbar)$ is the Schwinger field. When these quantities become ≥ 0.1, quantum effects begin to play more of a role [122]. Specifically, the η parameter determines the when the photon emission process of high energy electrons in strong bending fields needs to be corrected by the quantum mechanical model. On the other hand, χ determines the degree of which photon processes such as pair production play a role. The quantum corrected synchrotron model used by EPOCH can be seen below

$$F(\eta, \chi) = \frac{4\chi^2}{\eta^2} y K_{2/3}(y) + \left(1 - 2\frac{\eta}{\chi}\right) y \int_y^\infty K_{5/3}(x) dx \tag{A.5}$$

$$y = \frac{4\chi}{3\eta(\eta - 2\chi)} \tag{A.6}$$

The critical thing to note, as seen below in Fig. A.1 is that if $\eta \geq 0.1$ the synchrotron emission spectrum becomes suppressed. Figure A.1 shows the classical synchrotron curve for various η parameters in all cases with a dotted blue line. Figure (a), (b) and (c) show the Schwinger correction to the classical synchrotron function with a solid orange line, whereas (d), (e) and (f) show the Klepikov correction which is used in EPOCH, and begins to deviate from Schwinger at $\eta \sim 1$. Note that in the Schwinger model at $\eta = 1$ ($E_e \approx 5 \times 10^5$ MeV), photons are predicted to have energies up to $\sim 10^6$ MeV, whereas in the Klepikov model under the same conditions, photons are predicted to have energies up to $\sim 3.5 \times 10^5$ MeV preserving energy conservation. Assuming $\eta << 1$, the critical photon energy can be estimated with classical theory (the blue dotted line) by $\varepsilon_{cr}[\text{MeV}] = 0.75\eta\gamma_{\text{e}}$, and the most probable photon value by $\varepsilon_{mp} = 0.22\eta\gamma_e$ [154, 153].

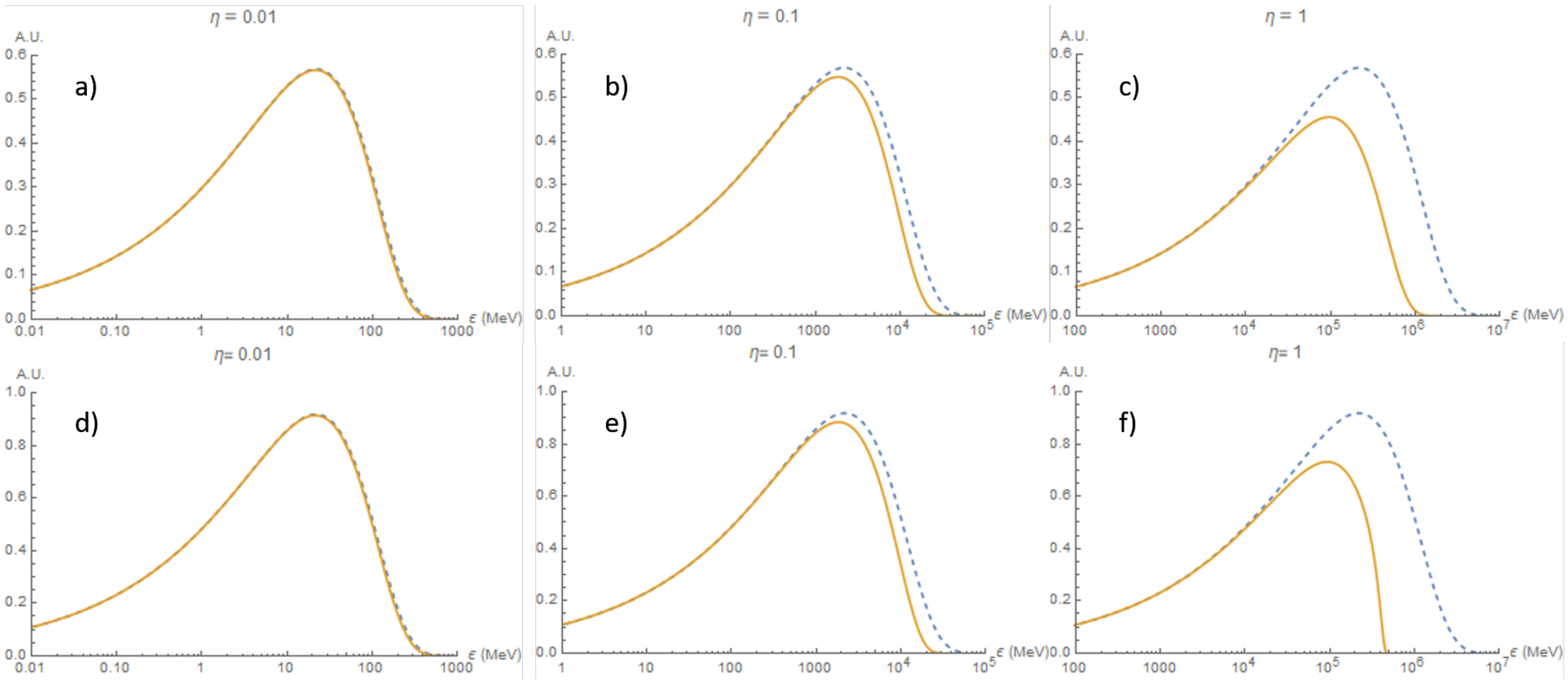

Figure A.1: The classical synchrotron function (blue-dotted) is plotted against Schwinger's quantum corrected synchrotron function (a), (b) and (c) and Klepikov's quantum corrected synchrotron function (d), (e) and (f). The values of η and γ_e and E from Table A.1 are used in each case.